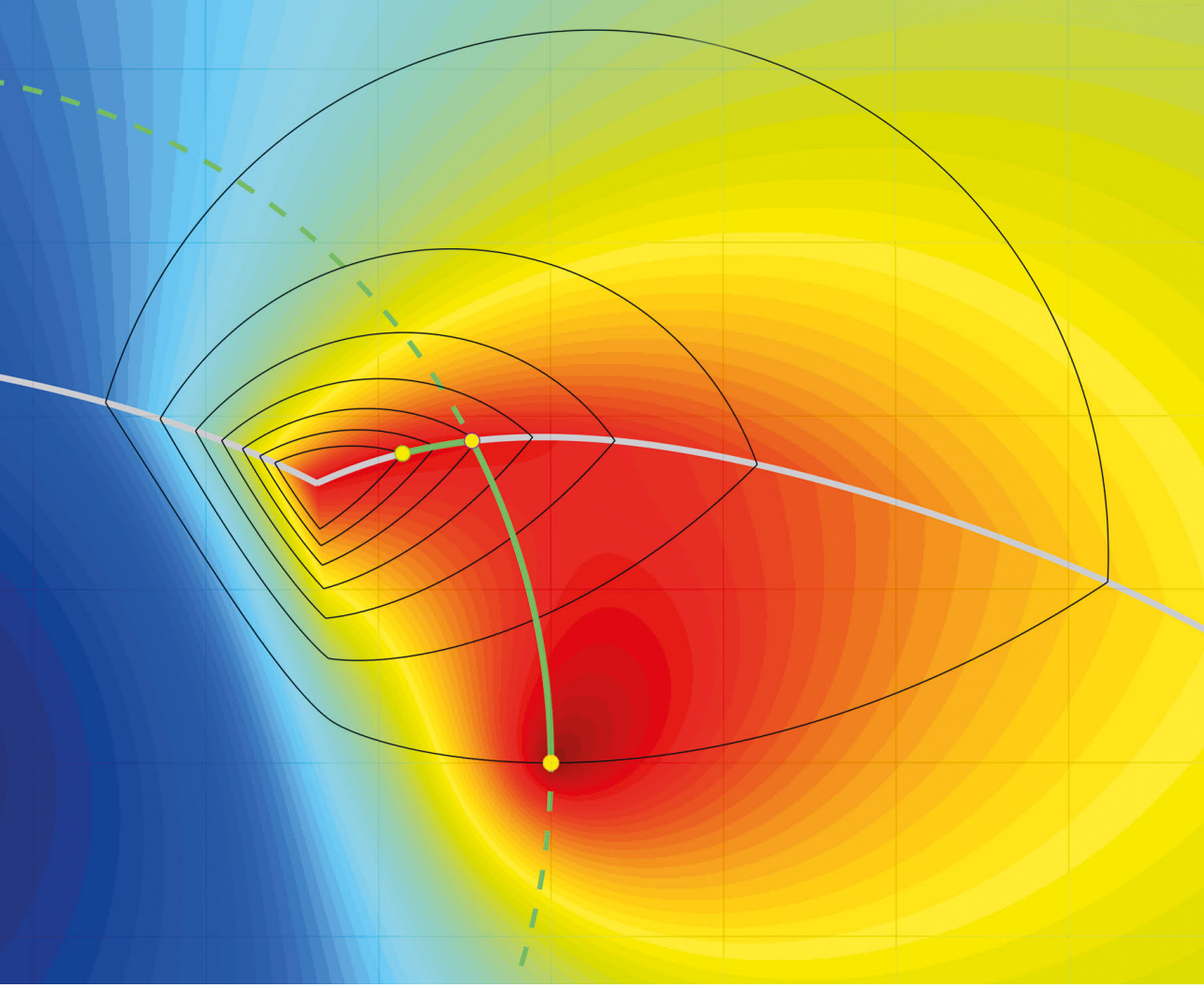

FAU Forschungen, Reihe B, Medizin, Naturwissenschaft, Technik 26

Christian Karl Musolff

Wideband Active Load Modulation in RF Power Amplifiers

FAU UNIVERSITY PRESS

Christian Karl Musolff

Wideband Active Load Modulation in RF Power Amplifiers

FAU Forschungen, Reihe B
Medizin, Naturwissenschaft, Technik
Band 26

Herausgeber der Reihe:
Wissenschaftlicher Beirat der FAU University Press

Christian Karl Musolff

Wideband Active Load Modulation in RF Power Amplifiers

Erlangen
FAU University Press
2019

Bibliografische Information der Deutschen Nationalbibliothek:
Die Deutsche Nationalbibliothek verzeichnet diese Publikation in der Deutschen Nationalbibliografie; detaillierte bibliografische Daten sind im Internet über http://dnb.d-nb.de abrufbar.

Bitte zitieren als
Musolff, Christian Karl. 2019. *Wideband Active Load Modulation in RF Power Amplifiers.* FAU Forschungen, Reihe B, Medizin, Naturwissenschaft, Technik Band 26. Erlangen: FAU University Press, DOI: 10.25593/978-3-96147-206-2.

Autoren-Kontaktinformation: musolff@ieee.org,
https://orcid.org/0000-0002-1397-4619

Der vollständige Inhalt des Buchs ist als PDF über den OPUS Server der Friedrich-Alexander-Universität Erlangen-Nürnberg abrufbar:
https://opus4.kobv.de/opus4-fau/home

Verlag und Auslieferung:

FAU University Press, Universitätsstraße 4, 91054 Erlangen

Druck: Digital Print Group GmbH

ISBN: 978-3-96147-205-5 (Druckausgabe)
eISBN: 978-3-96147-206-2 (Online-Ausgabe)
ISSN: 2198-8102
DOI: 10.25593/978-3-96147-206-2

Wideband Active Load Modulation in RF Power Amplifiers

Breitbandige aktive Lastmodulation in Hochfrequenzleistungsverstärkern

Der Technischen Fakultät
der Friedrich-Alexander-Universität
Erlangen-Nürnberg
zur
Erlangung des Doktorgrades Dr.-Ing.

vorgelegt von

Christian Karl Musolff

aus Köln

Als Dissertation genehmigt
von der Technischen Fakultät
der Friedrich-Alexander-Universität Erlangen-Nürnberg
Tag der mündlichen Prüfung: 19.11.2018

Vorsitzender des Promotionsorgans: Prof. Dr.-Ing. Reinhard Lerch

Gutachter: Prof. Dr.-Ing. Georg Fischer
PD Dr. rer. nat. Rüdiger Quay

To my beloved family, Thore, Charlotte, Erik and Miriam.

Take ye therefore good heed unto yourselves; for ye saw no manner of similitude on the day that the LORD spake unto you in Horeb out of the midst of the fire...

- Deuteronomy, 4:15

Zusammenfassung

Die vorliegende Dissertation behandelt das Thema der breitbandigen aktiven Lastmodulation in Hochfrequenzleistungsverstärkern vor dem Hintergrund des Einsatzes als Sendeverstärker in Mobilfunkbasisstationen. Im Zuge der auch international stetig fortschreitenden Zuteilung von Frequenzressourcen an die Mobilfunknetze sowie dem Wunsch nach einer weiteren Flexibilisierung des Netzbetriebs ergibt sich für die Infrastrukturanbieter der Bedarf nach einer nativen Unterstützung eines Multiband- und Multistandardbetriebs in ihren Produkten. Um die potentiellen Vorteile eines flexibleren Netzbetriebes, wie beispielsweise eine Optimierung der Netzkapazität sowie eine Senkung der Investitions- und Betriebskosten, u.a. durch Erhöhung der Energieeffizienz, voll abschöpfen zu können, muss eine Unterstützung des Multiband- und Multistandardbetriebs bereits auf der Ebene des Hochfrequenzfrontends der Basisstation umgesetzt werden. Die Leistungsverstärker nehmen dabei eine Schlüsselposition ein, da sie durch ihre Energieeffizienz und Bandbreite maßgeblich die Performanz des Gesamtsystems bestimmen, gleichzeitig aber aufgrund der vielfältigen Anforderungen auch die größten technischen Hürden bei der Realisierung des Multiband- und Multistandardbetriebs aufstellen.

Die Technik der aktiven Lastmodulation wird in Hochfrequenzleistungsverstärkern zur Erhöhung der Energieeffizienz im Teillastbereich eingesetzt, um bei der Verstärkung moderner Kommunikationssignale, die zumeist sehr hohe Scheitelfaktoren aufweisen, eine akzeptable Gesamteffizienz zu erzielen. Aufgrund ihrer inhärenten Linearität sowie ihres hervorragenden Effizienzpotentials stellt die auf aktiver Lastmodulation basierende Doherty-Architektur deshalb die inzwischen am weitesten verbreitete Schaltungslösung im Bereich der Sendeverstärker für Mobilfunkbasisstationen dar. Die Doherty-Architektur unterliegt allerdings einigen wohlbekannten, sowohl prinzipiellen als auch implementierungsbedingten Bandbreitenbeschränkungen, die die nutzbare relative Bandbreite praxisnaher Implementierungen bei Spitzenleistungen im Bereich einiger hundert Watt i.d.R. auf Werte von unter 20 % begrenzen.

In der vorliegenden Arbeit wird eine neuartige Methodik zur Analyse der breitbandigen aktiven Lastmodulation entwickelt, die ein umfassendes, deutlich über die in der Literatur zu findenden Teilbetrachtungen hinausgehendes Verständnis des Problems ermöglicht. Durch die Rückführung der, aus der aktiven Lastmodulation resultierenden, virtuellen Terminierungsimpedanzen auf einen komplexen Lastmodulationsfaktor und anschließender Anwendung eines Begrenzungsoperators auf die intrinsischen Wellenformen der Verstärkerkerne ist es gelungen, den von den Drainstromvektoren aufgespannten 3-dimensionalen Lastmodulationsraum auf eine 2-dimensionale, komplexe Lastmodulationsebene abzubilden. Die Darstellung der Ausgangsleistung und Effizienz des Verstärkers in der komplexen Lastmodulationsebene eröffnet einen anschaulichen Blick auf das Breitbandverhalten und ermöglicht dabei einerseits ein intuitives Verständnis des Einflusses der Ansteuerfunktionen, andererseits aber auch eine von der Auswahl einer expliziten Steuerfunktion unabhängige Betrachtung des Breitbandverhaltens eines gegebenen Ausgangsnetzwerkes. Die Methode ist dabei nicht auf die Doherty-Architektur beschränkt, sondern auf alle Verstärkerarchitekturen mit aktiver Lastmodulation anwendbar, unter der Bedingung, dass mindestens ein Verstärkerkern in Spannungssättigung betrieben wird und das Ausgangsnetzwerk verlustfrei und reziprok ist. Für den Klasse-B Fall (höhere Harmonische kurzgeschlossen) erfolgt eine vollständige, analytische Beschreibung der Lastmodulationsebene und der darin identifizierten, charakteristischen Strukturen, wie beispielsweise der Konturen konstanter Ausgangsleistung, der equi-clip Kontur und des Verlaufs der linearen Steuerfunktion. Die so entwickelten Analysewerkzeuge konnten unter Zuhilfenahme numerischer Methoden auch auf den Klasse-J Fall (reaktives Terminierungskontinuum für die 2. Harmonische) übertragen werden. Es ist auf diese Weise erstmalig gelungen, den breitbandigen Klasse-J Betrieb unter aktiver Lastmodulation exakt zu beschreiben und seine Vorteilhaftigkeit nachzuweisen. Die praktischen Auswirkungen der betrachteten Lösungsansätze werden anhand umfangreicher Parameterraumstudien untersucht und verglichen. Darüber hinaus konnte mithilfe der in der Arbeit entwickelten Analysewerkzeuge insbesondere die überragende Bedeutung der Steuerfunktionen für die breitbandige aktive Lastmodulation detailliert herausgearbeitet werden. Dabei wurde gezeigt, dass für das verstimmte Doherty-Ausgangsnetzwerk ein Übergang vom linearen Doherty-Modus in einen nichtlinearen Quasi-Outphasing-Modus im Amplitudenbereich existiert, der wesentliche Auswirkung auf die zu verwendenden Steuerfunktionen hat.

Die Stichhaltigkeit und Zweckmäßigkeit der gewonnenen Erkenntnisse wird anschließend anhand eines im Rahmen der Arbeit entwickelten, breitbandigen Doherty-Leistungsverstärkers mit einer maximalen Ausgangsleistung von 300 W im Frequenzbereich 680 - 1020 MHz, entsprechend einer relativen Bandbreite von 40 %, demonstriert. Dabei konnte insbesondere die durch Theorie und Simulation vorhergesagte Existenz eines Doherty-Outphasing-Übergangs messtechnisch nachgewiesen und insgesamt ein Performanzniveau erreicht werden, das deutlich über den Stand der Technik hinausgeht.

Abstract

The topic of this dissertation is wideband active load modulation in RF power amplifiers with an intended use in cellular base station applications. In the course of the continuing reallocation of new spectrum resources to the cellular networks and a general trend towards more flexible network operation, the providers of cellular network infrastructure face an increasing demand for a native support of multi-band and multi-standard operation scenarios in their products. In order to fully exploit the potentials of a more flexible network operation, like the optimization of network capacity, increased energy efficiency and a reduction of capital and operational expenditures, a genuine support of the multi-band and multi-standard operation must be implemented at the hardware level of the base transceiver station. The RF power amplifier takes a key position in this endeavour, because its energy efficiency and bandwidth is crucial to the overall system performance, while at the same time it poses significant technical obstacles to the implementation of wideband operation.

The active load modulation technique is used in order to increase the backoff efficiency of RF power amplifiers, which becomes necessary considering the very high peak-to-average power ratios present in modern communication signals, that could otherwise not be transmitted efficiently. Due to its inherent linearity and excellent efficiency potential, the Doherty architecture, which is based on active load modulation, has become the most widespread circuit topology used in the transmitter chain of cellular base transceiver stations today. However, this architecture is subject to some theoretical as well as practical bandwidth limitations that restrict its usage in practical base station applications with peak power levels of several hundred Watts to relative bandwidths that are typically well below 20 %.

In the present work, a novel method of analysis is developed, which enables a comprehensive understanding of the wideband active load modulation problem that goes distinctly beyond the partial approaches found in the literature. By means of reducing the virtual termination conditions that result from active load modulation to a complex load modulation factor and subsequent application of a clipping operator to the intrinsic waveforms of the amplifier

cores, the three-dimensional load modulation space spanned by the drain current vectors is mapped to a two-dimensional, complex load modulation plane. The representation of the amplifier's output power and efficiency on the complex load modulation plane opens up a demonstrative view on the bandwidth behaviour of the amplifier and enables an intuitive understanding of the role of the input drive functions in wideband active load modulation. On the other hand, it also allows for the assessment of the bandwidth behaviour of a given combiner circuit without relying on the explicit choice of a certain drive function. The methodology is not limited to the Doherty architecture, but can be applied to any active load modulation topology, provided that the combiner is lossless and reciprocal and that at least one amplifier core is operated in voltage saturation. A complete analytical description of the complex load modulation plane and the characteristic structures defined therein, like constant power contours, the equi-clip contour and the linear drive function circle, is provided for the Class-B case (higher harmonics shorted). Based on numerical methods, the tools of analysis developed for the Class-B case are then extended to the Class-J case (continuous, reactive termination conditions for the 2nd harmonic), which, for the first time, allowed a complete analysis of Class-J operation under active load modulation and demonstrated the advantage of its use in Doherty-type RFPAs. The practical consequences of the different approaches are assessed and compared by means of comprehensive design space analyses. Moreover, the tools of load modulation space analysis developed in this work provide significant insight into the crucial role of the drive functions in wideband active load modulation RFPAs, revealing, among other things, that a transition from the linear Doherty mode to a non-linear 'quasi-outphasing' mode in amplitude domain exists for the detuned Doherty combiner.

The soundness and utility value of the theoretical findings is demonstrated through a wideband active load modulation RFPA designed in the course of this work, with a full state output power of 300 W in the frequency range of 680 - 1020 MHz, corresponding to a relative bandwidth of 40 %. The measurement results obtained from this demonstrator show an overall level of performance that goes distinctly beyond the state of the art and, in particular, verify the presence of a transition from the linear Doherty mode to a non-linear 'quasi-outphasing' mode, as predicted by theory and simulation.

Acknowledgements

First and foremost, I wish to express my gratitude towards my wife Miriam who took care of our children practically on her own in the past year, which I spent designing the RFPA demonstrator presented in chapter three and preparing this thesis. I extend this thanks to the rest of my family, especially to my mother and to my sisters-in-law, who supported us a lot during this time.

Furthermore, I wish to express my sincere thanks to

- ... my academic supervisor and mentor, Prof. Dr.-Ing. Georg Fischer, for his guidance and support throughout my time at the Institute for Electronics Engineering. In countless discussions and consultations he provided me with valuable insights and ideas, which contributed a lot to my personal and professional development,
- ... Prof. Dr.-Ing. Dr.-Ing. habil. Robert Weigel, the head of the Institute for Electronics Engineering, who, upon our first meeting at the International Microwave Symposium 2010 in Anaheim, invited me to do a PhD at his institute, which I gratefully accepted. During my time in Erlangen, he always supported me in a generous way and conveyed to me a spirit of entrepreneurship, which I feel will be important to my future career,
- ... PD Dr. rer. nat. Rüdiger Quay for accepting to review this thesis and for the many enlightening discussions that we had since our first encounter in 2009,
- ... Prof. Dr.-Ing. Rainer Kronberger and Prof. Dr.-Ing. Jürgen Schneider, my professors and mentors during my undergraduate studies in Cologne, who taught me a lot about RF, circuit design and amateur radio, showed me how to put my talent in tinkering with electronic circuitry to reasonable use [E1], introduced me to the MTT-S and encouraged me to pursue a PhD,

... Dr.-Ing. Tilman Felgentreff, Hartmut Müller and Helmut Heinz of Nokia, Ulm, for their steady support and approval of my research, without which this work would not have been possible,

... Thomas Ackermann, who succeeded me as the leader of the institute's RFPA team and keeps up my research in the field of wideband active load modulation with a new focus on advanced system identification and predistortion techniques. He made invaluable contributions to this work by assisting me in the assembly of the wideband dual-input Doherty PA demonstrator and by setting up and operating the signal processing equipment which is used for the measurements of the demonstrator.

... my colleagues, former colleagues, team members, research partners and friends, Dr.-Ing. Michael Kamper, Wolfgang Akstaller, Dr.-Ing. Daniel Markert, Daniel Popp, Marco Dietz, Florian Trenz, Andreas Bauch, Dr.-Ing. Giovanni Donati, Dr.-Ing. Giuseppe Gottardo, Dr.-Ing. Ahmed Elmaghraby, Dr.-Ing. Zeid Abou-Chahine, Hartmut Hirsch, Christopher Beck, Dr.-Ing. Amelie Hagelauer, Fabian Lurz, Prof. Dr.-Ing. Alexander Kölpin, Gabriele Köhnen, Aurélia Martinek, Mathias Otto and many others, for the fruitful discussions and collaborations, shared ideas and insights and the good times we had together.

Contents

1 Introduction

1.1 Motivation and outline of this work

This dissertation is the result of the author's research activity at the Institute for Electronics Engineering of the Friedrich-Alexander-University Erlangen-Nuremberg, where he worked as a research assistant from 2011 to 2018 and established the institute's RFPA research group in 2015, which he led until 2018. The topic of the dissertation, wideband active load modulation in RFPA's, originates from a research cooperation between the Institute for Electronics Engineering and Nokia, Ulm.

As one of the largest providers of cellular network infrastructure in the world, Nokia has to face an increasing demand for higher operational bandwidth capabilities in the RF frontends of their cellular base transceiver stations. In the past two decades, general technological progress, the advance of the internet, a change of lifestyles and the appearance of new business models transformed cellular mobile radio from a rather simple telephone service to a universal data communication platform with exponential growth rates [1]. The Cisco Visual Networking Index (VNI) Global Mobile Data Traffic Forecast predicts a sevenfold increase of overall mobile data traffic in the years 2016 to 2021 [2]. The ever increasing need for data transmission capacity is met by a continuous advancement of communication standards, which aims at utilizing existing spectrum resources more efficiently, but, ultimately, also by the reallocation of new spectrum resources to the cellular networks. A typical, recent example is the reallocation of spectrum that becomes available in the course of the transition to digital terrestrial television broadcast (DVB-T), known under the term 'Digital Dividend'. The spectrum allocation on an international scale is even more diverse (s. Table 1.1) and individual frequency bands are also not bound exclusively to a single communication standard anymore, as they were in the early era of cellular mobile communications, but the coexistence of different communication standards (e.g. GSM and LTE) on the same frequency band will become a reality.

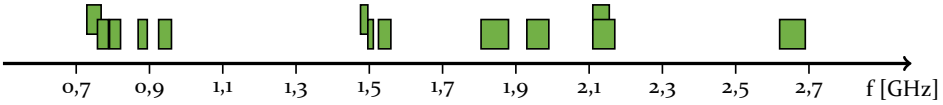

E-UTRA band	Downlink frequency range [MHz]	Designation	Standard	Region
12 - 17	729 - 768	SMH	GSM, UMTS, LTE	AMN
28	758 - 788	Digital Dividend II	GSM, LTE	EU, AS, OZE
20	791 - 821	Digital Dividend I	GSM, LTE	EU, AS, OZE, AFR
5	869 - 894	CLR	GSM, LTE	AMN, AS, OZE
8	925 - 960	E-GSM, GSM900	GSM, UMTS, LTE	EU, AS
11	1476 - 1496	LPDC	GSM, UMTS, LTE	Japan
21	1496 - 1511	UPDC	GSM, UMTS, LTE	Japan
24	1525 - 1559	L-Band	UMTS, LTE	AMN
3	1805 - 1880	DCS, GSM1800	GSM, LTE	EU, AS, AFR, OZE
2	1930 - 1990	PCS	GSM, LTE	AMN
4	2110 - 2155	AWS	GSM, LTE	AMN
1	2110 - 2170	IMT, UMTS-Band	UMTS, LTE	EU, AS, AFR, OZE
7	2620 - 2690	IMT-E, LTE-Band	LTE	worldwide

Table 1.1: Summary of the most important cellular radio downlink bands in use today

In consequence of these developments, the multi-band and multi-standard operation scenario is expected to become much more relevant in the future, also on the base station side. The desire for a more flexible allocation of resources already manifests itself today in techniques like inter/intra-band Carrier Aggregation in LTE or supplementary Downlink in HSPA+. The prospect of a generally more flexible network operation holds great promise, as the ability to allocate infrastructure and spectrum resources adaptively and dynamically will ultimately lead to a more efficient network operation. The network capacity can be optimized and operational as well as capital expenditures can be reduced. From a commercial perspective, recent trends like site-sharing and managed-services, where the ownership and operation of network infrastructure and spectrum resources is detached from the assignment of those resources, give evidence that the market participants are indeed willing to take advantage of the potentials associated with a more flexible network operation. However, in order to fully exploit these potentials, a native support of multi-band and multi-standard operation at the hardware level of the base transceiver station is yet to be implemented. It is the analogue RF

frontend, in particular the RFPA, that determines the operational costs of the base station with its power consumption and also makes up a large part of the manufacturing costs.

Even the conventional, narrowband operating scenario poses challenging and conflicting requirements on the RFPA in the cellular base station. Today's communication standards are designed with a main focus on efficient spectrum usage, which results in very strict requirements on the linearity of the transmitter signal chain and signal statistics with a very high peak-to-average power ratio. These signal statistics, in conjunction with fluctuating network loads, lead to a situation in which the RFPA must be able to provide an instantaneous peak output power that is more than ten times higher than its average output power. Under such conditions, a conventional RFPA will operate very inefficiently. Thus, as the energy efficiency of the RFPA is of key importance to the power consumption of the entire base station, the primary objective in the design of the RFPA is to increase its average efficiency despite the challenging signal conditions that it has to face.

State-of-the-art RFPAs for cellular base transceiver stations use advanced techniques like active load modulation in the form of the Doherty architecture, waveform engineering and digital predistortion in order to achieve efficient and linear power amplification. The Doherty architecture is the most widespread RFPA architecture in cellular base transceiver stations today, because it is ideally suited for the amplification of high PAPR signals due to its inherently sequential operating principle, while at the same time it maintains a sufficient level of linearity and its implementation is comparatively inexpensive and convenient. Although the Doherty architecture in its traditional form is subject to some well-known bandwidth limitations that restrict its usage to bandwidths below one octave, moderately wideband solutions, with relative bandwidths in the range of 30 - 40 %, are conceivable in theory. Such solutions would be sufficiently able to cover multi-band operation in neighbouring frequency bands, as indicated in Table 1.1, or full-band operation in wider, continuous frequency bands than today's, which are expected to become more relevant in the future, and are therefore highly desirable. The practical implementations that are used in today's base transceiver stations, however, are unable to utilize the architecture's theoretical bandwidth potential. They are typically designed for single-band operation with relative bandwidths of 10 % or even less. The goal of the present work is to overcome this discrepancy by opening up new ways to significantly increase the operational bandwidth capabilities of practical Doherty PA implementations without sacrificing the architecture's superior efficiency and linearity characteristics. The specific

question of bandwidth limitations in Doherty PA's has been in the focus of academic and industrial research for many years. Most of the sources of bandwidth limitations in the Doherty PA have been addressed individually and numerous techniques to enhance the bandwidth capabilities of the architecture have been proposed. However, the analysis presented in previous works very often lacks generality, because restrictive and sometimes even inconsistent assumptions are made. An intuitive understanding of the important role of the input drive functions seems to be missing in the literature. With the present work, the author aims at improving that situation by developing a more comprehensive and demonstrative understanding of the active load modulation problem.

The work is outlined as follows: In the remainder of chapter one, the basic principles of RFPAs and active load modulation, as far as they are relevant to the understanding of this work, will be recapitulated briefly. For a more comprehensive introduction to RFPA design, the reader is kindly referred to the numerous, good textbooks and review articles that are available on this topic [3]–[8]. Chapter two constitutes the main part of this work. A new approach to the analysis of the wideband active load modulation problem will be presented, which enables a demonstrative representation of the amplifier's performance parameters in two dimensional load modulation space. It allows for the assessment of the detuned amplifier's performance under active load modulation, without relying on the explicit choice of an input drive function. In the course of analysis, valuable insights on the nature of wideband active load modulation itself are gained, like the existence of a transition from the linear Doherty mode to a non-linear 'quasi-outphasing' mode, that occurs in the detuned Doherty PA. The approach is then extended to the Class-J case, incorporating the 2nd harmonic termination into the analysis and examining its effect on wideband active load modulation. Finally, an extensive combiner design space analysis for the Doherty variants treated in this work is presented in order to assess and compare their potential performance in wideband applications, including an enlightening discussion on boundary conditions. Chapter three presents a successful design of a wideband active load modulation RFPA demonstrator with a full state output power of 300 W in the frequency range 680 - 1020 MHz, corresponding to a relative bandwidth of 40 %. The demonstrator design is based on the theoretical findings presented in chapter two and substantiates the soundness and utility value of these findings. Chapter four concludes the dissertation with a discussion of the results and an outlook on ongoing and future research opportunities that arise from this work.

1.2 RFPA basics

The most basic implementation of a linear RFPA thinkable is the **Class-A power amplifier**. Its operating point is set to the center of the linear dynamic range and the amplifier is driven symmetrically around that point. It works essentially like a small-signal amplifier that is driven over its whole dynamic range. Under the assumption of a linear transfer function, the voltage and current waveforms are perfectly sinusoidal. If we set the DC voltage and current bias to $U_{DC} = I_{DC} = 1$ and introduce a normalized linear excitation amplitude $0 \leq \overline{in} \leq 1$, the efficiency of the ideal Class-A amplifier follows as

$$\eta_A\left(\overline{in}\right) = \frac{P_{out}}{P_{DC}} = \frac{\frac{1}{\sqrt{2}} U_{f_0} \frac{1}{\sqrt{2}} I_{f_0}}{U_{DC} I_{DC}} = \frac{\frac{1}{\sqrt{2}} \overline{in} \frac{1}{\sqrt{2}} \overline{in}}{1} = \frac{1}{2} \overline{in}^2 \tag{1.1}$$

As a consequence of the symmetric excursion around the operating point, the DC components at the current generator plane of the Class-A amplifier are independent of the actual drive level. The DC power it draws from the supply is constant, regardless of the drive level and regardless of how good or bad the load match is. It is a peculiarity of the Class-A amplifier that its power dissipation is actually the highest when its not driven at all. The more power it generates at the load, the less power it has to dissipate. It reaches its maximum efficiency of 50 % when it's fully driven and perfectly matched.

In order to understand how the RFPA's efficiency affects the overall power efficiency of the transmitter system, the **amplitude statistics** of the signals to be transmitted must be considered. The modulation techniques that are used in modern cellular radio standards are primarily designed for maximum spectral efficiency, which tends to result in a normal distribution of the I and Q amplitudes. With regard to the multi-band and multi-standard scenario, the Central Limit Theorem predicts that the sum of a large number of independent random variables will also tend towards the normal distribution, even if the variables themselves are not normally distributed. Thus, it is reasonable to assume a normal distribution of the I and Q components of the complex baseband signal and, as a result, a Rayleigh distribution of the RF amplitude. The probability density function of the Rayleigh distribution is illustrated in Figure 1.1[1]. The problem with this type of signal is that, in theory, the amplitude can become infinitely high. Since it is not feasible to transmit a

[1] Note that Figure 1.1 shows the Rayleigh amplitude distribution, as is usual in this context. For the calculation of average efficiency, the Rayleigh power distribution is used (s. eq. 2.101 on p. 33). Those two functions are quite different, which might seem counter-intuitive at first glance [9].

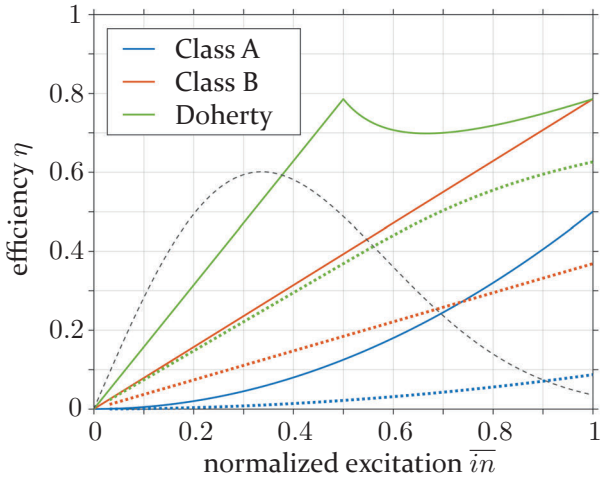

Figure 1.1: Power efficiency for the CW (solid) and for a 7.5 dB Rayleigh signal (dotted). The dotted gray line illustrates the probability density function of the 7.5 dB Rayleigh signal (unscaled).

signal with infinite peak power, crest factor reduction techniques are applied in order to reduce the peak-to-average power ratio to practical levels in the range of 7 - 10 dB. Nevertheless, these values are still very high with regard to efficient power amplification. With a 7.5 dB PAPR Rayleigh signal to be amplified, the ideal Class-A PA reaches a maximum average efficiency of only 8.7 %. Considering the amplitude statistics of the Rayleigh signal, it becomes clear that the reason for the very low average efficiency is not primarily the 50 % peak efficiency, but the fact that, in backoff, the efficiency of the Class-A amplifier falls with the square of the amplitude, because its DC input power remains constant.

A crucial step to increase the average efficiency of the RFPA is to reduce its DC bias current. Reducing it to $I_{DC}(0) = 0$ gives us an ideal **Class-B power amplifier**, with the efficiency

$$\eta_B(\overline{in}) = \frac{P_{out}}{P_{DC}} = \frac{\frac{1}{\sqrt{2}} U_{f_0} \frac{1}{\sqrt{2}} I_{f_0}}{U_{DC} I_{DC}} = \frac{\frac{1}{\sqrt{2}} \overline{in} \frac{1}{\sqrt{2}} \overline{in}}{\frac{2}{\pi} \overline{in}} = \frac{\pi}{4} \overline{in} \tag{1.2}$$

In addition to its higher full state efficiency of 78.5 %, the efficiency of the Class-B amplifier falls only proportionally to the amplitude in backoff, resulting in a significantly higher average efficiency of 36.9 % for the 7.5 dB Rayleigh signal. But there is another implication to the Class-B amplifier. As

the active device in the amplifier can conduct current only in one direction, the reduction of the DC bias current is equivalent to a reduction of the conduction angle. While the Class-A amplifier reproduces the entire waveform at its current generator plane, the Class-B amplifier will only conduct one half-wave of the cosine waveform. The conduction angle is thus reduced from 2π to π and since the current waveform of the **reduced conduction angle mode** is a cut-off sine pulse, it contains a significant amount of harmonics. The harmonic content of the reduced conduction angle mode waveforms will be discussed in more detail in section 2.1.2, but at this point we can already draw an important conclusion from the presence of higher harmonics with regard to the amplifier's bandwidth. In linear RFPA applications it is usually not acceptable to generate a significant amount of power at the load at higher harmonic frequencies. Thus, the output matching network of a single-ended, reduced conduction angle mode PA must provide separate terminations for the fundamental frequency component and for the higher harmonics, respectively. In case of the ideal Class-B amplifier, an intrinsic short circuit of the higher harmonic components is assumed, so that the intrinsic voltage waveform remains strictly sinusoidal and no power is generated at the higher harmonics. A separate termination of the harmonic components in a single-ended PA can only be realized if the harmonic frequency bands are distinguishable in frequency domain, which means that they may not overlap each other. This gives rise to the boundary condition

$$rel.\,BW \leq \frac{2}{2n-1} \tag{1.3}$$

with n denoting the order up to which the harmonic frequency bands shall be unambiguous. Table 1.2 illustrates this line of thought.

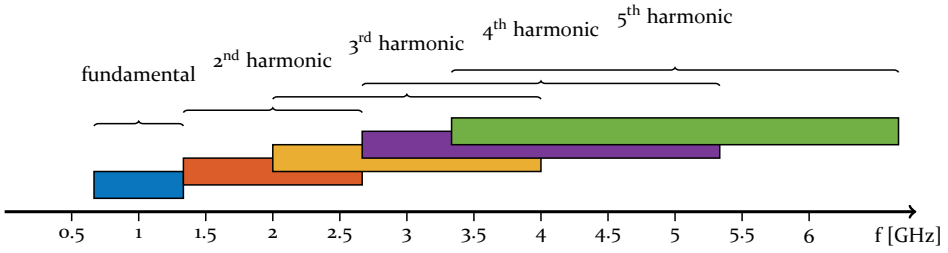

n	2	3	4	5
$rel.\,BW$	66.67 %	40 %	28.57 %	22.22 %

Table 1.2: Ambiguity of harmonic frequency bands (example drawn for a rel. BW of 66.67%)

The example above Table 1.2 illustrated that the bandwidth of the single-ended, reduced conduction angle mode RFPA is inherently **limited to one octave** (66.67% rel. BW), since the 2nd harmonic frequency band will overlap the fundamental frequency band at higher bandwidths [2]. In order to overcome this problem, two reduced conduction angle mode amplifier cores can be connected together in a **push-pull configuration** as shown in Figure 1.2. The two branches are driven in antiphase, so that, from a time domain perspective, each Class-B amplifier core would conduct one half-wave, resulting in a combined output current that is sinusoidal again. From a frequency domain perspective, the even numbered harmonics (DC, 2nd harmonic, etc.) appear at the even mode output port of the output combiner, while the odd numbered harmonics (fundamental, 3rd harmonic, etc.) appear at the odd mode output port. This allows the even numbered harmonics to be terminated separately from the odd numbered harmonics, as indicated in Figure 1.2, without having to separate them in frequency domain. Push-pull amplifier configurations are widely used in all fields of electronics, although in RFPA's their bandwidth capabilities are limited by the technical feasibility of a sufficiently wideband push-pull output combiner. The push-pull concept has been introduced here because it is helpful to the understanding of the reduced conduction angle modes and has an important place in wideband RFPA design [10]. With regard to the scope of this work, the bandwidth limitation imposed by the presence of higher harmonics does play a significant role, because the Doherty architecture strongly depends on reduced conduction angle mode operation, but it is only one bandwidth limiting factor among several others, which are more specific to active load modulation. Push-pull configurations will not be used in this work, although their application in active load modulation architectures is possible in theory and may be advantageous in some cases [11].

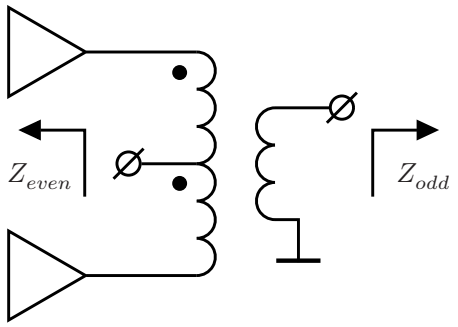

Figure 1.2: Push-pull configuration

[2] If the generation of power at higher harmonics at the load was acceptable, it would indeed be possible to design single-ended, reduced conduction angle mode RFPAs with higher bandwidths, but such a scenario is hardly relevant in radio communication applications. The use of an external filter between the RFPA and the load is not considered here, because that leads to rather philosophical questions about the definition of a wideband amplifier.

Aside from its detrimental effect on bandwidth, the presence of higher harmonics in the intrinsic current waveform of the active device can also be used to further improve the efficiency of the amplifier. By proper choice of the termination impedances of the respective harmonic components, the harmonic content of the intrinsic voltage and current waveforms can be controlled in such a way that the waveforms are further orthogonalized in time domain. Several such **waveform engineering techniques** exist, being known as Class-F, inverse Class-F or Class-E, to name the most important ones [6]. Waveform engineering has a very fundamental importance in RFPA design, since higher harmonic components are always present in practical RFPA implementations and therefore not dealing with harmonic terminations is not an option[3]. However, when it comes to increasing the average efficiency of a linear, wideband RFPA under high PAPR signal conditions, the prospects of these techniques are quite limited, because they tend to be inherently narrowband and nonlinear. The Class-F and inverse Class-F techniques in their original forms are defined by alternating intrinsic open and short circuit conditions for the higher harmonics [12]. In addition to the bandwidth limitation imposed by the ambiguity of the harmonic frequency bands (eq. 1.3), it is physically impossible to realize such termination conditions over an extended bandwidth because that would violate Foster's reactance theorem, which states that the reactance of a lossless, passive one-port increases strictly monotonically with frequency. To overcome this problem, the Class-F technique has been extended to continuous termination conditions that allow moderately wideband implementations [13], [14]. The Class-E technique, on the other hand, is defined by time-domain criteria and is therefore not bound to strictly narrowband harmonic termination conditions [15]. It can also be used in moderately wideband applications, but it still underlies the octave limit that follows from eq. 1.3. More critical than these bandwidth considerations is the fact that, in order to achieve efficiencies higher than the ideal Class-B efficiency of 78.5 % by means of waveform shaping, odd harmonics (3^{rd}, 5^{th}) must be present in the intrinsic waveforms. The presence of odd harmonics, in turn, necessitates non-linear operation of the PA. Class-F and Class-E are commonly categorized as **switched mode operation**, which means that the active device is significantly overdriven in order to approximate the desired

[3] The RFPA designer can choose to ignore them, resulting in suboptimal performance and limited repeatability. This has often been a problem in traditional RFPA designs, that were based solely on fundamental frequency loadpull data. In defence of the older generation of PA designers, it can be noted that the possibilities of active device modelling and simulation based design were not always as good as they are today.

switching behaviour. Nevertheless, since a certain amount of odd harmonics is always present in practical implementations of reduced conduction angle mode amplifiers [E2], waveform engineering techniques can be applied to linear RFPA's as well [E3], but the efficiency improvement will not be as significant as in switched mode operation, especially at backoff. The potential improvement in average efficiency under high PAPR signal conditions is therefore limited to a few percent.

Any meaningful attempt to further increase the average efficiency of the linear RFPA under high PAPR signal conditions must be aimed directly at increasing the RFPA's backoff efficiency. In a conventional RFPA, maximum efficiency is reached at full state power, when the fundamental drain voltage amplitude reaches its maximum. In order to extend the high efficiency power range, the voltage saturation condition must be maintained over an extended power range. There are two ways to do this, as can be seen from the very basic equation

$$P = \frac{U^2}{2R} \tag{1.4}$$

We can either adjust the drain voltage bias or the intrinsic load resistance along with the output power level. Both options are used in practice. Drain voltage modulation techniques are known under the terms **envelope tracking** (ET) [6] or envelope elimination and restoration (EER) [16]. These concepts use a separate modulation amplifier in order to generate a modulated supply voltage for the RFPA. The modulated supply voltage can either convey the full AM information of the signal to be transmitted, or a bandwidth limited version of it. As the modulator has to provide the necessary envelope power to the RFPA, the overall efficiency of the transmitter system is defined by the product of the RFPA efficiency and the modulator efficiency. Thus, in order to achieve favourable overall efficiency results, the modulator must be implemented as a highly efficient switched mode amplifier, which, in turn, limits its bandwidth capabilities. Another aspect that must be taken into account is that the ET concept is an inherently polar architecture, while the nature of the TX signal in a cellular base station is closer to the cartesian form. Converting it to a polar form results in a significant bandwidth expansion, which further limits the usable bandwidth of the ET concept [17]. After all, ET techniques can be very advantageous, but mostly so for narrowband signals and/or inherently polar modulation techniques and in particular for the low-power, integrated solutions that are used in handsets. With regard to the scope of this work - cellular base station applications with intended envelope bandwidths of

several hundred MHz and a full state power level of several hundred Watts - the ET concept did not seem advisable[4] and was therefore not pursued.

The other path to increase the backoff efficiency is to modulate the loadline resistance presented to the active device according to the output power level, such that the voltage saturation condition can be maintained in backoff. This can be implemented in a passive manner, by means of tunable reactive elements that change the transformation ratio in the output matching network of the amplifier. Such techniques are known under the terms **passive or dynamic load modulation** and are subject to similar disadvantages as the envelope tracking architectures, insofar as these are basically polar architectures as well, requiring highly heterogeneous signal paths with possible linearity and noise issues, especially at high bandwidths [18]–[21]. **Active load modulation**, on the other hand, is achieved by connecting two or more amplifier cores together using a non-isolating combiner. At least one of its implementations, the Doherty architecture, has significant advantages over the polar transmitter concepts introduced before. The Doherty architecture is the method of choice in most cellular base station applications today and provides the basis for this work.

1.3 Active load modulation

1.3.1 The Doherty architecture

The 1930's were the decade in which commercial radio broadcast finally grew out of its infancy and set out to become a mass medium. The output power levels of the AM transmitters used by large broadcast stations at that time reached hundreds of kilowatts and the power supply became the main factor in the operating costs of these stations [7], [22]. It is therefore not surprising that some of the most important inventions in the field of efficient transmitter design originate from this decade.

In 1936, William H. Doherty published his seminal paper named 'A new high efficiency power amplifier for modulated waves' [23] as a result of his work on high power transmitter designs for broadcast and radio telephone service at Bell Telephone Laboratories. In this paper, he follows the same line of thought as was introduced in the previous section: High efficiency RFPA operation

[4] A slow tracking of the drain bias supply voltage, aimed at accommodating fluctuating network loads, is indeed useful in base station applications, but that goes beyond the scope of this work.

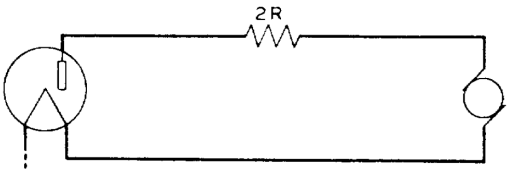

Figure 1.3: 'Insertion of a hypothetical source of additional voltage', taken from [23], © 1936 IEEE

is linked to the voltage saturation condition and thus the load resistance must be adjusted along with the output power in order to maintain voltage saturation and extend the range of high efficiency operation. But how can the load resistance be decreased while the output power supplied to the load is increasing? Doherty's answer is quite simple: By placing an additional voltage source in series to the load. Figure 1.3 shows Doherty's original drawing, illustrating his approach. The vacuum tube, representing the main RFPA core, shall be considered as an ideal current source, sourcing the current I_{Main}. In this circuit, the voltage across the load, $U_L = 2RI_{Main}$, is determined solely by I_{Main}. The output voltage of the additional voltage source, called a **peaking source**, U_{Peak}, has no direct effect on the load, but reduces the voltage across the current source, U_{Main}, and thus the effective load resistance seen by the current source

$$R_{Main} = \frac{U_{Main}}{I_{Main}} = \frac{2RI_{Main} - U_{Peak}}{I_{Main}} = 2R - \frac{U_{Peak}}{I_{Main}} \tag{1.5}$$

Assuming that the voltage across the current source, U_{Main}, is already saturated when the peaking voltage source comes into action, the peaking voltage U_{Peak} thus allows for a further increase of I_{Main}. If I_{Main} and U_{Peak} are increased simultaneously such that $\Delta U_{Peak} = 2R\Delta I_{Main}$, the voltage across the current source, U_{Main}, remains constant, while the output power increases to $2RI_{Main}^2$. This **load modulation mechanism** allows the main amplifier core to maintain a constant voltage saturation, while further increasing the power delivered to the load. Figure 1.4 shows the voltage and current functions that characterize the Doherty architecture, the resulting load profiles as seen by the amplifier cores and the output power contributions of the individual amplifier cores. At low power levels ('backoff region', $\overline{in} < 0.5$), only the main amplifier core is active and works into a load resistance of $2R$, which equals twice its full state load resistance. Due to the doubled load resistance, the main amplifier core reaches voltage saturation and thus maximum efficiency at half of its full state output current. When the output power is increased beyond that point ('Doherty region', $\overline{in} > 0.5$), the peaking voltage source is turned on, allowing I_{Main} to increase further while keeping U_{Main} constant, until both sources reach their full state load resistances and full state output

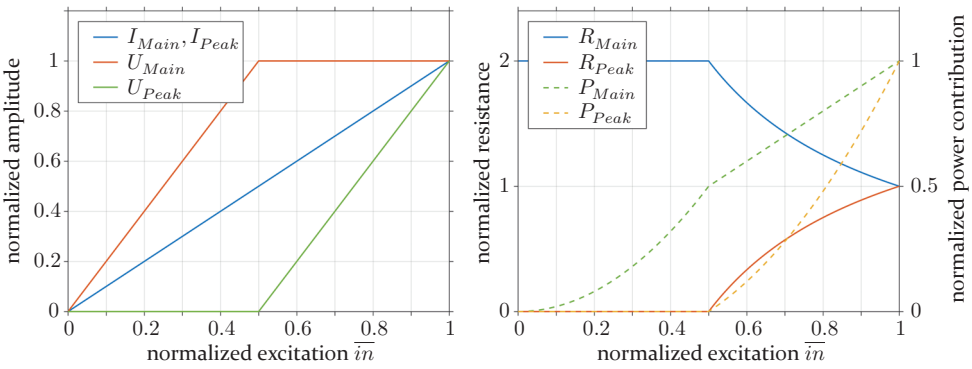

a) Main and Peak amplitudes

b) Load resistances and output power contributions

Figure 1.4: Typical Doherty characteristics for a circuit using a voltage mode peaking device

power. The resulting efficiency characteristic with its two distinct efficiency peaks is shown in Figure 1.1. For the 7.5 dB PAPR Rayleigh signal, the Doherty architecture produces an average efficiency of 62.6 %, as compared to 36.9 % for the ideal Class-B amplifier.

The circuit model that has been shown in Figure 1.3 can be seen as the most basic version of the Doherty architecture and is well suited to explain its operating principle, but it has a major problem connected to it. The 'insertion of a hypothetical source of additional voltage' is a very impractical thing to do, because all of the active devices that are available to the PA designer, be it vacuum tubes, BJT's or FET's, act as controlled current sources[5], exhibiting a high internal resistance when inactive . Fortunately, network theory offers a solution to this problem in the form of an **impedance inverting network**. An impedance inverting network is a two-port that swaps the voltage and current relations between its ports. It transforms an impedance Z into its dual impedance $1/Z$, or, in case of the Doherty amplifier, a current source into a voltage source. Probably the most common example of an impedance inverting network is the $\lambda/4$ transmission line transformer. The same function can also be realized using lumped element networks, which is usually done in lower RF frequency applications, like those in Doherty's original paper. With the help of the impedance inverting network, the auxiliary voltage source can be replaced by a regular amplifier core, as shown in Figure 1.5. The typical voltage and current functions, as well as the other characteristics shown in Figure 1.4 also

[5] With the exception of some highly sophisticated, integrated solutions like switched capacitor PA's [24].

apply to the modified circuit, with two exceptions: The voltage and current amplitudes at the peak amplifier core, U_{peak} and I_{peak}, are interchanged and, consequently, R_{Peak} starts at infinity instead of zero.

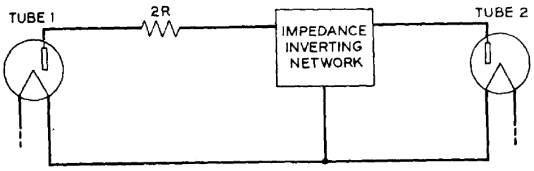

Figure 1.5: 'Fundamental form of a high efficiency circuit', taken from [23], © 1936 IEEE

The modified circuit is still somewhat impractical because it uses a series load, while in most applications a single-ended, ground referenced load would be preferable in order to allow for the connection of a coaxial feed line. At this point, the impedance inverting network helps us again. An impedance inverter with the characteristic impedance R transforms a series resistance of $2R$ connected to one of its port to a $1/2\,R$ parallel resistance connected to the other port, as demonstrated by the chain parameter equation

$$\underbrace{\begin{bmatrix} 1 & 2R \\ 0 & 1 \end{bmatrix}}_{\substack{\text{series} \\ \text{resistance}}} \underbrace{\begin{bmatrix} 0 & R \\ \frac{1}{R} & 0 \end{bmatrix}}_{\substack{\text{impedance} \\ \text{inverter}}} = \begin{bmatrix} 2 & R \\ \frac{1}{R} & 0 \end{bmatrix} = \underbrace{\begin{bmatrix} 0 & R \\ \frac{1}{R} & 0 \end{bmatrix}}_{\substack{\text{impedance} \\ \text{inverter}}} \underbrace{\begin{bmatrix} 1 & 0 \\ \frac{2}{R} & 1 \end{bmatrix}}_{\substack{\text{parallel} \\ \text{conductance}}} \tag{1.6}$$

Substituting the series load with a parallel load, we finally arrive at the circuit shown in Figure 1.6, which is the DPA variant that is commonly used, up to the present day [25]. The downside of using an impedance inverting network is that, unlike the ideal representation used in Eq. 1.6, practical impedance inverting networks like the $\lambda/4$ transmission line transformer introduce a $\lambda/4$ phase offset and exhibit a frequency response which limits the bandwidth of the DPA implementation.

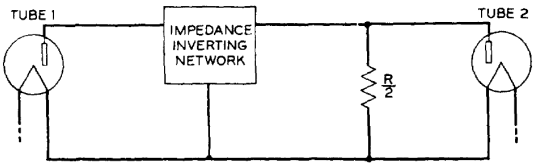

Figure 1.6: 'Second fundamental form of a high efficiency circuit', taken from [23], © 1936 IEEE

At microwave frequencies, the output capacitance of the active devices in conjunction with the bond wire inductances, package parasitics, bias feeds and, potentially, matching networks generates a significant offset length, which prevents a direct connection of the amplifier cores' intrinsic current generator planes to the Doherty combiner. To compensate for these effects,

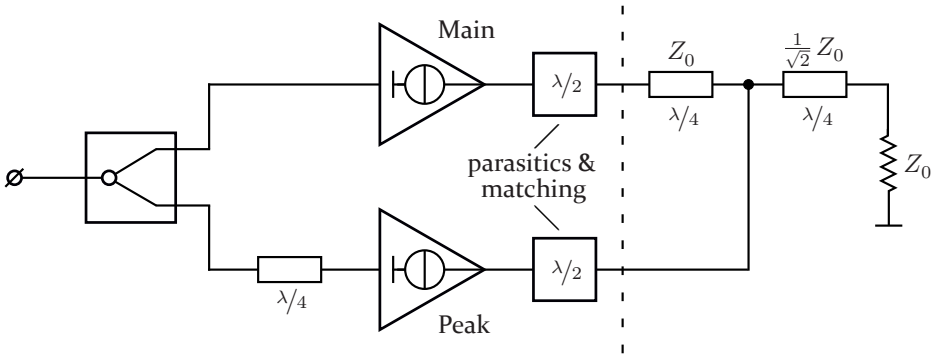

Figure 1.7: Conventional microwave DPA topology with parasitic offsets

offset lines are added in order to extend the parasitic offset lengths to $\lambda/2$, rendering them transparent for load modulation. Thus, in a conventional DPA implementation at microwave frequencies, the phase offset present between the intrinsic current generator planes of the main and peak devices and the common node of the Doherty combiner is $3/4\,\lambda$ and $\lambda/2$, respectively, instead of $\lambda/4$ and 0, as found in the ideal DPA (s. Fig.1.7).

Since a phase offset of $\lambda/4$ would be sufficient for the absorption of the active devices' parasitics in the majority of cases, the $3/4\,\lambda$ phase offset in the main branch is unnecessarily long, resulting in reduced bandwidth and increased circuit size. In order to remedy this issue a so called **inverted DPA** topology [26] can be used, which implements a $\lambda/4$ phase offset between the main amplifier core's intrinsic current generator plane and the common node of the combiner and a $\lambda/2$ phase offset between the peak amplifier core's intrinsic current generator plane and the common node of the combiner, as depicted in Fig. 1.8. The inverted DPA topology essentially uses the parasitic offset present in the main path as a $\lambda/4$ impedance inverter and creates a $\lambda/2$ offset in the peak path. Strictly speaking, this is by no means an independent circuit topology, but just a regular Doherty PA in which the definition of the combiner reference plane has been shifted. In the author's experience, the definition of reference planes in the Doherty architecture has often been the cause of misunderstanding, confusion and misconceptions. From the perspective of bandwidth analysis, it does not make much sense to distinguish between the package plane of the active device, some kind of matching networks and the Doherty combiner. Thus, the analysis in the present work strictly refers to the intrinsic current generator planes of the active devices and it is assumed that the active devices' output parasitics will later be absorbed in the combiner network during network synthesis.

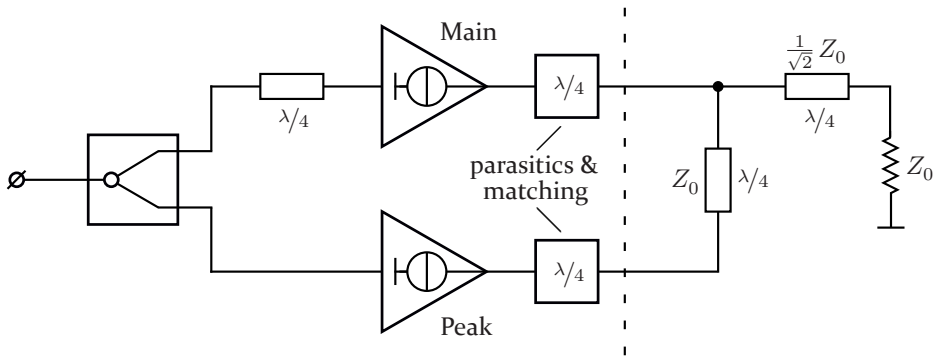

Figure 1.8: Inverted DPA topology

In line with Doherty's original paper, a DPA with equally sized amplifier cores has been assumed so far, commonly termed a **symmetric DPA**, resulting in an onset of load modulation and a first efficiency peak at 6 dB output power backoff. It is also possible to design **asymmetric DPA** variants, which allows to shift the first efficiency peak towards higher backoff power ratios than 6 dB. This is especially desirable in order to further increase the average efficiency when facing very high peak to average power ratios of 10 dB or more. The relationship between the backoff power ratio, the full state current ratio and the combiner parameters of the DPA will be discussed in detail in section 2.1.6, complemented by a discussion on asymmetric DPAs in section 3.1. Another way to increase the high efficiency power range beyond the capabilities of the classic DPA is to extend the Doherty principle to a three-way or, more generally, to an **n-way DPA**, comprising three or more amplifier cores. This is achieved by replacing either the main or the peak amplifier core of the DPA with another DPA in a recursive manner. Such designs are outside the scope of this work and will therefore not be further discussed, but a good overview can be found in [27], [28].

Among other things, it is the inherent **sequentiality** in the driving scheme that gives the Doherty PA an efficiency advantage over other high efficiency transmitter architectures in practical applications, because it effectively reduces the active device size at deep backoff. While in most other high efficiency transmitter concepts the entire active device periphery remains active and potentially wastes energy, the peak amplifier core of the Doherty transmitter is completely shut down at deep backoff. The sequential turn-on of the peak amplifier core and a high off-state resistance at deep backoff is achieved by biasing the active device in Class-C. In traditional, analogue DPA implementations, the input signal is split between the main and peaking amplifier path

by means of a linear power divider. In addition, a $\lambda/4$ delay line is included at the input of the peak amplifier core in a conventional DPA or at the input of the main amplifier core in an inverted DPA, in order to compensate for the phase shift generated by the impedance inverting network in the Doherty combiner (s. Figs. 1.7 and 1.8). While the traditional, analogue input signal splitter can provide an adequate input drive function to a narrowband DPA implementation, it does not leave much freedom for the alignment of the drive function's frequency response. Practical wideband DPA implementations require frequency responses of the drive functions that are significantly different from those that can be generated using a traditional input signal splitter. As a consequence of the continuing advances in the field of digital-to-analogue converter implementations and digital signal processing hardware, a mixed-signal approach that uses individual signal generation and up-conversion chains to drive the main and peaking branches of the DPA becomes more and more attractive. This **dual-input DPA**[6] concept enables the generation of arbitrary input drive functions in digital baseband and is therefore highly advantageous in the design of wideband DPAs.

Aside from the aforementioned aspects of impedance inverter implementation, active device parasitics and suitable wideband drive functions, there are several other factors that affect the bandwidth capabilities of the DPA, like the transformation ratios within the combiner, the wideband load match and the control of higher harmonic components present in the drain current of the active devices. The individual sources of bandwidth limitations in the DPA and the relevant approaches available in the literature will be addressed in the framework of chapter two.

1.3.2 Outphasing architectures

Outphasing transmitters constitute another group of active load modulation RFPA architectures. The idea behind the outphasing transmitter is to reproduce the amplitude modulation of a modulated signal by performing a **vectorial addition of two phase shifted carrier signals** at the load. The outphasing angle Θ between the two carrier signals determines the signal amplitude generated at the load. In this way, constant carrier voltage

[6] The term 'digital Doherty' is often used synonymously for the dual-input DPA concept, referring to the digital nature of its drive function generation. However, this term is ambiguous, because it also refers (more legitimately) to a type of DPA that uses switched mode amplifier cores and discrete amplitude steps, like the one described in [29]. The term 'digital Doherty' is therefore not used in this work.

levels can be maintained at the amplifier cores, independent of the output power level, which, in turn, should allow for a very efficient RFPA operation. When the carrier signals are in phase, they add entirely at the load, no energy is reflected and the amplifier cores are perfectly matched, but as soon as outphasing is applied (i.e. $\varphi > 0$), load modulation takes place at the common node of the combiner [7]. Unfortunately, the type of load modulation found in outphasing PAs does not produce strictly resistive load conditions, as is the case in the ideal, tuned Doherty PA, but strongly reactive loads, which will significantly reduce the efficiency of the amplifier cores in backoff. In his original paper from 1933 [30], Henri **Chireix**, who faced essentially the same problem as W. H. Doherty three years later, proposed an outphasing architecture that includes reactive elements $+jX$ and $-jX$ in order to cancel out the reactance created due to the outphasing operation at a certain backoff power level, as depicted in Figure 1.9. This results in a backoff efficiency characteristic similar to that of the Doherty PA, showing a distinct second efficiency peak at backoff [31]. In practical transmitter designs for cellular base station applications, however, it is very difficult to exploit the theoretical potential of the Chireix concept, because the actual RFPA cores do not behave like ideal voltage sources. The input drive levels of the RFPA cores must be adjusted along with the outphasing angle in order to approximate the desired behaviour [32] and to avoid a loss of power added efficiency due to the finite gain of the RFPA cores[7]. Furthermore, the conver-

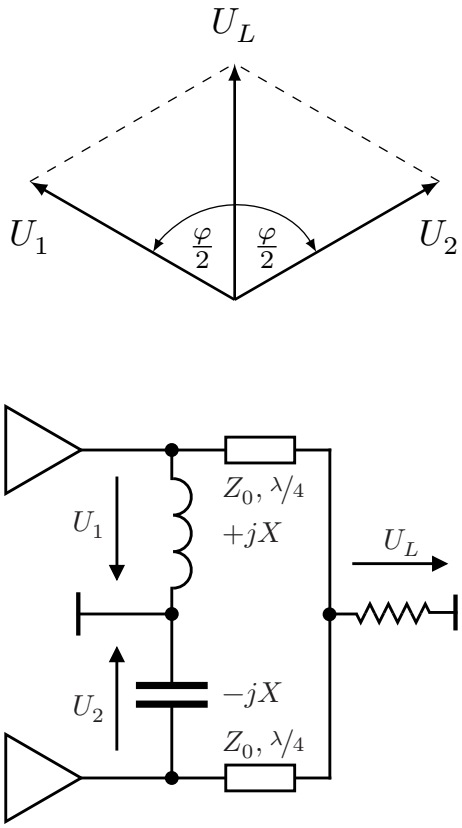

Figure 1.9: Chireix architecture

[7] If a constant input power level was used, the power added efficiency $PAE = \frac{P_{out} - P_{in}}{P_{DC}}$ would drop to zero as the output power backoff due to outphasing approaches the gain of the RFPA cores...

sion of the original signal's amplitude information to a phase modulation of the outphasing signals implicates a significant bandwidth expansion, similar to the polar transmitter concepts discussed before, which limits the suitability of the concept for concurrent wideband/multi-band applications.

As a solution to the problems associated with reactive loads and to extend the efficient output power range of the outphasing transmitter system, Perreault proposed a 4-way outphasing architecture [33] which reduces the reactive components created by the outphasing operation to negligible levels, for the price of increased system complexity. The problems associated with outphasing load modulation can also be avoided entirely by the use of an isolating combiner. The energy that is reflected back from the load due to outphasing is then dissipated in an isolation resistor, such that the amplifier cores see constant load conditions. Such techniques are known under the term **LINC** ('linear amplification with non-linear components') [34]. The LINC technique does indeed enable the use of highly efficient, non-linear, switched mode RFPA's in linear transmitter applications, but the backoff efficiency characteristic of such a system is as bad as that of the Class-A amplifier[8]. In an attempt to improve the backoff efficiency of the LINC transmitter, techniques to reuse the energy that appears at the isolating port of the output combiner instead of just dissipating it in a resistor have been conceptualized [35], but never reached a competitive advantage over other transmitter concepts.

In a nutshell, the outphasing concept, if successfully implemented, might show an efficiency potential that is similar to the Doherty architecture's, but it involves a significantly higher degree of inherent system non-linearity. Thus, in the author's opinion, the Doherty architecture provides a better basis for the design of a wideband active load modulation RFPA. The outphasing principle is nevertheless very important to the understanding of this work, because a continuum of Doherty modes and outphasing modes in frequency domain exists, as was first described by Richard Hellberg in [36]. In the present work, it will be shown that the detuned Doherty PA exhibits a transition from the linear Doherty mode to a non-linear 'quasi-outphasing' mode in amplitude domain and that this has a significant effect on the drive function of the wideband Doherty PA.

[8] i.e. efficiency falls with the square of the amplitude.

2 A generalized Theory on wideband active load modulation

2.1 Doherty PA model

2.1.1 Chain parameter model

A Doherty PA model based on two-port chain parameters is defined. The main and peak amplifier cores are represented by ideal, multi-harmonic current sources, which will be described in detail in section 2.1.2. Under the assumption that the combiner itself is lossless (i.e. the load Z_0 connected to it is the only lossy element), a simple two-port model can be used to describe the Doherty PA circuit.

$$\begin{pmatrix} U_M \\ I_M \end{pmatrix} = \begin{bmatrix} A_{11} & A_{12} \\ A_{21} & A_{22} \end{bmatrix} \begin{pmatrix} U_P \\ -I_P \end{pmatrix} \tag{2.1}$$

In the following sections, a combiner model will be used that is composed of three $\lambda/4$ transmission lines of certain impedances Z_1, Z_2, Z_3 and an ideal matching network, which transforms the load resistance Z_0 to a complex impedance Z_L, as illustrated in Figure 2.1. The chain parameter description of the circuit used here follows as

$$\begin{aligned} \begin{pmatrix} U_M \\ I_M \end{pmatrix} = \begin{bmatrix} \cos(\Theta) & jZ_1\sin(\Theta) \\ \dfrac{j\sin(\Theta)}{Z_1} & \cos(\Theta) \end{bmatrix} \cdot \begin{bmatrix} 1 & 0 \\ \dfrac{1}{Z_L} & 1 \end{bmatrix} \cdot \begin{bmatrix} \cos(\Theta) & jZ_2\sin(\Theta) \\ \dfrac{j\sin(\Theta)}{Z_2} & \cos(\Theta) \end{bmatrix} \\ \cdot \begin{bmatrix} \cos(\Theta) & jZ_3\sin(\Theta) \\ \dfrac{j\sin(\Theta)}{Z_3} & \cos(\Theta) \end{bmatrix} \cdot \begin{pmatrix} U_P \\ -I_P \end{pmatrix} \end{aligned} \tag{2.2}$$

with $\Theta = \dfrac{\pi}{2}\dfrac{f}{f_0}$.

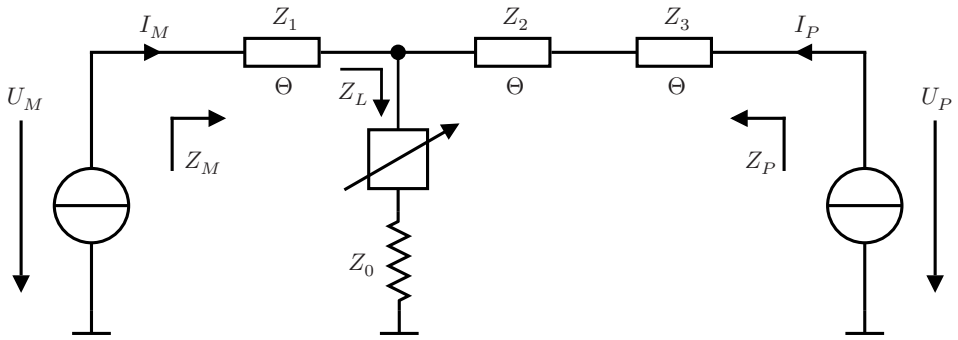

Figure 2.1: Doherty model schematic

This is without loss of generality, since every other linear combiner topology (e.g. the classic Doherty combiner without peaking path offset or a combiner model that includes the transistors drain-source capacitance and other parasitic elements, etc.) could be used as well.

2.1.2 *Multi-harmonic current sources*

The most basic model of a field effect transistor in an RF power amplifier is a voltage controlled current source with a linear transfer characteristic, controlled by a sinusoidal excitation. A variable conduction angle represents the bias setting (i.e. operating mode) of the transistor. Thus, for the reduced conduction angle modes, the drain current waveform has the shape of a cut-off cosine pulse with a certain conduction angle.

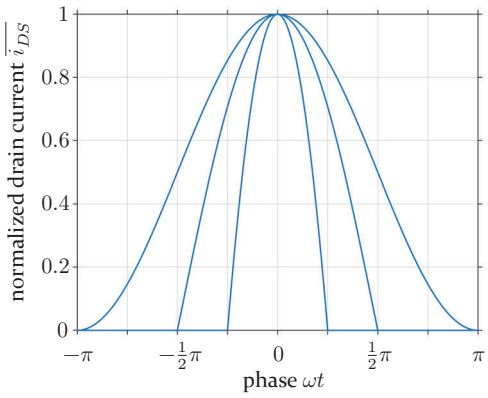

Figure 2.2: Normalized drain current pulse for different conduction angles (2π: Class-A, π: Class-B, $\pi/2$: Class-C)

As the further analysis of wideband active load modulation is performed in frequency domain, the main and peak source currents $\overrightarrow{i_M}$ and $\overrightarrow{i_P}$ will be regarded as har-

monic vectors, which represent the Fourier coefficients of the normalized drain current pulse multiplied by a phasor $\overrightarrow{I_{DS}}$

$$\overrightarrow{i_{DS}} = \overrightarrow{I_{DS}} \left(a_0, a_1, a_2, a_3, \ldots\right)^T \tag{2.3}$$

The Fourier series of the normalized drain current pulse as a function of conduction angle is given as

$$a_k(\phi) = \frac{1}{\pi\left(1-\cos\left(\frac{\phi}{2}\right)\right)} \int_{-\frac{\phi}{2}}^{\frac{\phi}{2}} \left(\cos(t) - \cos\left(\frac{\phi}{2}\right)\right) \cos(kt)\, \mathrm{d}t \tag{2.4}$$

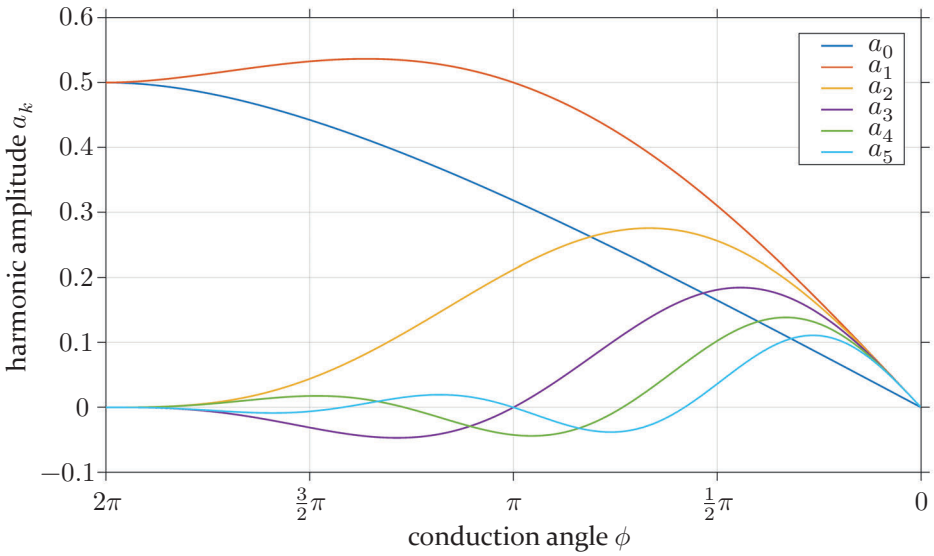

Figure 2.3: Harmonic amplitudes as a function of conduction angle

It is observed that the reduced conduction angle modes are inherently non-linear (see also [E2]), with the exception of $\phi = \pi$ (Class-B) and, trivially, $\phi = 2\pi$ (Class-A). From the envelope domain perspective, this corresponds to the statement that, for the non-linear reduced conduction angle modes, the effective conduction angle is a function of the input amplitude

$$\phi\left(\overline{in}\right) = 2\arccos\left(\frac{\cos\left(\frac{\phi_0}{2}\right)}{\overline{in}}\right) \tag{2.5}$$

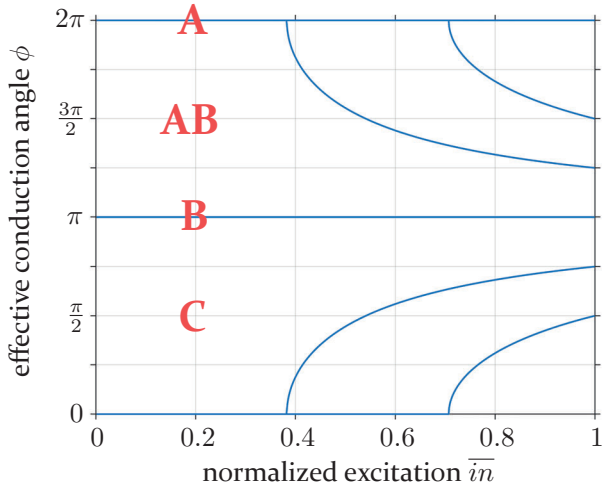

Figure 2.4: Effective conduction angle as a function of the normalized excitation

With respect to further analytical treatment of the problem, a linear, reduced conduction angle mode operation of the transistors is assumed, i.e. a conduction angle of $\phi = \pi$ (Class-B) for both amplifier cores. This is a classic assumption for the treatment of Doherty PAs and it applies to the Class-J theory of termination impedance continua for wideband linear power amplifiers, which will be discussed later in this work, as well. With the conduction angle being set to $\phi = \pi$, the source current vector[1] follows as

$$\overrightarrow{i_{DS}} = \overrightarrow{I_{DS}} \left(\tfrac{1}{\pi}, \tfrac{1}{2}, \tfrac{2}{3\pi}, 0, \tfrac{-2}{15\pi}, 0\right)^T \tag{2.6}$$

2.1.3 Load modulation factor and virtual impedances

Active load modulation, as it results from the Doherty model in section 2.1.1, is assumed to take place only at the fundamental frequency. Higher harmonics are assumed to be terminated individually, without any interaction between the two amplifier cores.[2] Thus, the following derivation of virtual impedances under active load modulation will be applied exclusively to the fundamental

[1] Truncated at 5th harmonic.

[2] In principle, the analysis could be extended to load modulation at higher harmonics, but this is regarded irrelevant from a technical point of view. Practical combiner network synthesis does not provide the degrees of freedom required for a deliberate control of multiharmonic load modulation. A more realistic approach is to minimize transmission of higher harmonics between the amplifier cores, thus avoiding load modulation effects at these frequencies.

frequency component. A linear set of equations for the voltages U_M and U_P occurring across the current sources is easily derived from Eq. 2.1

$$U_M = A_{11}U_P - A_{12}I_P \tag{2.7}$$

$$I_M = A_{21}U_P - A_{22}I_P \tag{2.8}$$

$$\Longrightarrow \qquad U_M = A_{11}\frac{I_M + A_{22}I_P}{A_{21}} - A_{12}I_P \tag{2.9}$$

$$\Longrightarrow \qquad U_P = \frac{I_M + A_{22}I_P}{A_{21}} \tag{2.10}$$

At this point, a **load modulation factor** is introduced, defined as

$$\Gamma = \frac{I_P}{I_M} \tag{2.11}$$

This factor is crucial to the further analysis. The virtual impedance at the main amplifier core follows as

$$Z_M = \frac{U_M}{I_M} = \frac{A_{11}}{A_{21}}(1 + A_{22}\Gamma) - A_{12}\Gamma = \frac{A_{11}}{A_{21}} + \left(\frac{A_{11}A_{22} - A_{12}A_{21}}{A_{21}}\right)\Gamma \tag{2.12}$$

With $\det(A) = 1$ (reciprocity), this simplifies to

$$Z_M = \frac{A_{11} + \Gamma}{A_{21}} \tag{2.13}$$

Likewise, the virtual impedance at the peak amplifier core follows as

$$Z_P = \frac{A_{22} + \frac{1}{\Gamma}}{A_{21}} \tag{2.14}$$

We observe that the virtual impedances solely depend on the load modulation factor Γ. In the following subsection, it will be shown that the knowledge of these virtual impedances is sufficient in order to derive the output parameters (i.e. output power and efficiency) of the amplifier. Thus, the load modulation problem is reduced from a 4-dimensional problem (two complex drain currents) to a 2-dimensional problem (one complex load modulation factor). This proves to be a key to an intuitive understanding of active load modulation and paves the way for a successful treatment of the wideband active load modulation problem.

2.1.4 Clipping operator

Figure 2.5a shows a normalized excitation of the Doherty model, which uses current waveforms $\overrightarrow{i_{DS}}$ as specified in Eq. 2.6. The main amplifier core phasor is normalized to 1 and accordingly the peak amplifier core phasor equals the load modulation factor Γ. The harmonic vectors for the voltages across the sources are given by

$$\overrightarrow{u_{DS}} = U_{DC} + \overrightarrow{i_{DS}} \cdot \left(0, Z_{f_0}(\Gamma), Z_{2f_0}, Z_{3f_0}, Z_{4f_0}, Z_{5f_0}\right) \tag{2.15}$$

with the virtual termination impedance at the fundamental frequency, $Z_{f_0}(\Gamma)$, following from Eqs. 2.13 and 2.14, and fixed termination conditions at the higher harmonics. Without loss of generality, termination conditions within the ideal Class-J continuum were chosen for the example in Figure 2.5b.

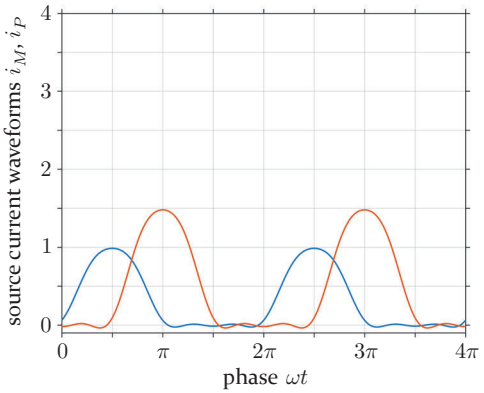

a) Current waveforms at the main (blue) and peak (red) amplifier cores for $\Gamma = j1.5$ [3]

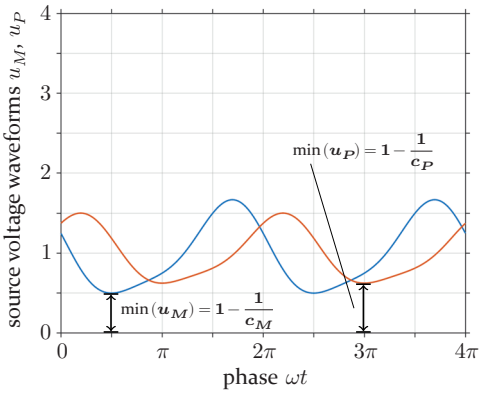

b) Voltage waveforms at the main (blue) and peak (red) amplifier cores for $Z_{M,f_0} = 1 + j\frac{1}{2}$, $Z_{M,2f_0} = -j\frac{3\pi}{16}$, $Z_{P,f_0} = 0.5 + j\frac{1}{4}$ and $Z_{P,2f_0} = -j\frac{3\pi}{32}$. Higher harmonics are assumed to be shorted. [3]

Figure 2.5: Unclipped current and voltage waveforms

Since 'linear' waveforms ($\phi = \pi$) are used, the waveforms can now just be rescaled until one of the voltages across the amplifier cores clips (Figure 2.6). This is strictly in line with the classic principle of active load modulation in power amplifiers, which aims at keeping one (Doherty) or both (Chireix) amplifier cores at voltage saturation in order to improve efficiency throughout

[3] Values in this example are chosen arbitrarily. Note that the DC component of the voltage, which represents the drain bias of the circuit, is normalized to 1.

an extended power region. The scaling factors for this operation are defined as the **clipping factors**

$$c_M = \frac{1}{1-\min\left(u_M(t)\right)} \qquad c_P = \frac{1}{1-\min\left(u_P(t)\right)} \tag{2.16}$$

The lowest of these clipping factors

$$c = \min\left\{c_M, c_P\right\} \tag{2.17}$$

is chosen for the rescaling operation, otherwise one of the voltage waveforms would become negative, which is not allowed.

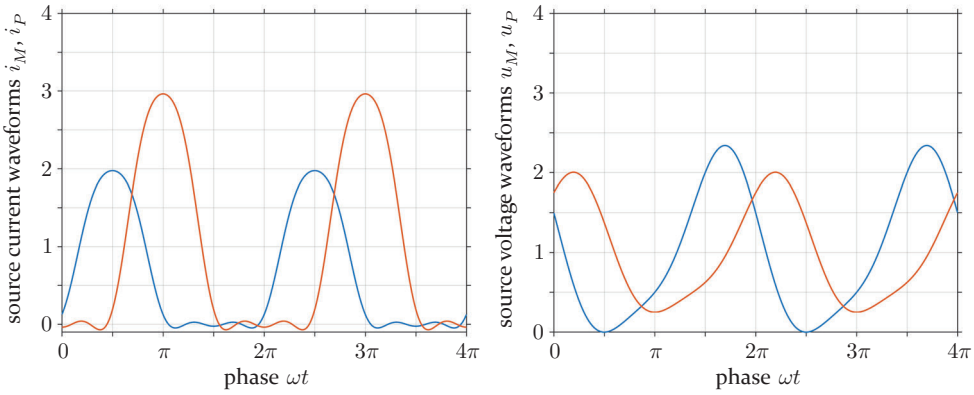

Figure 2.6: Clipped current and voltage waveforms

2.1.5 *Output power and efficiency*

Based on the clipped waveforms, the output parameters of the amplifier can be assessed easily. The output power is the sum of the active powers at the current sources

$$P = \frac{1}{2}\left(\mathfrak{Re}\left\{Z_M |I_M|^2\right\} + \mathfrak{Re}\left\{Z_P |I_P|^2\right\}\right) \tag{2.18}$$

$$= \frac{1}{2} c^2 \left(\mathfrak{Re}\left\{Z_M\right\} + \mathfrak{Re}\left\{Z_P\right\} |\Gamma|^2\right) \tag{2.19}$$

while DC power consumption is given by

$$P_{DC} = U_{DC}\frac{2}{\pi}\left(|I_M| + |I_P|\right) \tag{2.20}$$

$$= \frac{2c}{\pi}\left(1 + |\Gamma|\right) \tag{2.21}$$

The efficiency is

$$\eta = \frac{P}{P_{DC}} \tag{2.22}$$

The demonstrated approach enables a valid and meaningful assessment of the amplifiers output power and efficiency as sole functions of the complex load modulation factor (corresponding to the input drive function in a real amplifier). It allows us to easily visualize the amplifiers output parameters on a two-dimensional, complex load modulation factor plane.

Example 1: Classic, symmetrical Doherty PA

Figures 2.8a and 2.8b illustrate this approach for the case of a classic DPA at center frequency [4], [23]. As expected, we see an efficiency peak at backoff ($\Gamma = 0,\ P = 0.25$) as well as one at full state ($\Gamma = -j,\ P = 1$)[5]. The real advantage of this representation, however, becomes clear when looking at the case of a detuned combiner (Figs. 2.8c, 2.8d). It allows us to intuitively understand the frequency dependence of the DPA's behaviour in connection with the choice of the load modulation factor.

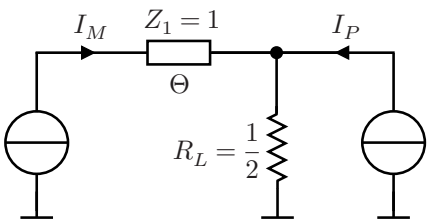

Figure 2.7: Classic, symmetrical DPA[4]

[4] Higher harmonics are assumed to be shorted.

[5] It is interesting to note that a circle of constant power extends beyond the usual full state point in the tuned case. Within this circle, only the power ratio between main and peak path changes, but the output power remains constant (see also footnote 12).

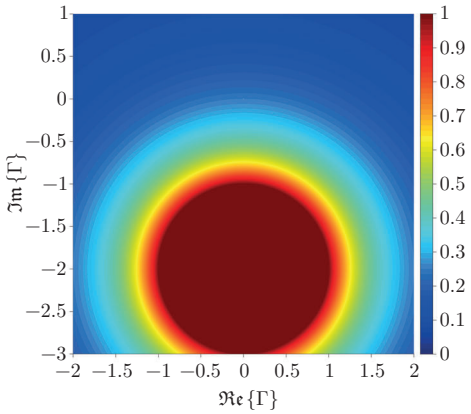

a) Normalized output power P at center frequency

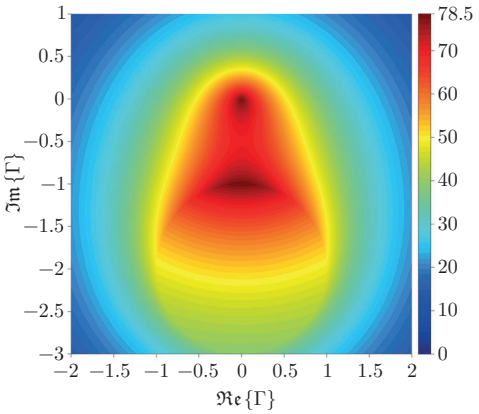

b) Efficiency η [%] at center frequency

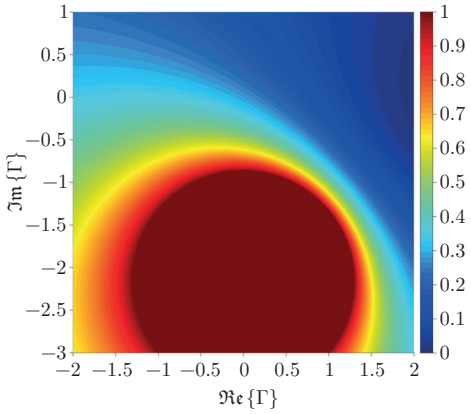

c) Normalized output power P at band edge

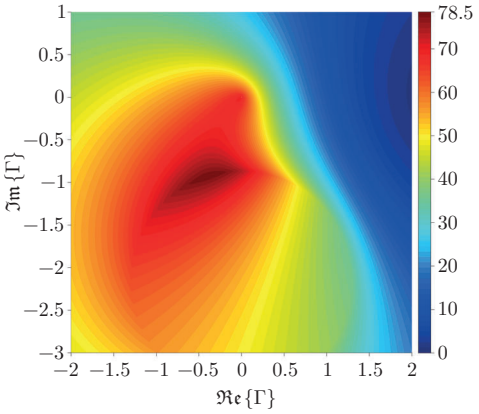

d) Efficiency η [%] at band edge

Figure 2.8: Output parameters of the classic Doherty PA in load modulation space at center frequency and at band edge for a relative BW of 50%

Figure 2.8 also shows that efficiency at the backoff point ($\Gamma = 0$) decreases when the combiner is detuned. Moreover, the output power at the backoff point increases, effectively reducing backoff performance even further (see Fig. 2.9). At full state, the transformation due to the impedance inverter vanishes, because it is matched on both sides. It causes only a phase shift, which is easily compensated by placing a $\lambda/4$ delay line at the input of the peak amplifier ($\Gamma(f) = e^{-j\frac{\pi}{2}\frac{f}{f_0}}$), as is commonly done in classic DPAs. Thus, full state performance is perfectly wideband.

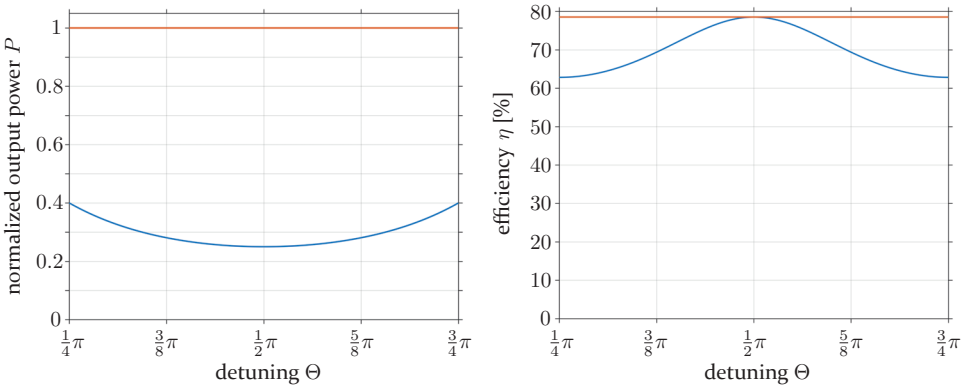

Figure 2.9: Output parameters of the classic DPA vs. detuning $\Theta = \frac{\pi}{2}\frac{f}{f_0}$ at backoff (blue) and full state (red)

Aside from its inherently limited bandwidth at backoff, building a classic DPA at microwave frequencies is practically impossible, since the intrinsic current generator plane of the peak amplifier cannot be connected to the common node without introducing significant offset length. It is therefore common practice to add a 180° offset in the peak path and call it an 'inverted' Doherty amplifier, which leads us to the second example.

Example 2: Grebennikovs solution

Grebennikov proposed a Doherty combiner based on three $\lambda/4$ transmission line sections as depicted in Figure 2.10 [37], [38]. With this solution, the backoff impedance transformation ratio imposed by Z_1 is reduced to 2 (vs. 4 in the classic DPA), which reduces the frequency dependence of the main amplifier core's backoff termination $Z_M(BO)$ significantly. The reduced transformation

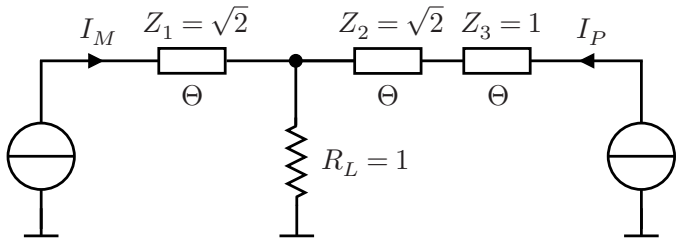

Figure 2.10: Grebennikovs solution[4]

ratio in conjunction with the susceptance imposed by Z_2 and Z_3 in parallel to the load results in a very low imaginary part of $Z_M(BO)$ over a bandwidth of nearly one octave. Consequently, backoff efficiency in this bandwidth is close to its optimum (s. Fig. 2.12). Output power at backoff, however, is not constant, but this may be acceptable to some extend. Since the backoff point is shifted towards lower powers at the band edges, average efficiency is not necessarily compromised.

The drawback in reducing the backoff transformation ratio of the impedance inverter is that it impacts full state performance, as there is also a transformation ratio of 2 at full state now (vs. 1 in the classic DPA). In terms of average efficiency, this is usually not critical, since backoff efficiency is more important than full state efficiency. But if full state power drops, it obviously becomes a problem. At full state, the structure of the load modulation space at the band edges (s. Fig. 2.11c) differs significantly from the classic DPA case. Operating the Grebennikov DPA with a classic input drive function ($\Gamma(f) = e^{j\frac{\pi}{2}\frac{f}{f_0}}$) will induce severe bandwidth limitations at full state (s. Fig. 2.12). On the other hand, when looking at Fig. 2.11c, we observe that the desired full state output power is still available in load modulation space, but it requires an appropriate choice of the load modulation factor Γ. Since Γ is directly linked to the source currents and thus to the input drive functions of the amplifier ($I_M = c(\Gamma)$, $I_P = \Gamma\, c(\Gamma)$), it constitutes a degree of freedom in the design of the DPA. This fact has often been neglected in previous works. Using a non-linear numeric solver to find the points of maximum efficiency for the full state power target $P = 1$ produces a frequency dependent drive function ($\Gamma(f)$) as shown in 2.13. For the case of the Grebennikov DPA, choosing the optimum drive function allows us to maintain full state output power $P = 1$ over a very large bandwidth while at the same time keeping full state efficiency at very good values (s. Fig. 2.12).

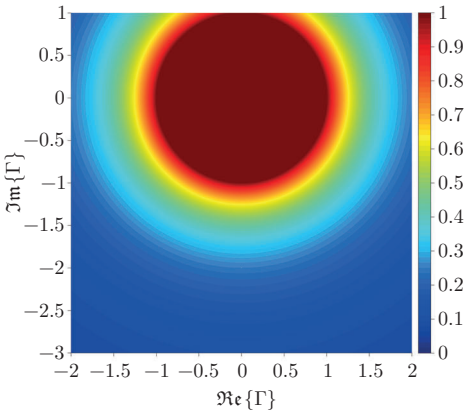

a) Normalized output power P at center frequency

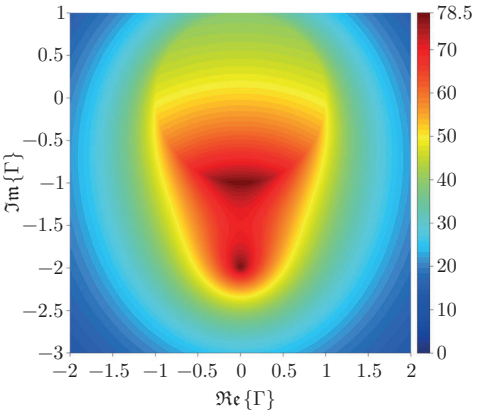

b) Efficiency η [%] at center frequency

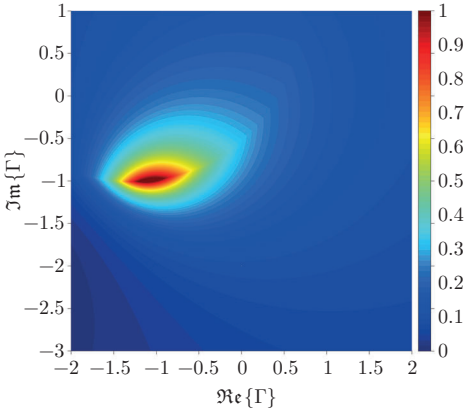

c) Normalized output power P at band edge

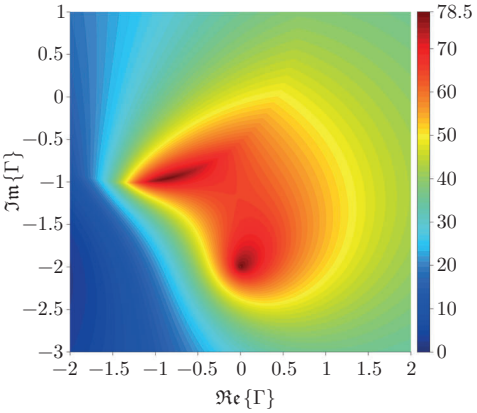

d) Efficiency η [%] at band edge

Figure 2.11: Output parameters of the Grebennikov DPA in load modulation space at center frequency and at band edge for a relative BW of 50%

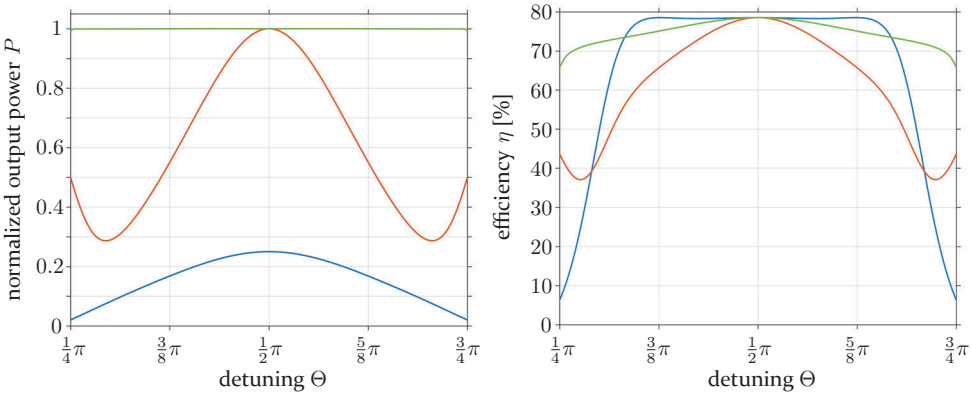

Figure 2.12: Output parameters of the Grebennikov DPA vs. detuning $\Theta = \frac{\pi}{2}\frac{f}{f_0}$ at backoff (blue), full state with classic drive function (red) and full state with optimum drive function (green)

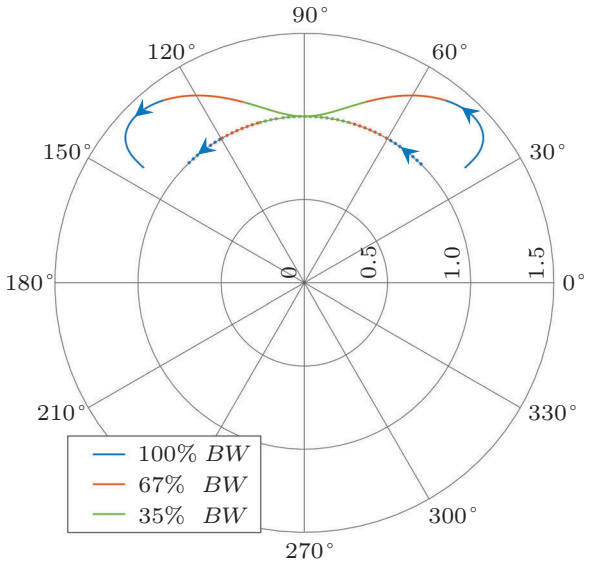

Figure 2.13: Optimum (solid) and classic (dotted) drive function $\Gamma(f)$ for the Grebennikov DPA

These examples hopefully helped to outline some basic principles of wideband DPAs:

- Backoff performance is determined by the frequency response of the combiner network.
- A $\lambda/2$ offset in the peak amplifier path is necessary in order to be able to absorb the transistors parasitics. If this offset is split into two $\lambda/4$ sections, an impedance transformation is introduced into the peak path, allowing us to lower the transformation ratio in the main path[6]. This type of combiner offers two degrees of freedom (vs. zero in the classic DPA) that can be used for bandwidth optimization.
- Full state performance critically depends on the correct choice of the complex load modulation factor.
- Choosing the appropriate load modulation factor for a certain output power is another degree of freedom that the DPA designer has. If a dual input architecture is used, a wide range of drive functions can be generated in digital baseband. In theory, the classic, analogue delay line in conjunction with an analogue power splitter works only for the classic DPA.
- The structure of the load modulation space itself holds some interesting features. When it comes to the analysis of linearity, it turns out that it might not be sufficient to only look at the backoff point and the full state point, as most DPA designers do. It will be shown later that the assumption that some kind of linear transition between these two points exists is usually wrong.

A deeper analysis of the structure and features of the load modulation space will reveal further insights that are extremely valuable to the design of wideband active load modulation PAs. But first things first. Before proceeding with the analysis of the load modulation space in section 2.3, a closer look at the normalization that is used throughout the analysis and at the choice of the wideband load impedance connected to the common node of the Doherty combiner is necessary.

[6] While maintaining symmetric drain bias voltage.

2.1.6 Normalization

The author felt the need to include a subsection about the normalization that is used throughout the analysis, since the details of this normalization are not always self-evident. Multiple more or less meaningful ways of normalization are thinkable and also literature is not consistent in this regard. The author found the normalization shown here to be the most advantageous. Furthermore, this subsection will help to clarify some important relations in the Doherty PA, which will be summarized at the end of the subsection.

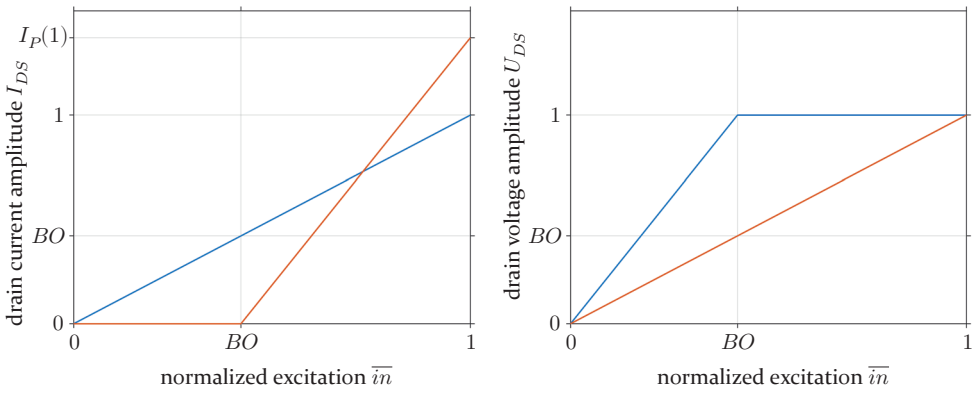

Figure 2.14: Normalized current and voltage amplitudes at the main (blue) and peak (red) amplifier core, respectively, vs. normalized excitation $\overline{in}$

The typical current and voltage functions that define the Doherty PA's operation are shown in Fig. 2.14. The following assumptions and normalizations are made

1. The definitions made in this subsection refer to the **tuned circuit**. Thus, the load impedance as well as the transformations imposed by the $\lambda/4$ transmission lines are strictly real. Higher harmonics are assumed to be shorted at the current generator plane (Class-B operation).

2. The **amplitudes refer to the fundamental frequency component**. The Class-B sine pulse current amplitudes equal twice the fundamental current amplitudes (see Eq. 2.6). The voltage amplitudes equal the fundamental voltage amplitudes, since higher harmonics are assumed to be shorted.

3. A **linear main amplifier drive function** $I_{DS,M}(\overline{in})$ is assumed. In particular, this means that its derivative is constant around the backoff point BO, a condition which will henceforth be referred to as the **1st linearity criterion**.

4. **Drain voltage bias is normalized to $U_{DC} = 1$.** This implies that main and peak amplifier drain voltage bias are assumed to be equal[7] and that the fundamental drain voltage amplitude at saturation is $U_{DS}(1) = 1$.

5. **The full state current amplitude at the main amplifier core is normalized to $I_{DS,M}(1) = 1$.**

Based upon previous definitions, the output powers and termination resistances at the backoff point $\overline{in} = BO$ and at full state $\overline{in} = 1$ follow as

$$P(1) = P_M(1) + P_P(1) = \frac{1}{2}(1 + I_P(1)) \tag{2.23}$$

$$P(BO) = BO^2\, P(1) = \frac{1}{2} BO^2\,(1 + I_P(1)) \tag{2.24}$$

$$R_M(BO) = \frac{1}{2P(BO)} = \frac{1}{BO^2\,(1 + I_P(1))} \tag{2.25}$$

$$R_M(1) = 1 \tag{2.26}$$

$$R_P(1) = \frac{1}{I_P(1)} \tag{2.27}$$

The chain parameters (Eq. 2.1) of the tuned combiner ($\Theta = \frac{\pi}{2}$) reduce to

$$A_{11} = -j\frac{Z_1 Z_2}{Z_3 R_L} \quad A_{12} = -j\frac{Z_1 Z_3}{Z_2} \quad A_{21} = -j\frac{Z_2}{Z_1 Z_3} \quad A_{22} = 0 \tag{2.28}$$

[7] The assumption of a symmetric drain bias has been made for the sake of simplicity, since the basic findings of this work do not rely on a certain choice of a drain bias. This is without loss of generality. The presented analysis can easily be extended to asymmetric drain bias. This will add another degree of freedom to the choice of transformation ratios within the combiner, which can be used to further improve wideband performance. Significant bandwidth improvements due to asymmetric drain bias have been reported in the literature [39], [40].

Inserting them into Eq 2.14 yields

$$R_P(1) = \frac{A_{22} + \dfrac{1}{\Gamma(1)}}{A_{21}} = j\frac{Z_1 Z_3}{\Gamma(1) Z_2} \tag{2.29}$$

With $\Gamma(1) = j I_P(1)$, equating (2.27) and (2.29) leads to the important **relation between the transformation ratios** within the combiner

$$\frac{1}{I_P(1)} = \frac{Z_1 Z_3}{I_P(1) Z_2} \quad \Rightarrow \quad Z_2 = Z_1 Z_3 \tag{2.30}$$

$$R_M(1) = \frac{A_{11} + \Gamma(1)}{A_{21}} = \frac{Z_1^2}{R_L} + j\frac{\Gamma(1) Z_1 Z_3}{Z_2} = \frac{Z_1^2}{R_L} - I_P(1) \tag{2.31}$$

For the backoff state ($\Gamma(BO) = 0$), it follows

$$R_M(BO) = \frac{Z_1^2}{R_L} \tag{2.32}$$

and for the full state ($\Gamma(1) = j I_P(1)$), we get

$$R_M(1) = R_M(BO) - I_P(1) = 1 \;\Rightarrow\; R_M(BO) = 1 + I_P(1) \tag{2.33}$$

Equating this with (2.25), yields

$$I_P(1) = \frac{1}{BO} - 1 \tag{2.34}$$

and

$$R_M(BO) = \frac{1}{BO} \tag{2.35}$$

It is clear that the parameters $I_P(1)$ and $R_M(BO)$ are functions of the backoff ratio BO. This well known fact results directly from the assumption of linearity of the main amplifier drive function around the backoff point (1st linearity criterion)[8]. If this assumption at center frequency is made, there are

[8] A less often contemplated consequence is that if linearity around the backoff point wasn't mandatory (i. e. a piecewise linear main amplifier drive function with different derivatives on each side of the backoff point was feasible), the peak current ratio $I_P(1)$ could theoretically be chosen independently from the backoff point BO.

three degrees of freedom left in the design of the combiner: The backoff ratio BO and the characteristic impedances Z_1 and Z_3. At center frequency, the value of the load resistance R_L is a function of Z_1 and $R_M(BO)$ (s. Eq. 2.32). In the next section it will be shown how the correct choice of the complex load impedance Z_L allows us to maintain a desired backoff termination of the main amplifier core $Z_M(BO)$ even in case of a detuned combiner.

2.2 Quasi left handed loads

2.2.1 *Ideal Class-B load*

The combiner model that was introduced in section 2.1 has four parameters, the characteristic impedances of the transmission lines Z_1, Z_2, Z_3 and the load impedance Z_L. As a result of the normalization presented in the previous section, assuming linear Doherty operation at the center frequency, the relation $Z_2 = Z_1 Z_3$ between the combiner parameters was found. For any given choice of the remaining parameters Z_1 and Z_3, the choice of the load impedance Z_L allows us to realize a desired fundamental termination impedance of the main amplifier core at the backoff state ($\Gamma(BO) = 0$), denoted as $Z_M(BO)$.

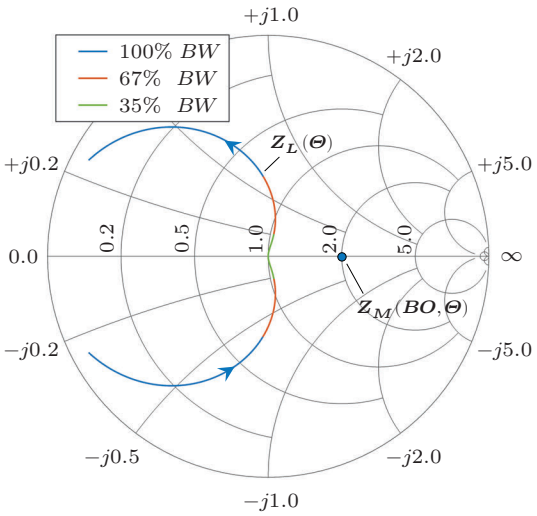

Figure 2.15: Frequency response $Z_L(\Theta)$ of the load impedance connected to the common node required in order to create optimum Class-B backoff termination conditions $Z_M(BO) = 2 + j0$ at the main amplifier core

$Z_M(BO)$ follows from Eq. 2.13 as

$$Z_M(BO) = \frac{A_{11}}{A_{21}} \tag{2.36}$$

The frequency response functions of the chain parameters are easily obtained from the matrix multiplication in Eq. 2.2. Inserting them in Eq. 2.36 and performing some further manipulations yields

$$Z_M(BO,\Theta) = \frac{\begin{array}{l}\cos(\Theta)^2\sin(\Theta)Z_1^2Z_2Z_3-\sin(\Theta)^3Z_1^2Z_2^2-j\cos(\Theta)^3Z_1Z_2Z_3Z_L\\ +j\cos(\Theta)\sin(\Theta)^2(Z_1^2Z_2Z_L+Z_1^2Z_3Z_L+Z_1Z_2^2Z_L)\end{array}}{\begin{array}{l}\cos(\Theta)^2\sin(\Theta)(Z_1Z_2Z_L+Z_1Z_3Z_L+Z_2Z_3Z_L)-\sin(\Theta)^3Z_2^2Z_L\\ +j\cos(\Theta)\sin(\Theta)^2Z_1Z_2^2-j\cos(\Theta)^3Z_1Z_2Z_3\end{array}} \tag{2.37}$$

For an ideal Class-B termination, a certain resistance $R_M(BO)$ is to be maintained over bandwidth, while the respective reactance shall be zero. Setting $Z_M(BO,\Theta) = R_M(BO)$ and solving Eq. 2.37 for Z_L yields

$$Z_L(\Theta) = \frac{\begin{array}{l}Z_1Z_2\big(Z_2\sin(\Theta)^2-Z_3\cos(\Theta)^2\big)(Z_1\sin(\Theta)+jR_M\cos(\Theta))\end{array}}{\begin{array}{l}\cos(\Theta)^2\sin(\Theta)(-R_MZ_1Z_2-R_MZ_1Z_3-R_MZ_2Z_3)+\sin(\Theta)^3R_MZ_2^2\\ +j\cos(\Theta)\sin(\Theta)^2(Z_1^2Z_2+Z_1^2Z_3+Z_1Z_2^2)-j\cos(\Theta)^3Z_1Z_2Z_3\end{array}} \tag{2.38}$$

Looking at Fig. 2.15 we observe that the frequency response of the optimum $Z_L(\Theta)$, which is required for the ideal Class-B termination of the main amplifier core at backoff state, $Z_M(BO,\Theta) = 2 + j0$, shows a counter-clockwise rotation.

2.2.2 Ideal Class-J load

The Class-J termination continuum describes a set of multi-harmonic terminations conditions that enable linear and efficient RFPA operation over an extended bandwidth of theoretically up to one octave. The following derivation of ideal Class-J loading conditions in the Doherty combiner is included at this point in anticipation of the analysis of Class-J operation under active load modulation, which is carried out later in this work. A brief introduction to the Class-J continuum will be given there (see section 2.5.1).

In order to create Class-J termination conditions at the main amplifier core, a reasonable (i.e. physically meaningful) frequency response for the second harmonic termination has to be defined. An obvious solution would be the frequency response of a $\lambda/4$ open stub

$$Z_{M,2f0}(\Theta) = -jZ_{2f0}\cot(\Theta) \quad (2.39)$$

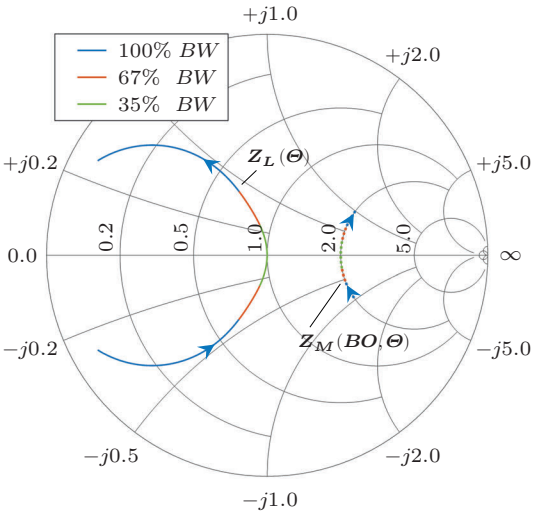

Figure 2.16: Frequency response of Z_L (solid line) for $Z_M(BO) = 2 + j\cot(\Theta)$ (dotted)

The optimum fundamental termination impedance for ideal Class-J conditions at backoff state follows as

$$Z_M(BO,\Theta) = R_M(BO) + jZ_i\cot(\Theta) \quad (2.40)$$

with $R_M(BO)$ denoting the desired fundamental termination resistance at the main amplifier core in backoff state as defined in 2.1.6 and

$$Z_i = \frac{8}{3\pi}Z_{2f0} \quad (2.41)$$

representing the optimum Class-J reactance ratio between fundamental and second harmonic components. Equating eq. 2.40 with eq. 2.37 and solving for the optimum load impedance frequency response $Z_L(\Theta)$ yields

$$Z_L(\Theta) = \frac{-Z_1Z_2\left(Z_2\sin(\Theta)^2 - Z_3\cos(\Theta)^2\right)\left(Z_1\sin^2(\Theta) - Z_i\cos(\Theta)^2 + jR_M\cos(\Theta)\sin(\Theta)\right)}{\begin{aligned}&\cos(\Theta)^2\sin(\Theta)^2(R_MZ_1Z_2 + R_MZ_1Z_3 + R_MZ_2Z_3) - \sin(\Theta)^4R_MZ_2^2\\ &-j\cos(\Theta)\sin(\Theta)^3(Z_1^2Z_2 + Z_1^2Z_3 + Z_1Z_2^2 + Z_2^2Z_i)\\ &+j\cos(\Theta)^3\sin(\Theta)(Z_1Z_2Z_3 + Z_1Z_2Z_i + Z_1Z_3Z_i + Z_2Z_3Z_i)\end{aligned}} \quad (2.42)$$

Again, we observe that the optimum load match frequency response $Z_L(\Theta)$ which is required for $Z_M(BO, \Theta) = 2 + j\cot(\Theta)$ shows a counter-clockwise rotation. An example of an ideal Class-J load impedance frequency response for combiner parameters $Z_1 = \sqrt{2}$ and $Z_3 = 1$ is given in Fig. 2.16.

2.2.3 Practical quasi left handed loads

The previous finding that ideal wideband loads in a Doherty combiner exhibit a counterclockwise frequency dependence is repelling at first glance, as such frequency responses are known to be unnatural. Empirical findings, however, show that the kind of frequency response seen in Figures 2.15 and 2.16 can, to a certain extent, be approximated by a multi-section transmission line transformer composed of $\lambda/4$ sections as depicted in Figure 2.17. The attainable accuracy and bandwidth of this approximation depend on the order of the transformer network. For practical reasons, the number of $\lambda/4$ sections must be limited to a rather low value (3 - 5), otherwise transmission losses and PCB area usage would become prohibiting. Using numerical optimization algorithms, parameters Z_{Tn} can be found that approximate the frequency response of the ideal wideband load $Z_L(\Theta)$ on a certain bandwidth. Figure 2.18 shows examples of such approximations for a Class-B and a Class-J case. At least for some choices of the combiner parameters Z_1 and Z_3, the approximations can be made very tight, resulting in a $Z_M(BO)$ which comes very close to its optimum. Obviously, there are also choices of Z_1 and Z_3 that lead to a $Z_L(\Theta)$ which cannot be approximated that easily. Therefore, this aspect has to be taken into account when choosing the combiner parameters Z_1 and Z_3. Section 2.4.2 will further elaborate on this issue and present some simple measures that allow to estimate the feasibility of approximating a certain $Z_L(\Theta)$. It has been argued in chapter one that single-ended RFPA cores operating in reduced conduction angle modes are generally limited to bandwidths below one octave, since fundamental and second harmonic frequency bands will overlap at higher bandwidths.

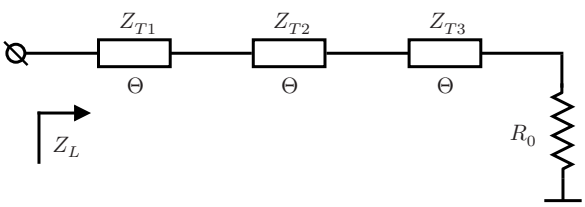

Figure 2.17: Three section output transformer

In addition to that, the following sections, which will take a closer look at the characteristics of the load modulation space, will illustrate that the linear kind of active load modulation that is promoted in this work will also limit the bandwidth to below one octave. Active load modulation can in principle support higher bandwidths by using continuous transitions between different load modulation schemes [36], [41], but this means to sacrifice the Doherty PA's biggest advantage: its inherent linearity.

In summary, there are multiple reasons for an octave limit[9] on the hardware side. Moving beyond that limit will severely impact efficiency and/or linearity and is therefore not desirable in applications like macrocell base station PAs, on which this work is focused. A relative bandwidth of 40 - 50 % would be sufficient in the majority of typical use cases. The goal is to cover neighbouring frequency bands with a single PA and to meet demands for full band operation in wider frequency bands, which are expected in the future. The idea of a single

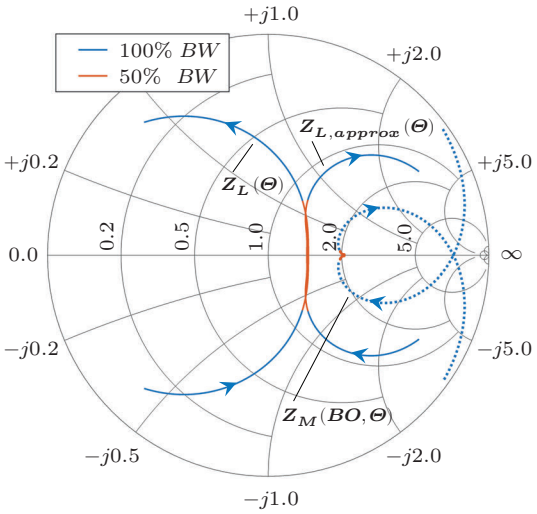

a) Class-B: $Z_1 = 1.7$, $Z_3 = 1$, $Z_i = 0$

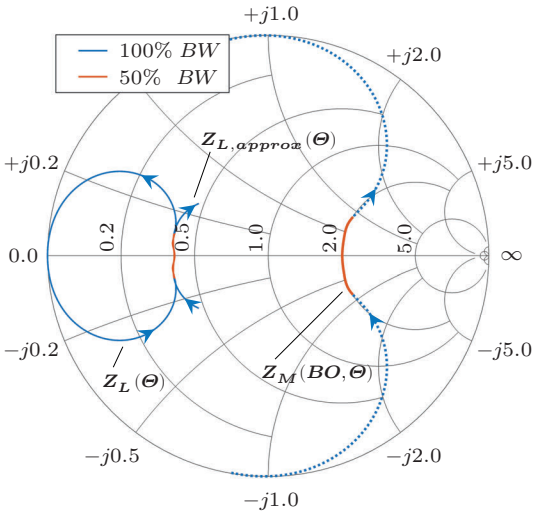

b) Class-J: $Z_1 = 0.9$, $Z_3 = 0.7$, $Z_i = 1$

Figure 2.18: Examples of optimum left handed $Z_L(\Theta)$, their approximation by a 4-step transformer (solid lines) and the resulting $Z_M(BO, \Theta)$ (dotted)

[9] The octave limit is a theoretical upper bound. In practice, a 40 - 50 % rel. BW limit on the hardware side is more realistic, due to restrictions in the synthesis of practical combiner networks.

ultra wideband PA that could possibly cover all cellular bands at once will not become attractive in foreseeable future, since there are too many drawbacks associated with it, even aside from the feasibility and performance of the PA itself. To conclude this section, we will briefly recapitulate the findings regarding the optimum wideband load match $Z_L(\Theta)$:

- For a given set of combiner parameters Z_1 and Z_3, the choice of the load match Z_L allows us to create a desired backoff termination of the main amplifier core $Z_M(BO)$.
- In order to create optimum wideband termination conditions at backoff state, left handed frequency responses of Z_L are required.
- By using multi-step transmission line transformers, many of these responses can be well approximated on a relative bandwidth of 50 %, which is sufficient from an application level perspective.
- **Defining the optimum wideband load match $\boldsymbol{Z_L(\Theta)}$ analytically enables us to implicitly set the backoff performance to its optimum. If the feasibility of the load match approximation is ensured, the wideband combiner design problem is thus reduced to the analysis of performance in the load modulation region.**

2.3 Analysis of the fundamental load modulation space

In section 2.1, coloured surface plots representing the output power and efficiency of two Doherty PA examples in complex load modulation space were shown (Figs. 2.8 and 2.11). These examples already indicated that, by mapping the two complex input vectors of the DPA to a two dimensional space, the load modulation space representation presented in this work enables a very intuitive understanding of the DPA's wideband behaviour and revealed some eye-catching geometric features that demand closer examination. The most important concepts and tools for the analysis of the wideband load modulation space will be introduced in this section. In this context, the fundamental (i.e. Class-B) load modulation space has the major advantage that the clipping factors can be expressed analytically and that nearly all of the important geometric representations come in the form of circular arcs.

The following examples (Figs. 2.19 - 2.21) illustrate the concepts of the load modulation space analysis at center frequency and at frequency deviations corresponding to 25 % and 50 % of relative bandwidth, respectively[10]. Combiner parameters $Z_1 = \sqrt{2}$, $Z_3 = 1$ and an optimum Class-B load match $Z_L(\Theta) = Z_{L,opt}(\Theta)$, as defined by Eq. 2.38 ($R_M = 2$), are used in the examples. Due to the optimum load match, performance at the backoff point ($\Gamma = 0$) is implicitly held at its optimum throughout the bandwidth.

Since the iso-P contours can be calculated analytically, it is no longer necessary to use separate diagrams for output power and efficiency. In the following plots, colour will be used to represent efficiency while the output power will be represented by iso-P contours drawn from 0.25 to 1 in steps of 0.125.

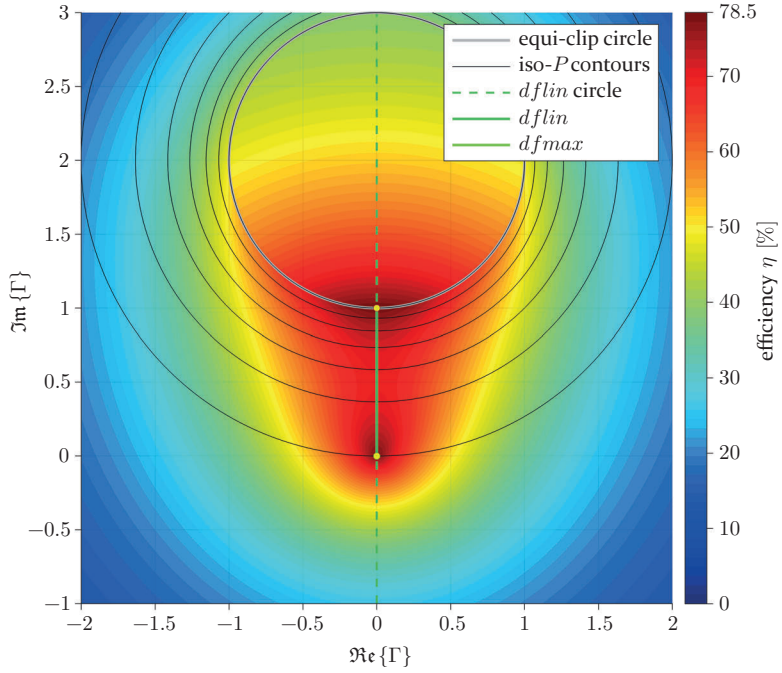

Figure 2.19: Class-B load modulation space at $\frac{f}{f_0} = 1$ (center frequency)

[10] Since the frequency response of the combiner circuit used is symmetric around the center frequency, only the upper band edge is shown. At the lower band edge, the load modulation space is mirrored along the $\mathfrak{Im}\{\Gamma\}$-axis.

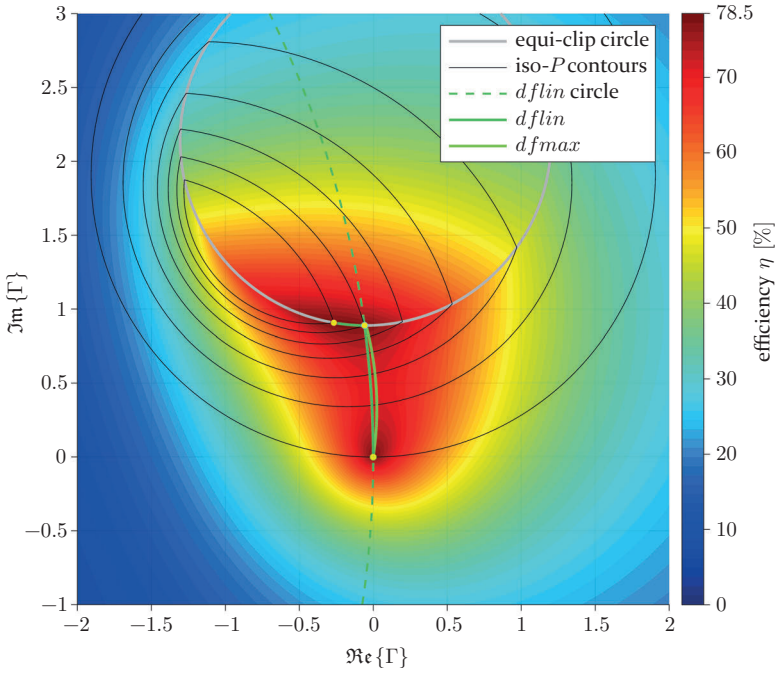

Figure 2.20: Class-B load modulation space at $\frac{f}{f_0} = 1.125$ (detuning to 25% rel. BW)

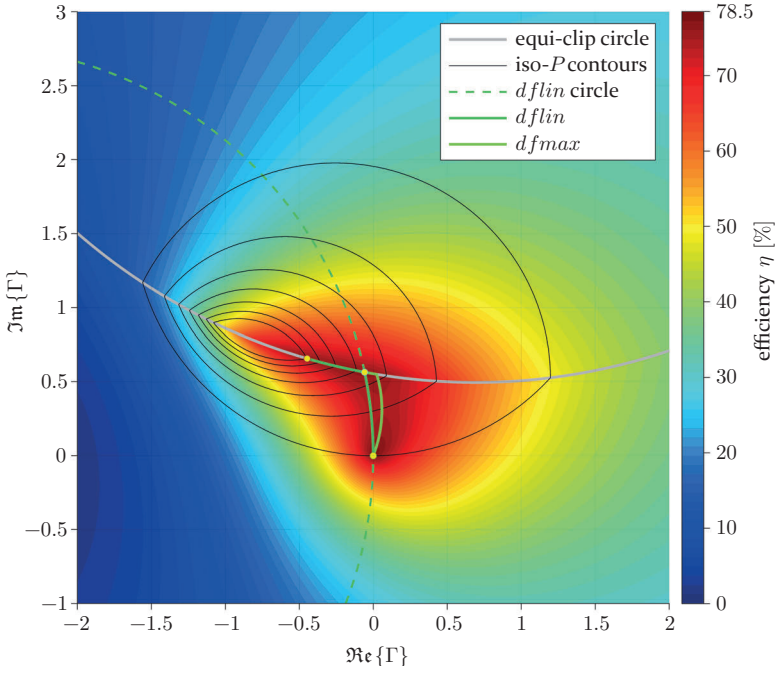

Figure 2.21: Class-B load modulation space at $\frac{f}{f_0} = 1.25$ (detuning to 50% rel. BW)

2.3.1 Equi-clip circle

Under the assumption of a sinusoidal drain voltage (i.e. Class-B), the clipping factors can be expressed analytically as

$$c_M(\Gamma) = \frac{1}{1-\min(u_M(t))} = \frac{1}{|U_M|} = \frac{1}{|Z_M(\Gamma)|} = \left|\frac{A_{21}}{A_{11}+\Gamma}\right| \tag{2.43}$$

$$c_P(\Gamma) = \frac{1}{1-\min(u_P(t))} = \frac{1}{|U_P|} = \frac{1}{|\Gamma\, Z_P(\Gamma)|} = \left|\frac{A_{21}}{A_{22}\Gamma+1}\right| \tag{2.44}$$

Equating these yields

$$c_M(\Gamma) = c_P(\Gamma) \tag{2.45}$$

$$|\Gamma + A_{11}| = |A_{22}\Gamma + 1| \tag{2.46}$$

$$\left|\frac{\Gamma + A_{11}}{\Gamma + \frac{1}{A_{22}}}\right| = |A_{22}| \tag{2.47}$$

Applying the conformal mapping

$$\psi(\Gamma) = \frac{A_{11}A_{22}-1}{A_{22}\Gamma+1} \tag{2.48}$$

to the left side of Eq. 2.47 yields the complex equation of a circle

$$|\psi(\Gamma)+1| = |A_{22}| \tag{2.49}$$

Inserting $\psi(\Gamma) \in \{|A_{22}|-1, -|A_{22}|-1\}$ yields

$$\Gamma_1 = \frac{A_{11}A_{22}-|A_{22}|}{A_{22}(|A_{22}|-1)} = \frac{A_{11}\sqrt{A_{22}}-\sqrt{A_{22}^*}}{A_{22}\sqrt{A_{22}^*}-\sqrt{A_{22}}} \tag{2.50}$$

$$\Gamma_2 = \frac{-A_{11}A_{22}-|A_{22}|}{A_{22}(|A_{22}|+1)} = \frac{-A_{11}\sqrt{A_{22}}-\sqrt{A_{22}^*}}{A_{22}\sqrt{A_{22}^*}+\sqrt{A_{22}}} \tag{2.51}$$

As the conformal mapping preserves the angle, these points can be used in order to calculate the center and radius of the original circle

$$M_{eq} = \frac{\Gamma_1 + \Gamma_2}{2} = \frac{A_{11} - A_{22}^*}{|A_{22}|^2 - 1} \tag{2.52}$$

$$r_{eq} = \frac{|\Gamma_1 - \Gamma_2|}{2} = \frac{|A_{11}A_{22} - 1|}{|A_{22}|^2 - 1} \tag{2.53}$$

The circle

$$r_{eq} = |\Gamma - M_{eq}| \tag{2.54}$$

represents the equi-clip condition (Eq. 2.45) in load modulation space and will henceforth be referred to as the **equi-clip circle**.

2.3.2 *Iso-P circles*

Numerically calculated output power plots like the one shown in Fig. 2.11c already indicated that the iso-P contours seem to be circular arcs, limited by the equi-clip circle. **The equi-clip circle splits the load modulation space in two subspaces, one limited by c_M, the other one limited by c_P.** In accordance to the operating principle of the Doherty amplifier, we usually only operate in the area limited by c_M. However, for the sake of completeness, the iso-P circles will be derived for both subspaces, starting with

the c_P-limited iso-P circles:

$$P = \frac{1}{2} c_P^2 \left(\mathfrak{Re}\{Z_M\} + \mathfrak{Re}\{Z_P\} |\Gamma|^2 \right) \tag{2.55}$$

$$= \frac{|A_{21}|^2}{2|A_{22}\Gamma + 1|^2} \left(\mathfrak{Re}\left\{ \frac{A_{11} + \Gamma}{A_{21}} \right\} + \mathfrak{Re}\left\{ \frac{A_{22} + \frac{1}{\Gamma}}{A_{21}} \right\} |\Gamma|^2 \right) \tag{2.56}$$

$$= \frac{\Gamma\Gamma^*(A_{22}A_{21}^* + A_{22}^*A_{21}) + \Gamma(A_{21} + A_{21}^*) + \Gamma^*(A_{21} + A_{21}^*) + A_{11}A_{21}^* + A_{11}^*A_{21}}{4(\Gamma\Gamma^*A_{22}A_{22}^* + \Gamma A_{22} + \Gamma^*A_{22}^* + 1)} \tag{2.57}$$

which can be rewritten as

$$\Gamma\Gamma^*\left(2P|A_{22}|^2-\mathfrak{Re}\{A_{22}A_{21}^*\}\right)+\Gamma\left(2PA_{22}-\mathfrak{Re}\{A_{21}\}\right)+\Gamma^*\left(2PA_{22}^*-\mathfrak{Re}\{A_{21}\}\right)=\mathfrak{Re}\{A_{11}A_{21}^*\}-2P \quad (2.58)$$

This equation has the form

$$\Gamma\Gamma^*a+\Gamma b+\Gamma^*b^*=c \quad (2.59)$$

With $a,c\in\mathbb{R}$, Eq. 2.59 can be transformed to the equation of a circle

$$\Gamma\Gamma^*+\Gamma\frac{b}{a}+\Gamma^*\frac{b^*}{a^*}=\frac{c}{a} \quad (2.60)$$

$$\left(\Gamma+\frac{b^*}{a}\right)\left(\Gamma^*+\frac{b}{a}\right)=\frac{c}{a}+\frac{|b|^2}{a^2} \quad (2.61)$$

$$\left|\Gamma+\frac{b^*}{a}\right|=\sqrt{\frac{c}{a}+\frac{|b|^2}{a^2}} \quad (2.62)$$

with

$$a=2P|A_{22}|^2-\mathfrak{Re}\{A_{22}A_{21}^*\} \quad (2.63)$$

$$b=2PA_{22}-\mathfrak{Re}\{A_{21}\} \quad (2.64)$$

$$c=\mathfrak{Re}\{A_{11}A_{21}^*\}-2P \quad (2.65)$$

Thus, center and radius of the c_P-limited iso-P circles follow as

$$M_{iPcp}=-\frac{2PA_{22}^*-\mathfrak{Re}\{A_{21}\}}{2P|A_{22}|^2-\mathfrak{Re}\{A_{22}A_{21}^*\}} \quad (2.66)$$

$$r_{iPcp}=\sqrt{\frac{\mathfrak{Re}\{A_{11}A_{21}^*\}-2P}{2P|A_{22}|^2-\mathfrak{Re}\{A_{22}A_{21}^*\}}+\frac{\left|2PA_{22}-\mathfrak{Re}\{A_{21}\}\right|^2}{\left(2P|A_{22}|^2-\mathfrak{Re}\{A_{22}A_{21}^*\}\right)^2}} \quad (2.67)$$

Likewise, we can calculate

the c_M-limited iso-P circles:

$$P = \frac{1}{2} c_M^2 \left(\mathfrak{Re}\{Z_M\} + \mathfrak{Re}\{Z_P\} |\Gamma|^2 \right) \tag{2.68}$$

$$= \frac{|A_{21}|^2}{2\,|A_{11}+\Gamma|^2} \left(\mathfrak{Re}\left\{ \frac{A_{11}+\Gamma}{A_{21}} \right\} + \mathfrak{Re}\left\{ \frac{A_{22}+\frac{1}{\Gamma}}{A_{21}} \right\} |\Gamma|^2 \right) \tag{2.69}$$

$$= \frac{\Gamma\Gamma^* (A_{22}A_{21}^* + A_{22}^* A_{21}) + \Gamma (A_{21} + A_{21}^*) + \Gamma^* (A_{21} + A_{21}^*) + A_{11}A_{21}^* + A_{11}^* A_{21}}{4\,(\Gamma\Gamma^* + \Gamma A_{11}^* + \Gamma^* A_{11} + A_{11}A_{11}^*)} \tag{2.70}$$

which can be rewritten as

$$\begin{aligned} &\Gamma\Gamma^* (2P - \mathfrak{Re}\{A_{22}A_{21}^*\}) + \Gamma (2PA_{11}^* - \mathfrak{Re}\{A_{21}\}) \\ &\qquad + \Gamma^* (2PA_{11} - \mathfrak{Re}\{A_{21}\}) = \mathfrak{Re}\{A_{11}A_{21}^*\} - 2P|A_{11}|^2 \end{aligned} \tag{2.71}$$

This is transformed to the form of Eq. 2.62 with

$$a = 2P - \mathfrak{Re}\{A_{22}A_{21}^*\} \tag{2.72}$$

$$b = 2PA_{11}^* - \mathfrak{Re}\{A_{21}\} \tag{2.73}$$

$$c = \mathfrak{Re}\{A_{11}A_{21}^*\} - 2P|A_{11}|^2 \tag{2.74}$$

Thus, center and radius of the c_M-limited iso-P circles follow as

$$M_{iPcm} = -\frac{2PA_{11} - \mathfrak{Re}\{A_{21}\}}{2P - \mathfrak{Re}\{A_{22}A_{21}^*\}} \tag{2.75}$$

$$r_{iPcm} = \sqrt{\frac{\mathfrak{Re}\{A_{11}A_{21}^*\} - 2P|A_{11}|^2}{2P - \mathfrak{Re}\{A_{22}A_{21}^*\}} + \frac{|2PA_{11} - \mathfrak{Re}\{A_{21}\}|^2}{(2P - \mathfrak{Re}\{A_{22}A_{21}^*\})^2}} \tag{2.76}$$

The boundary angles at which the c_M and c_P circles intersect each other can be calculated using the law of cosines. For the angles on the c_M circles we get

$$\varphi_{iPcm} = \angle\left(M_{iPcp} - M_{iPcm}\right) \pm \arccos\left(\frac{r_{iPcp}^2 - r_{iPcm}^2 - \left|M_{iPcp} - M_{iPcm}\right|^2}{-2r_{iPcm}\left|M_{iPcp} - M_{iPcm}\right|}\right) \tag{2.77}$$

Likewise, the boundary angles on the c_P circles are given as

$$\varphi_{iPcp} = \angle\left(M_{iPcm} - M_{iPcp}\right) \pm \arccos\left(\frac{r_{iPcm}^2 - r_{iPcp}^2 - \left|M_{iPcm} - M_{iPcp}\right|^2}{-2r_{iPcp}\left|M_{iPcm} - M_{iPcp}\right|}\right) \tag{2.78}$$

When plotting the resulting iso-P contours, it can be observed that the intersection points lie exactly on the equi-clip circle (s. Fig. 2.19 - 2.21), verifying the assumption made in the beginning of this subsection.

2.3.3 Linear drive function

For a drive function to be linear with regard to the main amplifier core's current amplitude, the equation

$$\frac{c_M}{\sqrt{P}} = \frac{c_M(BO)}{\sqrt{P(BO)}} \tag{2.79}$$

must hold. It states that the derivative of the main amplifier drive function in the load modulation region must equal its derivative in the low power region, which has been defined before as the 1st linearity criterion. In this case, c_M is fixed for a given value of P

$$c_M = \frac{|A_{21}|}{|A_{11} + \Gamma|} = c_M(BO)\frac{\sqrt{P}}{\sqrt{P(BO)}} \tag{2.80}$$

At this point, we could use

$$|\Gamma + A_{11}| = \frac{|A_{21}|}{c_M} = \frac{|A_{21}|\sqrt{\mathfrak{Re}\left\{\frac{A_{11}}{A_{21}}\right\}}}{\sqrt{2P}} \tag{2.81}$$

to calculate the center and radius of iso-c_M circles

$$M_{icm} = -A_{11} \tag{2.82}$$

$$r_{icm} = \frac{|A_{21}|\sqrt{\mathfrak{Re}\left\{\frac{A_{11}}{A_{21}}\right\}}}{\sqrt{2P}} \tag{2.83}$$

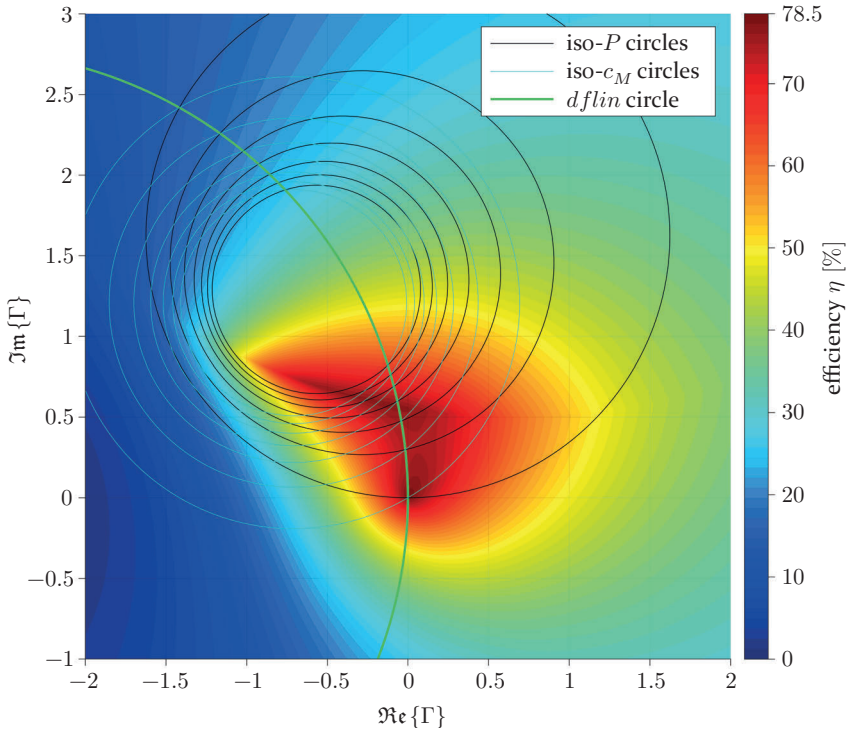

Figure 2.22: $dflin$ circle defined by the intersections of the c_M-limited iso-P circles and iso-c_M circles

A drive function that fulfills the 1st linearity criterion must lay on the intersections of the iso-c_M circles and the corresponding iso-P circles[11]. Calculating the intersection points for certain powers and plotting them in a diagram reveals that the linear drive function itself lies on a circle (s. Fig. 2.22). Instead of calculating individual intersection points, however, it is far easier to derive the linear drive function circle directly by solving Eq. 2.81 for P and equating with Eq. 2.19

$$P = \frac{c_M^2}{c_M(BO)^2} P(BO) = \frac{1}{2} c_M^2 \mathfrak{Re}\left\{\frac{A_{11}}{A_{21}}\right\} = \frac{1}{2} c_M^2 \left(\mathfrak{Re}\{Z_M\} + \mathfrak{Re}\{Z_P\}|\Gamma|^2\right) \tag{2.84}$$

Using the same approach as in 2.3.2 yields

$$2\mathfrak{Re}\left\{\frac{A_{11}}{A_{21}}\right\}|A_{21}|^2 = |\Gamma|^2 \mathfrak{Re}\{A_{22}^* A_{21}\} + \Gamma \mathfrak{Re}\{A_{21}\} + \Gamma^* \mathfrak{Re}\{A_{21}\} \tag{2.85}$$

which gives us center and radius of the linear drive function circle[12]

$$M_{dflin} = -\frac{\mathfrak{Re}\{A_{21}\}}{\mathfrak{Re}\{A_{22}A_{21}^*\}} \tag{2.86}$$

$$r_{dflin} = \left|\frac{\mathfrak{Re}\{A_{21}\}}{\mathfrak{Re}\{A_{22}A_{21}^*\}}\right| \tag{2.87}$$

2.3.4 Maximum efficient drive function

Looking at Figures 2.20 - 2.21 it can be observed that the linear drive function is not the most efficient one. In order to find a drive function with maximum efficiency, P_{DC} has to be minimized for a given output power P. For the c_m limited subspace, P_{DC} is given by

$$P_{DC} = \frac{2}{\pi}\left|\frac{A_{21}}{A_{11}+\Gamma}\right|(1+|\Gamma|) \tag{2.88}$$

[11] Note that this criterion degenerates at center frequency, because iso-c_M and iso-P circles are identical there. Thus, theoretically, every drive function would fulfill the criterion. This is equivalent to the well known statement that, in an ideal, tuned Doherty PA, the peak amplifier core doesn't affect linearity [4]. For the detuned combiner, this statement becomes invalid.

[12] In accordance to footnote 11, these functions have a pole at center frequency ($A_{22} = 0$).

With Γ laying on the respective iso-P circle, the minimum of the function

$$P_{DC}(\varphi) \propto \frac{1+\left|M_{iPcm}+r_{iPcm}e^{j\varphi}\right|}{\left|A_{11}+M_{iPcm}+r_{iPcm}e^{j\varphi}\right|} \tag{2.89}$$

has to be found. This function is not completely differentiable, but its local minimum inside the c_M-limited subspace can easily be found numerically. The most important observation to make here is that the maximum efficient drive function does not follow a circular arc and violates the 1st linearity criterion. Another observation is that usually the linear drive function is only slightly less efficient.

2.3.5 Equi-clip/$dflin$ intersection and 2nd linearity criterion

The examples of Figs. 2.20 - 2.21 illustrated that the maximum output power available in linear Doherty mode in the load modulation space of a detuned combiner (i.e. the power at the intersection of the linear drive function circle and the equi-clip circle) is lower than the targeted full state power. It is further observed that the targeted full state power is still available in the load modulation space, if the drive function leaves the $dflin$ circle at the intersection and follows the equi-clip circle until full state power is reached. This essentially means a transition from the 'linear' Doherty mode[13] to a less linear, 'quasi-outphasing' mode. In order to provide a more intuitive understanding of drive function non-linearity, the drive function can be transformed back from the complex load modulation space to the amplitude domain. In 2.1.5, it has already been shown that the main and peak amplifier drain current amplitudes as well as the relative phase between these currents are easily expressed as functions of the load modulation factor

$$|I_M| = c(\Gamma) \qquad |I_P| = |\Gamma|\, c(\Gamma) \qquad \varphi = \angle\Gamma \tag{2.90}$$

Likewise, the load modulation factor can be referenced back to the normalized linear excitation $\overline{in}$ by using the relationships established in 2.1.5 and 2.1.6.

$$\overline{in} = \sqrt{\frac{P(\Gamma)}{P(1)}} = \sqrt{\frac{P(\Gamma)}{\frac{1}{2}(1+I_P)}} = \sqrt{P(\Gamma)\,2BO} \tag{2.91}$$

[13] Note that the 'linear' Doherty mode defined in 2.3.3 is only linear with regard to the main amplifier cores amplitude function.

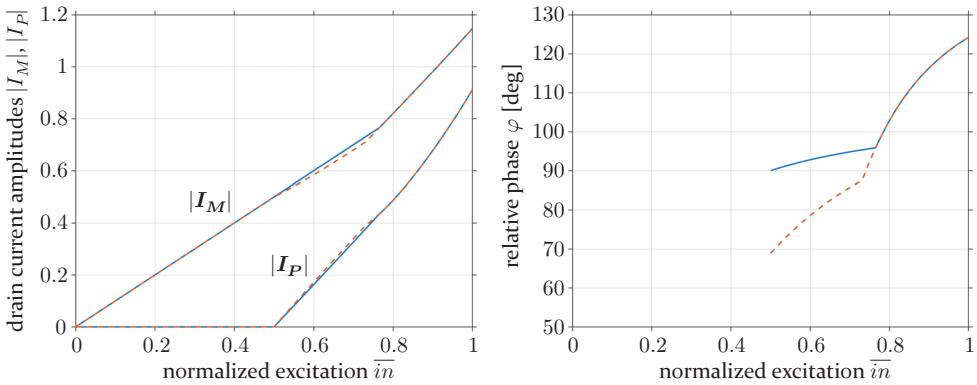

Figure 2.23: 'Linear' (blue) and maximum efficient (red dotted) drive functions vs. normalized excitation $\overline{in}$ corresponding to the load modulation space shown in Fig. 2.21

Figure 2.23 shows that a distinct discontinuity in the derivative of the drive function arises from the transition between the $dflin$ circle and the equi-clip circle. Thus, a **second linearity criterion** can be defined, based on the maximum available power of the linear Doherty mode. The difference between the output power at the $dflin$/equi-clip intersection point $P(int)$ and the targeted full state power $P(1)$, or alternatively the euclidean distance $|\Gamma(int) - \Gamma(1)|$ between the intersection and the full state load modulation factor[14], provide useful measures for the amount of drive function non-linearity that a certain DPA topology exhibits in wideband operation. The intersection point of the $dflin$ circle and the equi-clip circle can be calculated directly using Herons formula

$$\Gamma(int) = \frac{\left(M_{eq} + M_{dflin}\right)\left(M_{eq} - M_{dflin}\right)^* - r_{eq}^2 + r_{dflin}^2 \pm jd}{2\left(M_{eq} - M_{dflin}\right)^*} \tag{2.92}$$

with

$$d = \sqrt{\left(g + r_{ep} + r_{dflin}\right)\left(-g + r_{ep} + r_{dflin}\right)\left(g - r_{ep} + r_{dflin}\right)\left(g + r_{ep} - r_{dflin}\right)} \tag{2.93}$$

$$g = \left|M_{eq} - M_{dflin}\right| \tag{2.94}$$

[14] $\Gamma(1)$ is found by inserting the boundary angle (eq. 2.77) into the equation of the iso-$P(1)$ circle.

The maximum output power of the linear Doherty mode follows from

$$P(int) = \frac{c_M(int)^2}{c_M(BO)^2} P(BO) = c_M(int)^2 \, \mathfrak{Re}\left\{\frac{A_{11}}{A_{21}}\right\} \tag{2.95}$$

$$= \left|\frac{A_{21}}{A_{11} + \Gamma(int)}\right|^2 \mathfrak{Re}\left\{\frac{A_{11}}{A_{21}}\right\} \tag{2.96}$$

It will be shown in the next section that, for the case discussed so far (Class-B, $Z_2 = Z_1 Z_3$), the distance $|\Gamma(int) - \Gamma(1)|$ cannot be brought to zero. But even in case both the first and second linearity criterion could be met (i.e. the main amplifier's amplitude drive function would be perfectly linear), the peak amplifier's amplitude drive function will remain non-linear[15] and a drive function with non-linear phase is necessary in order to facilitate wideband active load modulation as outlined in this work. A certain amount of drive function non-linearity seems to be inevitable in a wideband DPA design, but there are reasons to assume that this is not necessarily a problem. The analysis presented here is based on a highly simplified model of the active devices. In practice, the non-linearity introduced by the active devices themselves will be in the same order of magnitude as the drive function non-linearity introduced by wideband DPA operation. It is common practice today to optimize efficiency by allowing even a classic narrowband DPA to be quite non-linear. Digital predistortion is then applied in order to linearize the system. If the amount of drive function non-linearity that is inherent to wideband DPA operation stays within the range that the DPD can deal with, it can be a feasible solution. It seems reasonable to assume that intelligent signal processing enables us to meet this goal, which will be discussed briefly at the end of this work. The only major difference to state-of-the-art cellular base station transmitter chains is that the wideband DPA concept discussed here implies a dual input PA architecture and, consequently, a dual output DPD.

The concepts of load modulation space analysis introduced in this section will be transferred to the Class-J load modulation space in section 2.5. With the help of these tools, it will be shown that a Class-J termination of

[15] Note that the peak amplifier's amplitude drive function is inherently non-linear due to the sequential nature of the Doherty architecture, which calls for Class-C operation of the peak amplifier core. In practice, this can be more critical than the additional non-linearity theoretically required for wideband operation. In this context, it should also be reconsidered what was said in footnote 11.

the main amplifier core is indeed helpful in order to minimize the measure $|\Gamma(int) - \Gamma(1)|$ and theoretically even allows to fulfill the 2nd linearity criterion. Before moving forward to the Class-J load modulation space, however, the next section will explore the combiner design space spanned by the combiner parameters Z_1 and Z_3.

2.4 Analysis of the Class-B combiner design space

For the combiner structure discussed here, literature offers several approaches towards an optimum choice of parameters Z_1, Z_2 and Z_3 with respect to wideband operation [11], [37]–[44]. None of these works, however, is able to provide a complete picture of the problem. By assuming a resistive load match R_L, constant throughout the bandwidth, they do not recognize the potential of choosing a complex wideband load match that implicitly sets the main amplifiers backoff termination to its optimum value. Thus, besides missing out a substantial step towards improving wideband performance, they all share the problem of affecting both backoff and full state performance simultaneously when modifying combiner parameters. Moreover, they mostly ignore the role of the drive function, which is absolutely crucial to the understanding of wideband active load modulation, as has been demonstrated in the previous section of this work. The analysis of the combiner design space that is proposed here is based on three principles:

- The combiner design space is reduced to the parameters Z_1 and Z_3. The other two combiner parameters, Z_2 and $Z_L(\Theta)$, are functions of Z_1 and Z_3.
- Performance must only be evaluated in the load modulation region. Performance at deep backoff, prior to the onset of load modulation, is implicitly held at its optimum, due to the choice of the optimum wideband load match $Z_L(\Theta)$ at the common node of the combiner.
- Load modulation space analysis establishes a direct relationship between the choice of combiner parameters and the drive function.

This approach allows us to reduce the problem to a manageable amount of performance and feasibility criteria, which can all be expressed as functions of the combiner parameters Z_1 and Z_3. In the following, the combiner design space spanned by Z_1 and Z_3 will be further examined and illustrated. A

two dimensional parameter sweep over the $[Z_1, Z_3]$-space is performed and for each point in the design space, a set of measures is deduced from load modulation space analysis:

- **Boundaries:**
  The choice of Z_1 and Z_3 is restricted by a number of boundary conditions. For the Class-B case examined in this section, but even more so for the Class-J case that will be treated in section 2.6, the study of these boundary conditions will help to improve the understanding of the underlying load modulation space concept, as it provides examples of load modulation spaces that are significantly different from the usual Doherty space.

- **Feasibility of $Z_L(\Theta)$:**
  In section 3.2, wideband load impedance functions $Z_L(\Theta)$ have been derived which ensure an optimum termination of the main amplifier core at backoff state throughout the bandwidth. It was pointed out that the resulting frequency slope of $Z_L(\Theta)$ exhibits a counterclockwise behaviour, which can only be approximated to a certain extend by a multi-section impedance transformer. Thus, the feasibility of this approximation must be taken into account when choosing combiner parameters Z_1 and Z_3.

- **Drive function non-linearity:**
  As outlined in 2.3.5, the euclidean distance between the full state load modulation factor and the $dflin$/equi-clip intersection point $|\Gamma(int) - \Gamma(1)|$, as well as the maximum output power of the linear Doherty mode $P(int)$, are used for the assessment of drive function non-linearity.

- **Efficiency in the load modulation region**

- **Full state balance:**
  Based on the first linearity criterion, it has been shown in 2.1.6 that the full state current ratio $\frac{|I_P|}{|I_M|}$ and the full state power ratio $\frac{P_P}{P_M}$ at center frequency are functions of the backoff parameter BO. For the detuned combiner, however, these ratios will deviate from their center frequency value. This deviation must be kept within reasonable limits, otherwise it will affect the feasibility and performance of the implementation.

These criteria will be addressed in more detail in the following subsections. As in previous sections, the target bandwidth will be 50 % (i.e. $\frac{f}{f_0} = 1.25$) and

the backoff parameter is set to $BO = \frac{1}{2}$. Z_2 is set to $Z_2 = Z_1\, Z_3$ and Z_L is set to the optimum $Z_L(\Theta)$ as derived in section 2.2.

2.4.1 Boundary conditions

For the Class-B case, three boundary conditions are identified. Each condition will be represented by an encircled number which will later be used to identify the respective region in the diagrams visualizing the $[Z_1, Z_3]$ design space.

① The first and most basic boundary condition is obtained by checking if **the maximum available output power in load modulation space reaches the targeted full state power** $P(1) = \frac{1}{2\,BO}$. One way to do this is to check if the c_M- and c_P-limited iso-P circles for $P(1)$ intersect each other (or the equi-clip circle). This is done by using the form of Eq. 2.77 and checking if the argument of the arccos-function lies within the interval $\{-1, 1\}$.

$$\left| \frac{r_{iPcm}^2 - r_{eq}^2 - \left|M_{eq} - M_{iPcm}\right|^2}{2\, r_{eq} \left|M_{eq} - M_{iPcm}\right|} \right| \quad \leq \quad 1 \tag{2.97}$$

② The second boundary condition is given by

$$c_M(BO) \,<\, c_P(BO) \quad \Rightarrow \quad \left|\frac{A_{21}}{A_{11}}\right| \,<\, |A_{21}| \quad \Rightarrow \quad |A_{11}| \,>\, 1 \tag{2.98}$$

Equation 2.98 implies that **the origin of the load modulation space (i.e. the backoff point $\Gamma = 0$) must lie inside the c_M-limited subspace**. If this condition wasn't met, the peak amplifier core, although inactive, would already saturate at backoff and the main amplifier core would not be saturated at the backoff point. Thus, the output power at the backoff point would be lower than the desired c_M-clipped power $P(BO) = \frac{U_{DC}^2}{2R_M} = \frac{BO}{2}$ and backoff efficiency wouldn't reach $\pi/4$. In this case, the linear drive function defined in section 2.3.3 would also become meaningless. This region is obviously not useful in the design of a Doherty PA, as it contradicts its basic principle.

③ A third boundary condition is found by checking if **the *dflin* circle intersects the equi-clip circle**, as was assumed in the definition of the drive function. Similar to the first boundary condition, this is done by evaluating

$$\left| \frac{r_{dflin}^2 - r_{eq}^2 - |M_{eq} - M_{dflin}|^2}{2 r_{eq} |M_{eq} - M_{dflin}|} \right| \leq 1 \qquad (2.99)$$

The boundaries discussed are illustrated in Fig. 2.24, which shows an exemplary choice of $[Z_1, Z_3]$ that violates both condition ② and condition ③. The equi-clip circle lies entirely within the $dflin$ circle and the backoff point is c_P-clipped.

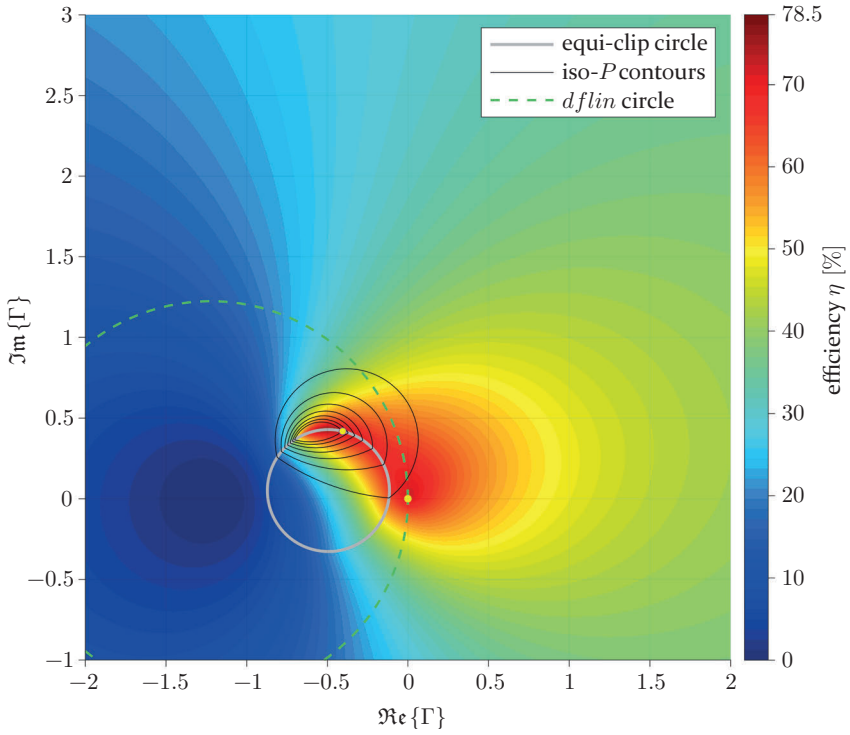

Figure 2.24: Example of load modulation space that violates boundary conditions ② and ③ ($Z_1 = 1.5$, $Z_3 = 0.72$, $BO = 0.5$, $\frac{f}{f_0} = 1.25$, iso-P contours drawn from 0.25 to 1 in steps of 0.125.)

2.4.2 Feasibility of Z_L

Assuming that the output transformer is implemented using microstrip transmission lines, the number of $\lambda/4$ sections is strictly limited, as a high number of sections will result in significant transmission losses and will consume too much PCB area. Three to four sections can be considered a practical limit. A complete analytic treatment of the design and limitations of such transformer networks would go beyond the scope of this work but empirical results have shown that impedance transformers made of three to four $\lambda/4$ sections will approximate the optimum load match frequency response sufficiently well for a quite large range of combiner parameters Z_1 and Z_3, if certain constraints are met. A multidimensional global optimizer, set up to minimize the approximation error between the actual transformer network's frequency response and the ideal $Z_L(\Theta)$, as derived in section 2.2, on a given bandwidth, was applied in order to find the characteristic impedances of the output transformer's $\lambda/4$ sections. Examples of counterclockwise load responses and the corresponding approximations were given in section 2.2.3. Experiments have shown that the maximum quality factor

$$Q_{max} = \max\left(\left|\frac{\mathfrak{Im}\{Z_L(\Theta)\}}{\mathfrak{Re}\{Z_L(\Theta)\}}\right|\right) \tag{2.100}$$

and the maximum resistance variation

$$\Delta R_{max} = \left|\frac{\max(\mathfrak{Re}\{Z_L(\Theta)\})}{\min(\mathfrak{Re}\{Z_L(\Theta)\})}\right| \tag{2.101}$$

over a given bandwidth are useful measures that allow to estimate the feasibility of the approximation. As a rule of thumb, it was found that for $\boldsymbol{Q_{max} < 0.5}$ **and** $\boldsymbol{\Delta R_{max} < 1.2}$, the quasi-left handed load match is feasible. Although not completely accurate, this method allows for a fast identification of the relevant region inside the $[Z_1, Z_3]$ design space, which will be represented by a green line in the diagrams shown in the following subsections.

It must be kept in mind that the results shown in this section refer to a normalized case. This implies that also the reference impedance, which sets the ratio between the drain voltage level and the output power level, is normalized to 1 Ohm. In a practical amplifier design, the actual reference impedance has to be adjusted to the targeted output power level at a given drain voltage level. In general, this will not affect the results presented in this section, since the values of Z_1, Z_2, Z_3 and Z_L can just be rescaled to another

reference impedance, but it might affect the feasibility of the output matching transformer. Since the load impedance connected to it remains at 50 Ohms in a practical RFPA design, the transformation ratio will be changed. Thus, the feasibility of the output transformer has to be re-evaluated when changing the reference impedance, or otherwise an ideal broadband transformation from 50 Ohms to the targeted reference impedance must be provided at the output of the circuit, which might not be practical.

2.4.3 Drive function non-linearity

Figures 2.25 and 2.26 visualize the euclidean distance between the full state load modulation factor and the $dflin$/equi-clip intersection point, as well as the maximum output power of the linear Doherty range $P(int)$ as functions of combiner parameters Z_1 and Z_3. We see that, for the case discussed so far (Class-B, $Z_2 = Z_1\, Z_3$), the minimum of the distance $|\Gamma(int) - \Gamma(1)|$ is around 0.35, thus the second linearity criterion defined in 2.3.5 cannot be met. It has already been argued in 2.3.5 that a certain amount of drive function non-linearity seems to be inevitable in a wideband DPA design. The question of whether or not the extra amount of drive function non-linearity added by the transition from the 'linear' Doherty mode to a 'quasi-outphasing' mode can be absorbed by the digital signal processing available in modern transmitter systems cannot be finally answered in this work, but approaches to resolve the issue on the amplifier side by reducing the distance $|\Gamma(int) - \Gamma(1)|$ will be introduced later. Aside from such approaches on the hardware side, the definition of a maximum efficient drive function introduced in 2.3.4 exemplified that drive function non-linearity and efficiency can always be traded off against each other. Choosing a softer transition between the Doherty mode and the outphasing mode is possible even on the two dimensional load modulation plane. It should be kept in mind that the two dimensional load modulation space representation used in this work was introduced mainly for the purpose of simplifying the analysis. The actual drive function operates on a three dimensional space and is not bound to the condition that at least one amplifier core must be clipped, which opens up yet another degree of freedom to trade off efficiency for drive function linearity. Finally, a dynamic, forward-looking, drive function can be imagined, which changes its path according to the maximum power required in a block of symbols to be transmitted. In this way, we could make use of the low probability of high powers in the signal statistics in order to minimize the degradation of average efficiency caused by the limitations imposed by the drive function non-linearity.

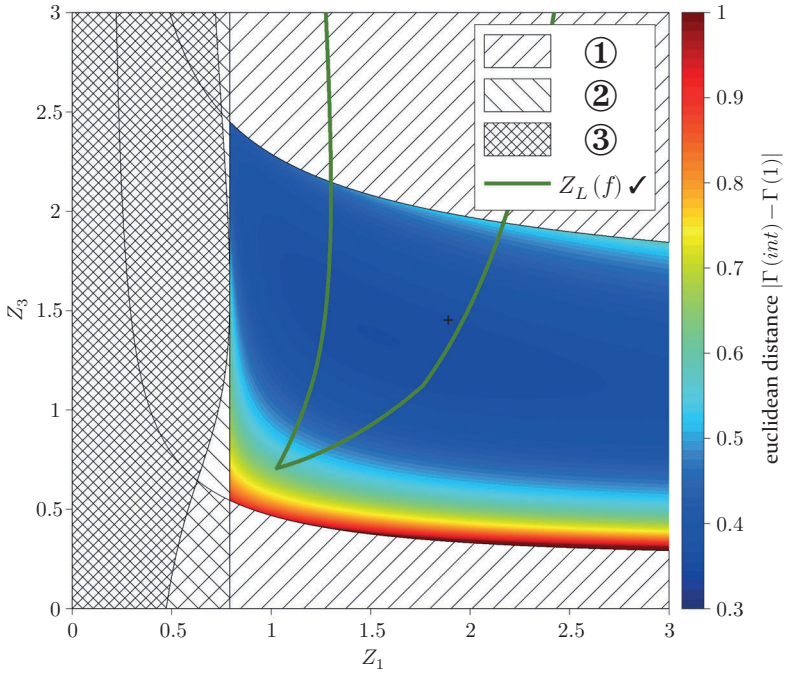

Figure 2.25: Euclidean distance $|\Gamma(int)-\Gamma(1)|$ in $[Z_1, Z_3]$-space

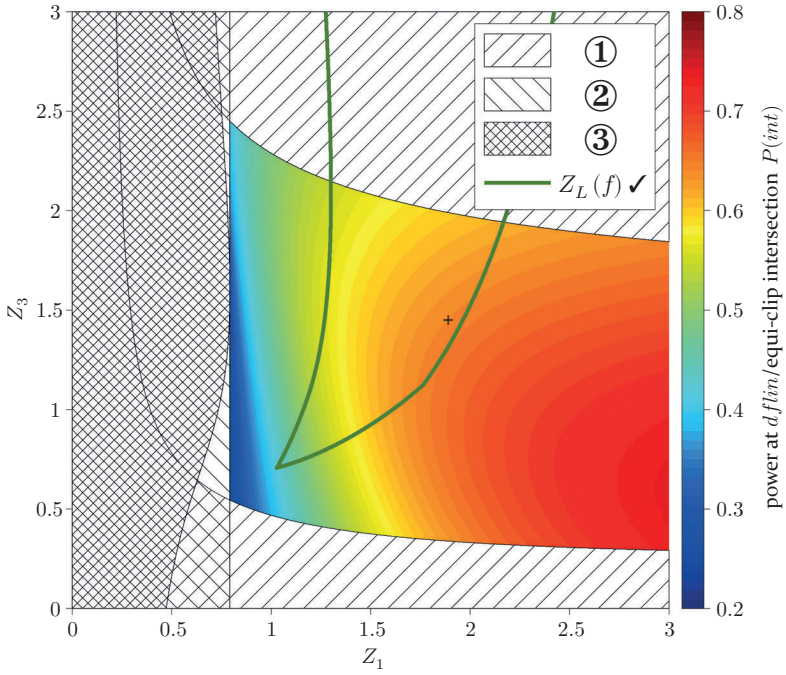

Figure 2.26: Power at $dflin$/equi-clip intersection $P(int)$ in $[Z_1, Z_3]$-space

2.4.4 Efficiency in the load modulation region

Evaluating efficiency at distinct points inside the load modulation region, e.g. at full state (Fig. 2.27) or at the intersection of the linear drive function circle and the equi-clip circle, can be helpful but will not provide the full picture. A more meaningful assessment of efficiency in the load modulation space must be based on some preconditions. Since the average efficiency is an integral measure,

$$\eta_{avg} = \frac{\int PPDF(P)\,\mathrm{d}P}{\int \frac{PPDF(P)}{\eta(P)}\,\mathrm{d}P} \tag{2.102}$$

an assumption on the amplitude statistics of the modulated signal must be made. The Rayleigh power distribution [9] is used in order to approximate the power statistics of a communication signal

$$PDF(P) = \frac{1}{\gamma}\, e^{-\frac{P}{\gamma}} \tag{2.103}$$

with $\gamma = 10^{-\frac{PAPR[dB]}{10}}$. For the average efficiency results shown in Fig. 2.28 the PAPR was set to 6.45 dB.

It has been demonstrated in section 2.3 that the efficiency function $\eta(P_{out})$ depends on the explicit choice of a drive function. For the efficiency analysis shown here, the drive function in the load modulation region, by definition, follows the linear drive function circle until it intersects the equi-clip contour, which is then followed until full state power is reached (s. $dflin$ in Fig. 2.21). In the low power region ($P \leq P(BO)$, $\Gamma = 0$), a Class-B efficiency slope $\eta(P) = \frac{\pi}{4}\sqrt{\frac{P}{P(BO)}}$ is assumed.

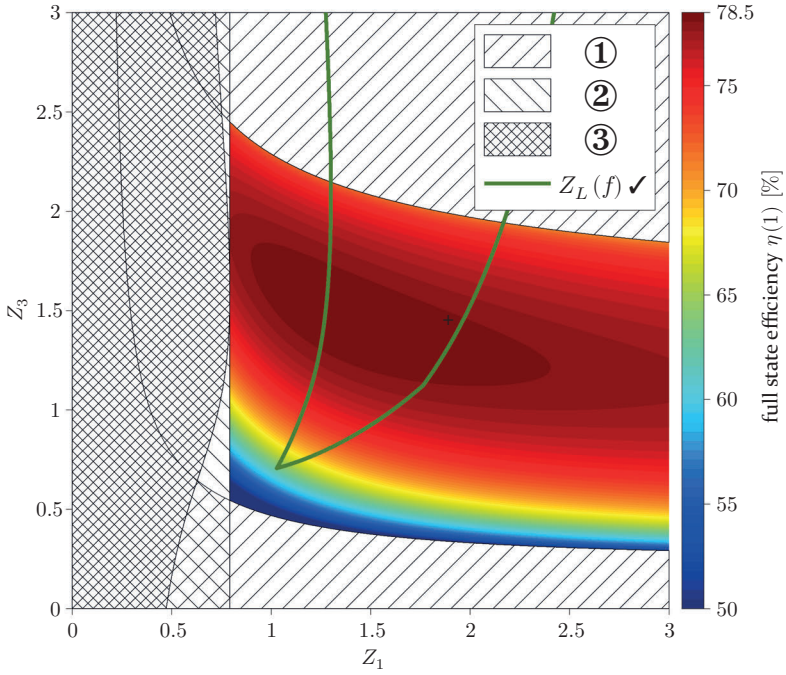

Figure 2.27: Full state efficiency $\eta(1)$ in $[Z_1, Z_3]$-space

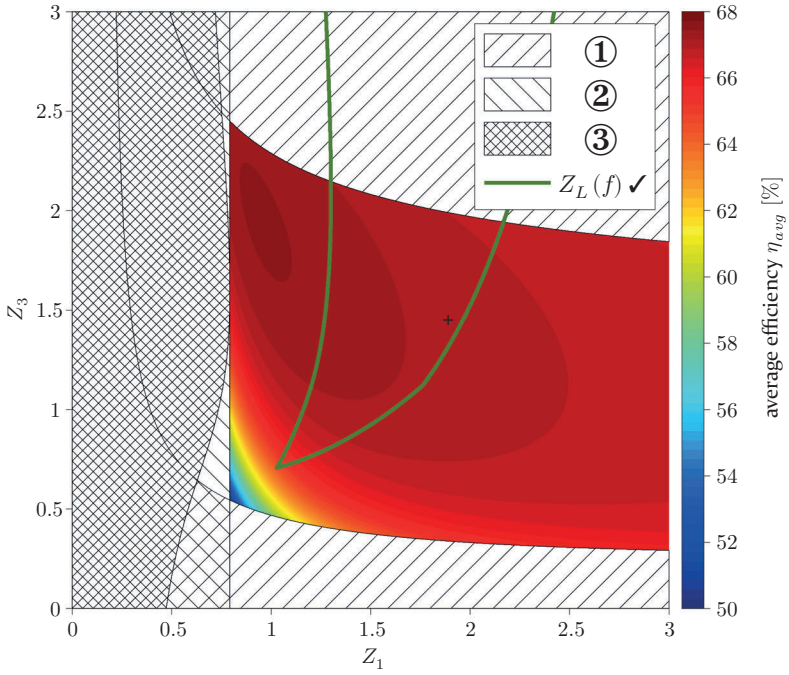

Figure 2.28: Average efficiency η_{avg} for a 6.45 dB PAPR Rayleigh signal in $[Z_1, Z_3]$-space

2.4.5 Full state balance

Based on the normalization that was introduced in section 2.1.6, in particular the first linearity criterion and the assumption that both amplifier cores shall saturate at full state, it has been shown that the full state current and power ratios at center frequency are functions of the backoff parameter BO, according to the relation

$$\frac{|I_P|}{|I_M|} = \frac{P_P}{P_M} = \frac{1}{BO} - 1 \tag{2.104}$$

For the detuned combiner, however, these ratios will deviate from their center frequency value. It must be kept in mind that the current source models used here in order to simplify analytic treatment create a highly idealized situation. They will just source any current requested into any load presented to them, however odd it may be. A real world transistor, on the other hand, is limited in its current and power capabilities and will react reluctantly (or even become unstable in the worst case) if exposed to termination conditions that are too far off its normal operating range. Keeping full state current and power balance within reasonable limits around their center frequency values is therefore mandatory in order to allow for an actual implementation of the results.

Another point to be considered is the power utilization factor, which is a measure for the transistor periphery that is to be installed in an amplifier versus the power that is actually taken out of that transistor, traditionally defined as

$$PUF = \frac{P_{out}}{U_{DS,max} I_{DS,max}} \tag{2.105}$$

Referred to the average power of the signal, this measure will in any case be painfully low due to the high crest factor of the signals to be amplified. This is especially true for the peak amplifier core in a DPA. It is therefore highly desirable to not further degrade the power utilization of the transistors by allowing the full state power ratio in the wideband DPA to vary too much over the bandwidth. Figures 2.29 and 2.30 show the full state current and power ratios at the band edges. The respective value at center frequency is $\frac{|I_P|}{|I_M|} = \frac{P_P}{P_M} = 1$.

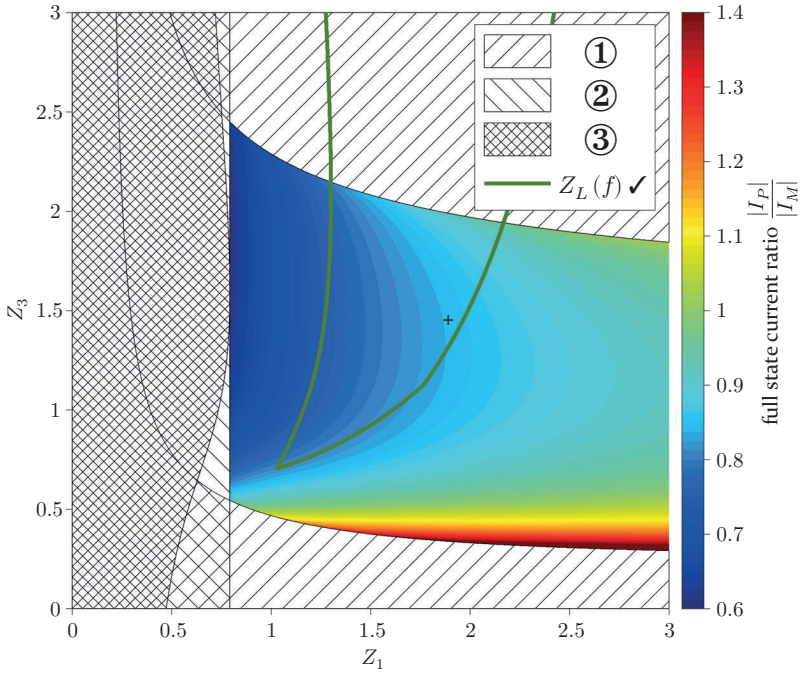

Figure 2.29: Full state current ratio $\frac{|I_P|}{|I_M|}$ in $[Z_1, Z_3]$-space

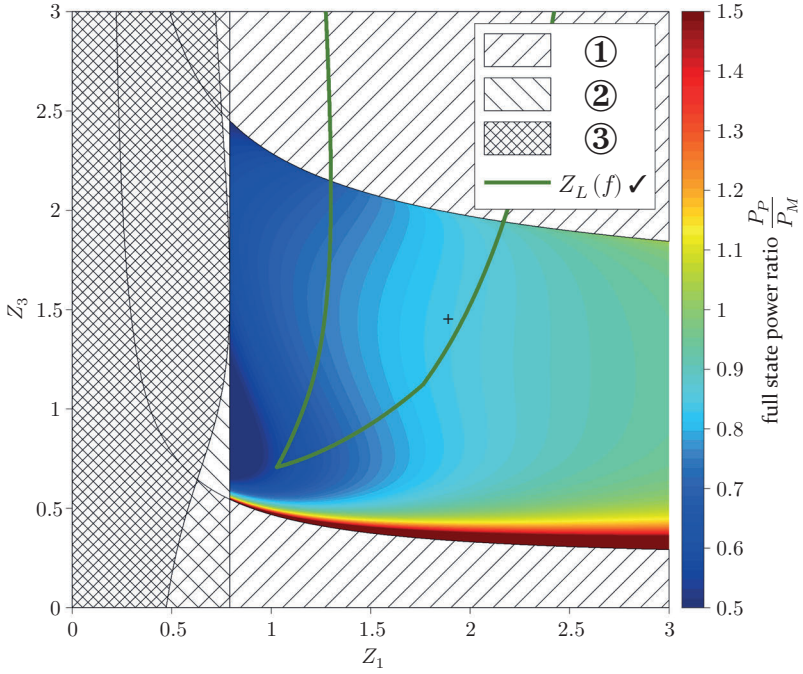

Figure 2.30: Full state power ratio $\frac{P_P}{P_M}$ in $[Z_1, Z_3]$-space

2.4.6 Conclusion

In order to allow for a comparison between different wideband techniques at the end of this chapter, an exemplary set of optimum combiner parameters is chosen for the Class-B case with $Z_2 = Z_1\,Z_3$, which has been examined so far. Evaluating the results of the design space analysis, we notice that the choice of parameters Z_1 and Z_3 within most of the feasible region has a rather marginal impact on average efficiency. This result is not surprising, due to the PDF of the Rayleigh signal causing average efficiency to be determined mainly in the backoff region, where efficiency is independent of the choice of Z_1 and Z_3. The impact on the distance $|\Gamma\,(int) - \Gamma\,(1)|$ is also marginal. The exemplary choice of optimum combiner parameters[16], $Z_1 = 1.9$ and $Z_3 = 1.45$, summarized in Table 2.1, is therefore mainly aimed at keeping full state balance as close as possible to its center frequency value and maximizing the linear power range, defined by $P\,(int)$. The corresponding load modulation space and amplitude domain representation of the drive function are shown in Figures 2.31 and 2.32, respectively.

	Z_1	Z_2	Z_3	$\eta(1)$	η_{avg}	$\lvert\Gamma\,(int) - \Gamma\,(1)\rvert$	$P(int)$	$\frac{\lvert I_P\rvert}{\lvert I_M\rvert}$	$\frac{P_P}{P_M}$
Class-B $Z_2 = Z_1\,Z_3$ center frequency	1.90	2.76	1.45	78.54	65.23	0	1	1	1
Class-B $Z_2 = Z_1\,Z_3$ band edge	1.90	2.76	1.45	78.17	67.05	0.36	0.64	0.84	0.84

Table 2.1: Summary of exemplary results for the Class-B case with $Z_2 = Z_1\,Z_3$

[16] Marked by a cross in previous diagrams of the $[Z_1, Z_3]$-space.

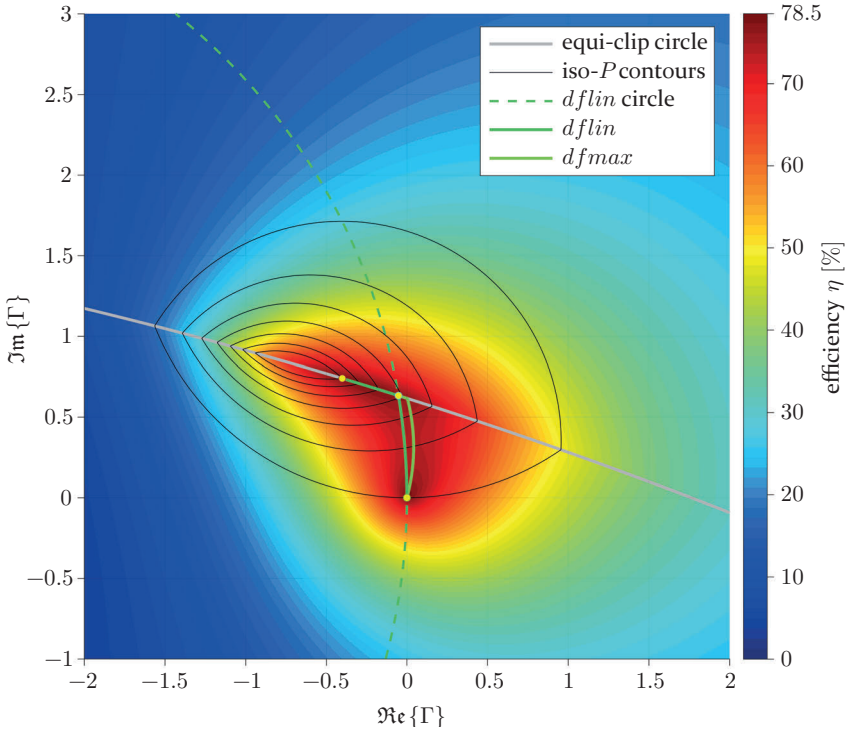

Figure 2.31: Load modulation space for $Z_1 = 1.90$, $Z_2 = 2.76$ and $Z_3 = 1.45$ at $\frac{f}{f_0} = 1.25$

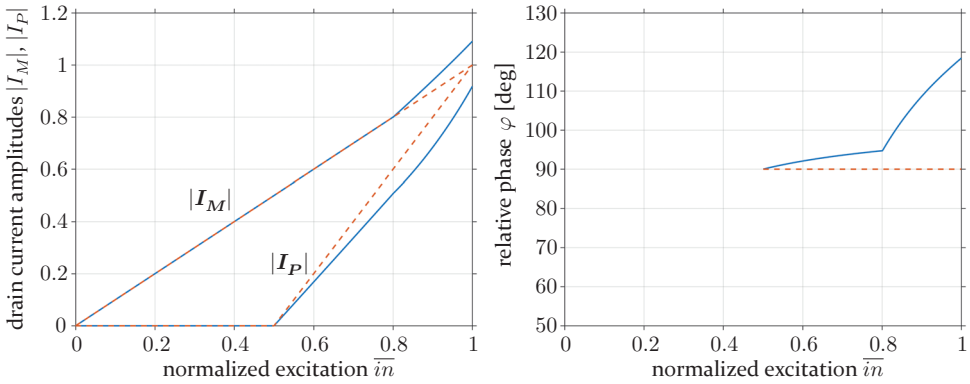

Figure 2.32: Band edge (blue) and center frequency (red dotted) drive functions vs. normalized excitation $\overline{in}$

It is interesting to note that the average efficiency at the band edges is higher than the average efficiency at center frequency. This is due to the fact that the smaller Doherty load modulation range followed by a 'quasi-outphasing' load modulation range provides higher instantaneous efficiencies than the linear Doherty mode at center frequency (s. Fig. 2.33). In conclusion, it can be stated that, besides adding significant insight, the new wideband DPA design techniques introduced so far – quasi left handed loads and non-linear drive functions based on load modulation space analysis – already provide a wideband DPA solution that goes distinctly beyond the state of the art. However, two major issues remain. One is the degree of drive function non-linearity required due to the transition from the Doherty mode to a 'quasi-outphasing' mode. Although it is difficult to predict the feasibility of such a solution without looking very deep into the signal processing field, we can safely assume that it would make things easier if we had a solution that inherently fulfilled the second linearity criterion defined in 2.3.5. The other issue lies in the assumption of a wideband Class-B operation, a problem that non of the previous works on wideband DPAs ever addressed. Such an amplifier would require a wideband 2nd harmonic short at the transistors intrinsic drain, which is physically impossible as it contradicts Foster's reactance theorem. Both of these issues will be addressed in the following sections.

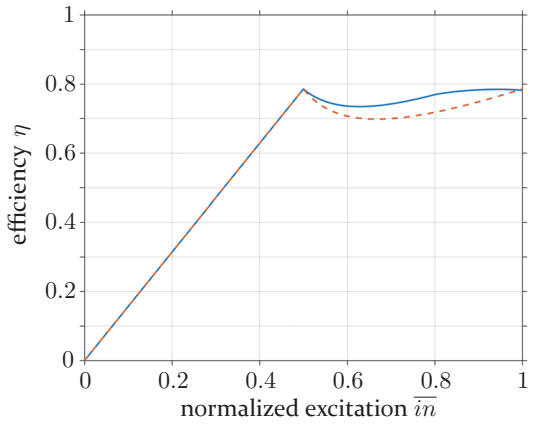

Figure 2.33: Instantaneous efficiency at band edges (blue) and center frequency (dottet red)

2.5 Analysis of the Class-J load modulation space

It was an early objective of this work to explore the feasibility and potential of continuous, linear waveform engineering techniques in Doherty-type active load modulation RFPAs. This combination of wideband and high efficiency RFPA design techniques seemed self-evident, but has not received proper

attention in the literature yet. The load modulation space analysis presented so far is a byproduct of that effort. It provides the tools and insights necessary to understand the implications that wideband, continuous operating modes have on the performance of a Doherty-type active load modulation RFPA. However, extending the analysis to Class-J operating modes holds some further challenges which will be discussed in the following, beginning with a brief introduction to the Class-J continuum of linear operating modes.

2.5.1 Introduction to Class-J theory

The theory of continuous linear RFPA operating modes, commonly referred to as the Class-J continuum, has been proposed by Cripps et al. in [45]. It addresses the problem of providing an adequate wideband termination to the 2nd harmonic component in the output transistors drain current. As has been outlined in chapter 1, higher harmonic components are inherent to reduced conduction angle modes, which, in turn, are essential to the design of efficient and linear RFPA's. Cripps stated that 'this presents significant problems when performance is specified over a significant bandwidth; a simple shunt resonator will present an increasingly negative (lower frequencies) and positive (higher frequencies) reactive termination to harmonic current components, which degrade the power and efficiency available for linear operation'. He proposed a continuum of voltage waveforms that satisfy the equation

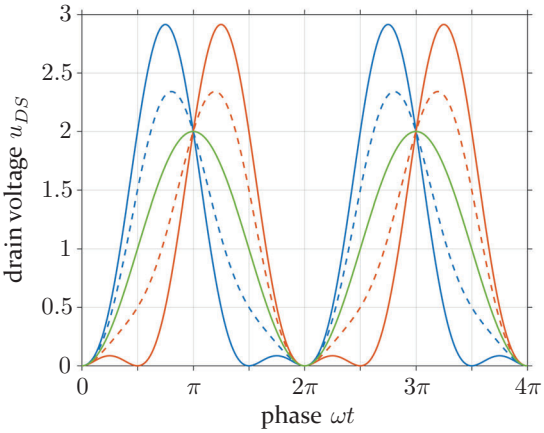

Figure 2.34: The continuum of Class-J voltage waveforms: $\alpha = -1$: Class-J^{-1} (blue), $\alpha = 0$: Class-B (green), $\alpha = 1$: Class-J (red)

$$u_{DS}(\omega t) = (1 - \cos(\omega t))(1 - \alpha \sin(\omega t)) \tag{2.106}$$

with $-1 \leq \alpha \leq 1$.

A waveform that satisfies Eq. 2.106 cannot assume negative values. They all have the same minimum value of zero and are therefore suitable for linear PA operation[17]. Furthermore, all of these waveforms produce equal DC and fundamental power components and thus deliver the same full state output power and efficiency. Based on the assumption of a certain current waveform, usually a cosine pulse with a conduction angle of π (Class-B) as defined in 2.1.2, the Class-J voltage waveform continuum defined by Eq. 2.106 can be mapped to a termination impedance continuum

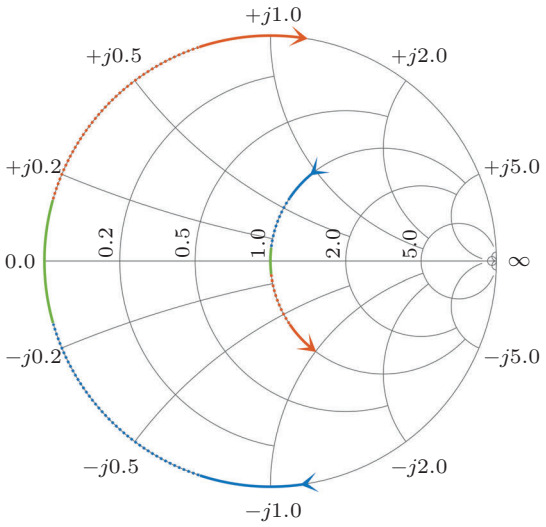

Figure 2.35: Class-J termination continuum (Fundamental frequency response on the $R = 1$ circle, 2nd harmonic response on the edge of the Smith chart, colouring according to Fig. 2.34)

$$Z_{f0} = R_0 - j\alpha R_0 \quad (2.107)$$

$$Z_{2f0} = j2\alpha \frac{a_2}{a_1} R_0 \quad (2.108)$$

with a_1 and a_2 representing the fundamental and 2nd harmonic Fourier coefficients of the drain current pulse (s. Eq. 2.6). For the Class-B pulse, we get

$$Z_{2f0} = j\alpha \frac{3\pi}{8} R_0 \quad (2.109)$$

Instead of being limited to a harmonic short circuit, which can only be realized for a single frequency, the Class-J continuum allows a reactive termination of the 2nd harmonic to be compensated by an opposite signed reactive termination component at the fundamental frequency. When a properly designed frequency response of the fundamental and second harmonic termination impedances, with the reactive parts rotating in opposite directions to each other (s. Fig. 2.35), is provided, the Class-J continuum enables efficient and

[17] Knee voltage not taken into account.

linear RFPA operation in a bandwidth of (theoretically) up to one octave [46], [47]. The price for the Class-J waveforms is a slightly higher voltage stress on the active devices.

2.5.2 Class-J clipping factors

By definition, the clipping factors of the ideal Class-J waveforms (Eq. 2.106) equal those of the corresponding Class-B waveform. But while we can ensure ideal Class-J operation at backoff by providing the optimum Class-J load match, as outlined in 2.2.2, this assumption generally becomes invalid under load modulation[18]. In order to extend the Class-B load modulation space analysis to Class-J type operating modes, the analysis may not be restricted to ideal Class-J waveforms but has to allow for general two-harmonic voltage waveforms

$$u_{DS}(\omega t) = \cos(\omega t) + a\cos(2\omega t + \varphi) \tag{2.110}$$

Unfortunately, the clipping factors c_M and c_P of the general two-harmonic voltage waveform cannot be expressed in closed form as easily as the Class-B clipping factors. When trying to calculate the minima of the general two-harmonic waveform, we end up with a 4^{th} order polynomial

$$0 = e^{j4\omega t} + 2ae^{-j\varphi}\left(e^{j3\omega t} - e^{j\omega t}\right) - e^{-j2\varphi} \tag{2.111}$$

which cannot be solved in closed form conveniently[19]. The identification of the minima is therefore done numerically. This also means that the geometrical structures that were used in the analysis of the Class-B load modulation space, in particular the equi-clip contour and the iso-P contours, can no longer be expressed by circles. The underlying concepts are nevertheless fully applicable to the Class-J load modulation space, but they assume more sophisticated shapes, which have to be constructed with the help of numerical algorithms[20].

[18] It is possible to arbitrarily enforce ideal Class-J termination conditions at either the main amplifier core or the peak amplifier core throughout the load modulation range by choosing the drive function accordingly, but this will result in suboptimal performance. Maintaining optimum Class-J conditions at both amplifier cores simultaneously is practically impossible.

[19] At least not by the author of this work...

[20] With respect to the scope of this work, the Matlab program code of the algorithms that have been developed and used for the analysis presented in the following sections will not be discussed here in detail.

2.5.3 Class-J linear drive function

There is one important exception to what was said in the last paragraph: The linear drive function circle, as introduced in 2.3.3, maintains its circular properties in the Class-J load modulation space. This becomes clear when we look at the underlying equation

$$c_M^2 \frac{P(BO)}{c_M(BO)^2} = \frac{1}{2} c_M^2 \left(\mathfrak{Re}\{Z_M\} + \mathfrak{Re}\{Z_P\} |\Gamma|^2 \right) \tag{2.112}$$

The actual clipping factor c_M is cancelled out and the backoff term $\frac{P(BO)}{c_M(BO)^2}$ maintains its Class-B value throughout the bandwidth, since, at backoff, ideal Class-J operation is assumed (3.2.2). Thus, the Class-J termination of the 2nd harmonic does not affect the linear drive function directly, but it affects the position and shape of the equi-clip contour and therefore also the position of the $dflin$/equi-clip intersection point.

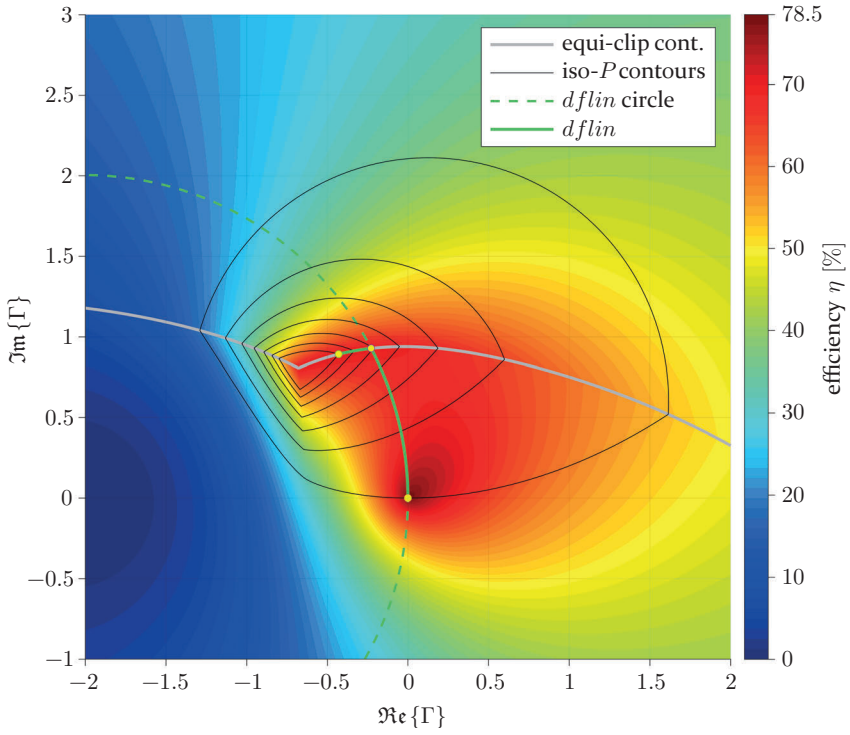

Figure 2.36: Load modulation space for $Z_1 = 1.07$, $Z_2 = 0.87$, $Z_3 = 0.81$, $Z_{i,M} = 2$ and $Z_{i,P} = 1$ at $\frac{f}{f_0} = 1.25$

Figure 2.36 shows an example of a typical Class-J load modulation space. Most noticeable, there is a distinct discontinuity in the derivative of the equi-clip contour and the c_M-limited iso-P contours, which corresponds to a transition between the two local minima of the general two-harmonic voltage waveform. We also see that the euclidean distance $|\Gamma(int) - \Gamma(1)|$ has become significantly shorter than in the Class-B case. In the following section, the previously established methods of combiner design space analysis are applied to the Class-J combiner design space in order to obtain a more complete picture of Class-J type operation under active load modulation.

2.6 Analysis of the Class-J combiner design space

In order to examine the effects that a Class-J termination at backoff has on load modulation performance, complex termination conditions will be introduced to the design space analysis by modifying the parameter Z_i defined in section 2.2.2. $Z_{i,M}$ sets the reactive part of the main amplifier core's fundamental frequency termination at backoff (s. Eq. 2.40) by acting upon the load match $Z_L(\Theta)$ (Eq. 2.42), as well as the second harmonic termination impedance $Z_{M,2f0}$ (Eq. 2.41), which is used for the numerical calculation of the clipping factor c_M. For a given relative bandwidth BW, the valid range for $Z_{i,M}$ is

$$0 \leq Z_{i,M} \leq R_M(BO) \tan\left(\frac{\pi}{2}\left(1 + \frac{BW}{2}\right)\right) \tag{2.113}$$

$Z_{i,M} = 0$ corresponds to wideband Class-B operation, while the upper limit corresponds to full Class-J operation ($\alpha = 1$ in Eq. 2.106) at the band edge[21]. In addition, we will also introduce a reactance parameter $Z_{i,P}$ to the peak amplifier core's termination. For the sake of consistency, this parameter is defined analogously to $Z_{i,M}$, although it only affects the peak amplifier core's second harmonic termination used for the calculation of the clipping factor c_P. As previously demonstrated for the Class-B case, the design space analysis is based on the the knowledge of the points $\Gamma(int)$ and $\Gamma(1)$, which are obtained by means of load modulation space analysis. Since the analysis

[21] Note that this upper limit refers to the main amplifier cores termination resistance at backoff $R_M(BO)$. It is self-evident that, in order to be able to maintain acceptable termination conditions under load modulation, which is meant to decrease the fundamental termination resistance but leaves the 2nd harmonic termination reactance constant, $Z_{i,M}$ must be chosen significantly lower.

of a multi-dimensional combiner design space requires a very high number of load modulation spaces to be examined and a simple closed-form solution is not available for the Class-J case, it is absolutely crucial to have an algorithm at hand that constructs the Class-J drive function in a computationally efficient way. Due to its importance to the design space analysis, the main branch of the algorithm that has been used in order to obtain adequate drive function data will be described briefly. It can be broken down into two stages:

1. The load modulation factor is swept along the linear drive function circle in discrete steps in the direction of increasing power until a change of sign in the term $c_M(\Gamma) - c_P(\Gamma)$ is detected. The step width is adjusted dynamically so that individual zero crossings in close proximity to each other can be distinguished reliably. A non-linear solver, constraint to the interval in which the change of sign was detected, is then applied in order to find the exact position of the intersection point with the equi-clip contour on the $dflin$ circle.

2. If the output power at the intersection point is smaller than the targeted full state power, a fast search algorithm follows the equi-clip contour from the intersection point onwards in discrete steps in the direction of increasing power, until the targeted full state power is reached. If the output power at the intersection point is larger than the targeted full state power, the angle on the linear drive function circle is turned back until the targeted full state power is reached.

Conditional branches and side conditions encountered by the algorithm during load modulation space analysis lead us straight to the definition of boundary conditions for the Class-J combiner design space.

2.6.1 Boundary conditions

The three boundary conditions that were defined in the analysis of the Class-B combiner design space (2.4.1) apply to the Class-J design space as well. Their definitions remain unaltered, only the methods of identification change, due to the numeric nature of the Class-J design space analysis. In addition to that, the Class-J combiner design space gives rise to the definition of three new boundary conditions, which will also be introduced in the following.

① Boundary condition 1 evaluates if **the maximum output power available in the load modulation space is higher than the targeted full state power**. For the Class-J case, this is done by using a two-dimensional unconstrained non-linear solver to find the point of maximum power in the load modulation space.

② Boundary condition 2 evaluates if $\boldsymbol{c_M(BO) < c_P(BO)}$ (i.e. the backoff point is c_M-clipped). The backoff clipping factors are found numerically.

③ Boundary condition 3 evaluates if **the linear drive function circle intersects the equi-clip contour**. It is violated if step 1 of the algorithm described previously is completed without detecting a change of sign in $c_M(\Gamma) - c_P(\Gamma)$.

④ Boundary condition 4 states that **the linear drive function circle intersects the full state power contour before it reaches the equi-clip condition**. It is set if the power at the intersection point is larger than the targeted full state power. This condition implies that the second linearity criterion is fulfilled.

⑤ Boundary condition 5 is a subset of condition 3. It states that **the linear drive function circle intersects the full state power contour but**, unlike condition 4, **never reaches the equi-clip condition**. This condition is evaluated by searching for a change of sign in the term $P(\Gamma) - P(1), \Gamma \in \{dflin\}$, in a side branch of the algorithm in case boundary condition 3 is violated while 1 and 2 are met. An example of a load modulation space that fulfills condition 5 is given in Figure 2.37.

⑥ Boundary condition 6 states that $|\boldsymbol{P(\Gamma) - P(1)}|, \boldsymbol{\Gamma \in \{equi-clip\}}$, **has a local minimum before the equi-clip contour actually intersects the full state power contour**. Expressed in a more descriptive way, this means that the drive function will run in parallel to the full state power contour for a while and intersect it from its 'back-side' as illustrated in Figure 2.38. The issue could be avoided by using a more sophisticated drive function definition, but this was omitted because the region in which it occurs is irrelevant to the task of finding an optimum set of combiner parameters. Nevertheless, it provides a good example of the challenges that must be faced when analyzing multi-harmonic load modulation spaces.

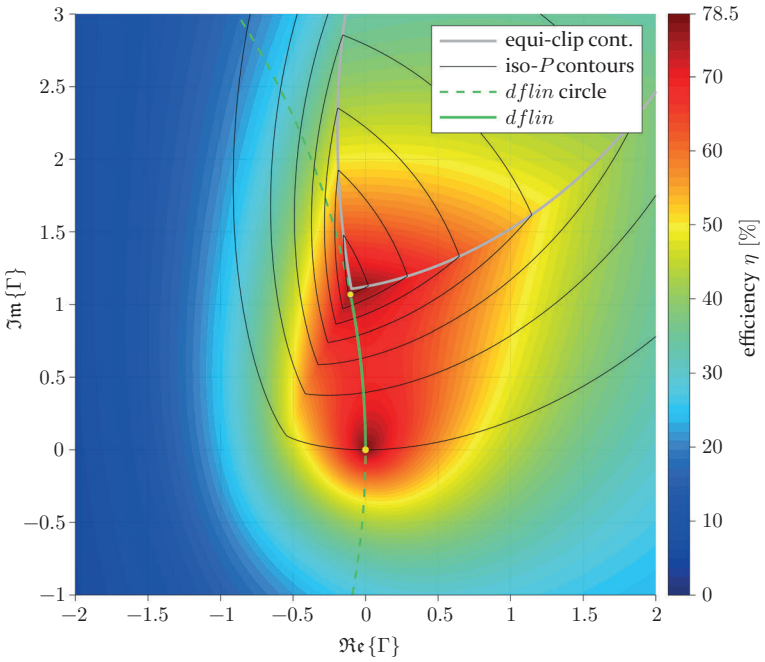

Figure 2.37: Example of a violation of boundary condition ⑤ ($Z_1 = 2.65$, $Z_3 = 0.4$, $Z_2 = Z_1\,Z_3$, $Z_{i,M} = 3$, $Z_{i,P} = 0$, $R_M = 2$, $\frac{f}{f_0} = 1.25$)

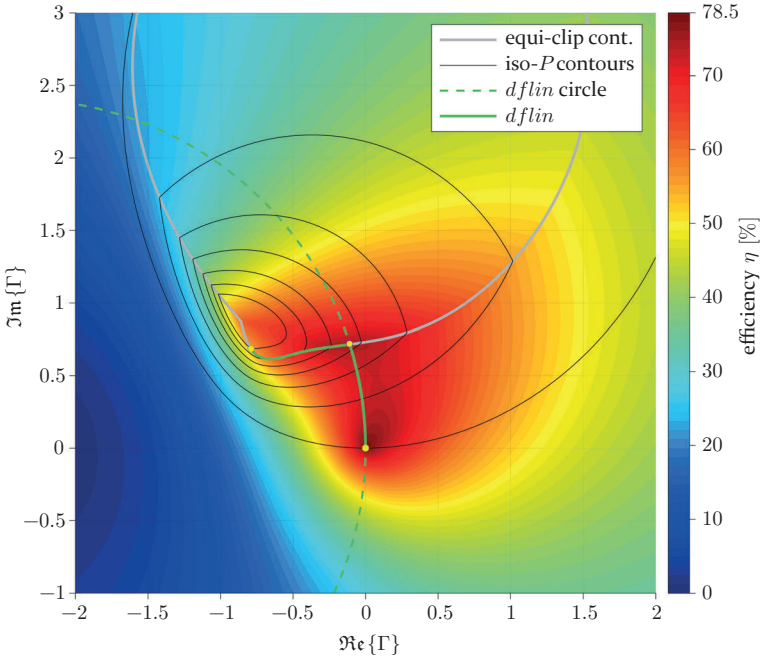

Figure 2.38: Example of a violation of boundary condition ⑥ ($Z_1 = 1.25$, $Z_3 = 0.18$, $Z_2 = Z_1\,Z_3$, $Z_{i,M} = 1$, $Z_{i,P} = 1$, $R_M = 2$, $\frac{f}{f_0} = 1.25$)

2.6.2 Class-J performance and feasibility criteria

For the Class-B case, analytic expressions for the output power and the instantaneous efficiency were available for each section of the drive function (i.e. the low power region, the $dflin$ region and the equi-clip region). In the Class-J case, however, the drive function is constructed in an iterative manner, resulting in a discrete, non-equidistant set of points. To accommodate this, average efficiency is calculated using

$$\eta_{avg} = \frac{\sum_{i=1}^{n} \int_{P_{i-1}}^{P_i} PDF(P) \frac{P_{i-1}+P_i}{2} \, \mathrm{d}P}{\sum_{i=1}^{n} \int_{P_{i-1}}^{P_i} PDF(P) \frac{P_{i-1}+P_i}{\eta_{i-1}+\eta_i} \, \mathrm{d}P} \tag{2.114}$$

As for the Class-B average efficiency, a Rayleigh PDF (Eq. 2.103) with a PAPR of 6.45 dB and a Class-B efficiency slope in the low power region is assumed.

Based on the knowledge of $\Gamma(int)$, $\Gamma(1)$ and the numerically calculated clipping factors at these points, the other performance criteria (i.e. drive function non-linearity, full state balance and full state efficiency) are evaluated in accordance with the Class-B case. Likewise, the feasibility of the wideband load match $Z_L(\Theta)$ is assessed, based on the criteria that have been introduced in 2.4.2. The feasible Z_L-ranges must, of course, be recalculated when changing the main amplifier core's backoff reactance parameter $Z_{i,M}$, as this parameter directly affects $Z_L(\Theta)$ (s. Eq. 2.42). $Z_{i,P}$, on the other hand, has no effect on the load match. On the following pages (Figs. **??** to 2.44), the results of the Class-J design space analysis are illustrated for a discrete set of backoff reactance parameters $Z_{i,M} \in \{1,2,3\}$[22] and $Z_{i,P} \in \{0,1\}$. All other parameters are set in accordance with the Class-B case, $\frac{f}{f_0} = 1.25$, $BO = \frac{1}{2}$, $Z_2 = Z_1 \, Z_3$ and $Z_L = Z_L(\Theta)$ as given in Eq. 2.42.

[22] The theoretical upper limit (Eq. 2.113) would, in this case, be at $Z_{i,M} \approx 4.83$.

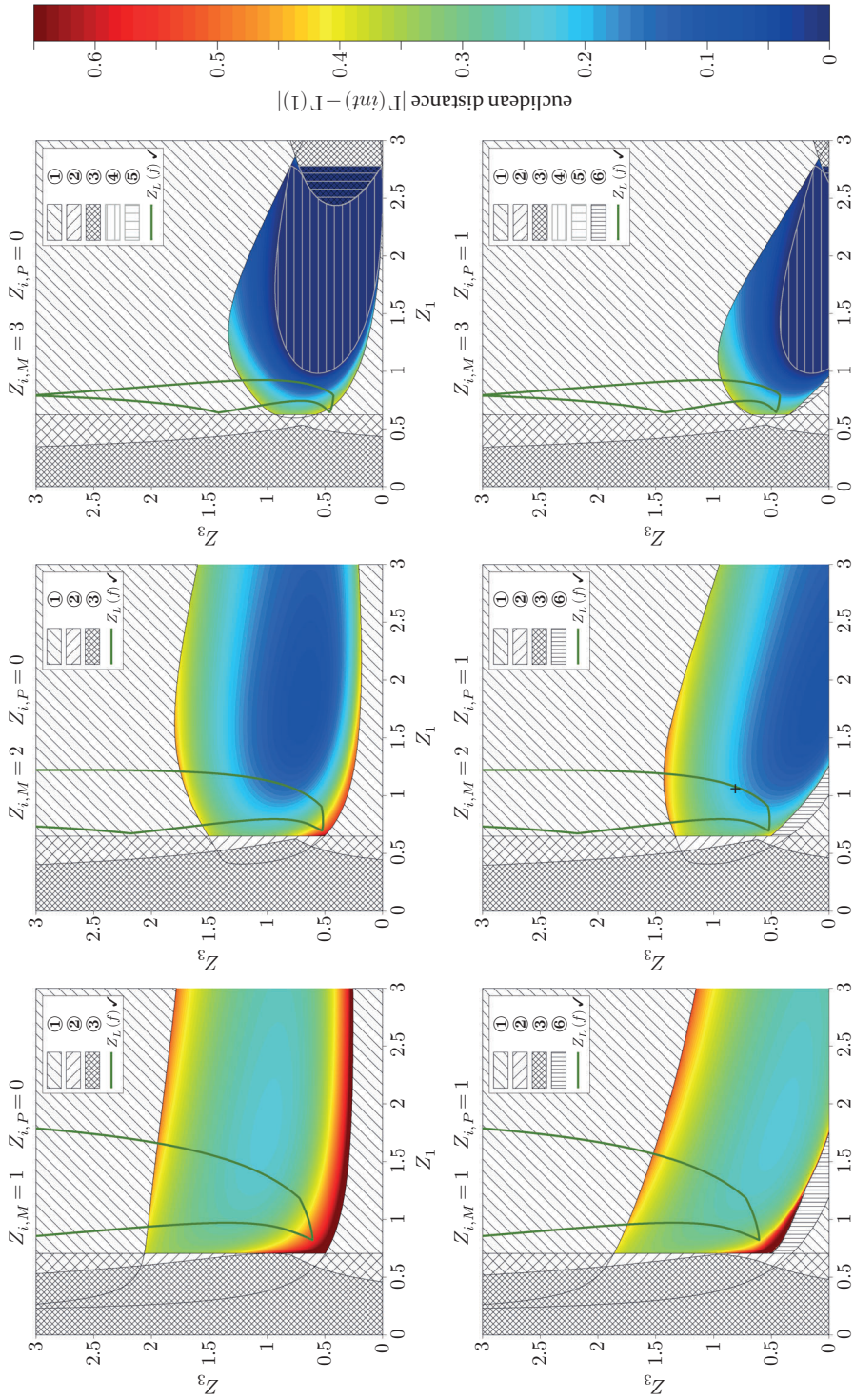

Figure 2.39: Euclidean distance between $dflin$/equi-clip intersection and full state load modulation factor for various backoff reactance parameters $Z_{i,M}$ and $Z_{i,P}$

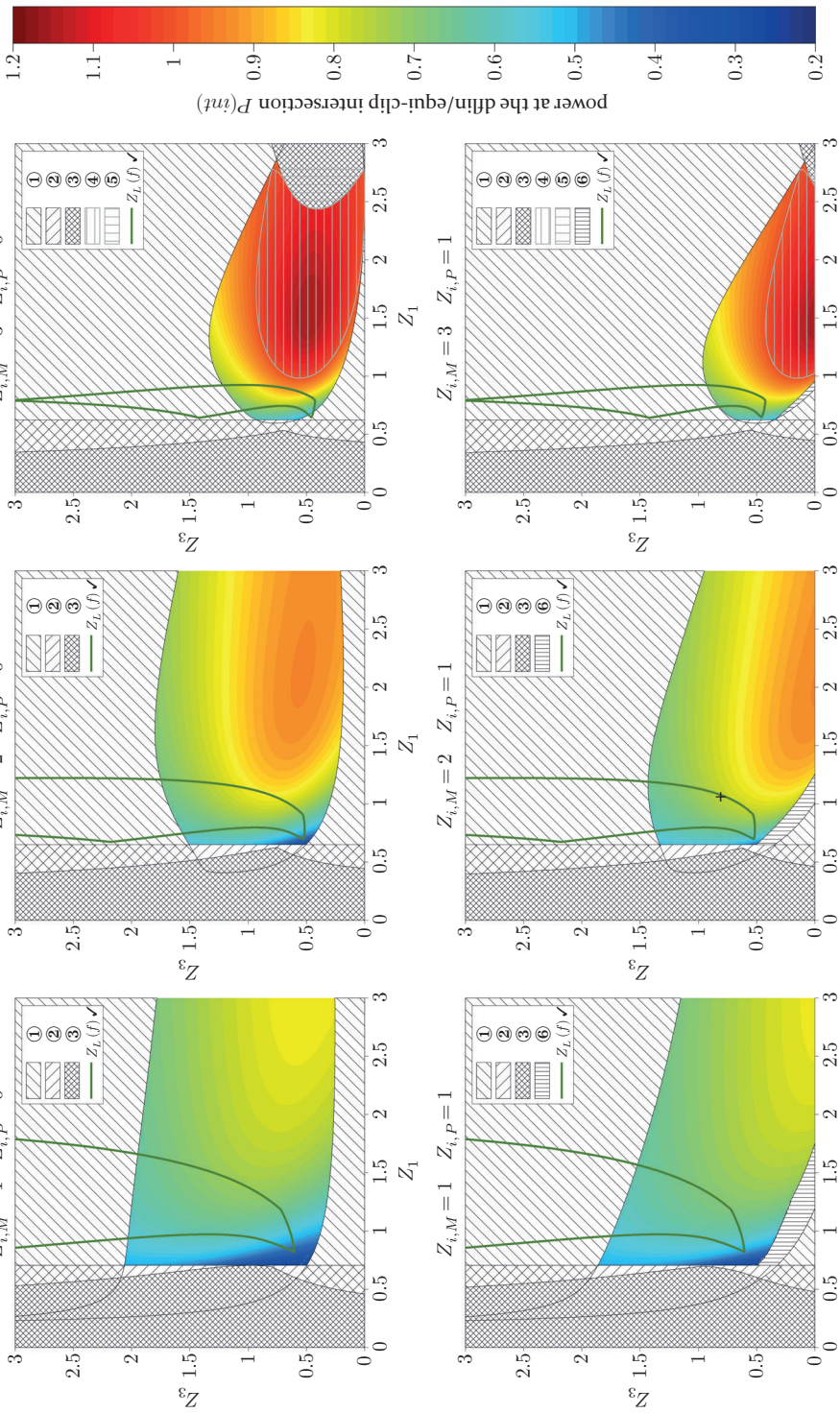

Figure 2.40: Power at $dflin$/equi-clip intersection for various backoff reactance parameters $Z_{i,M}$ and $Z_{i,P}$ ($R_M = 2$, $\frac{f}{f_0} = 0.75$)

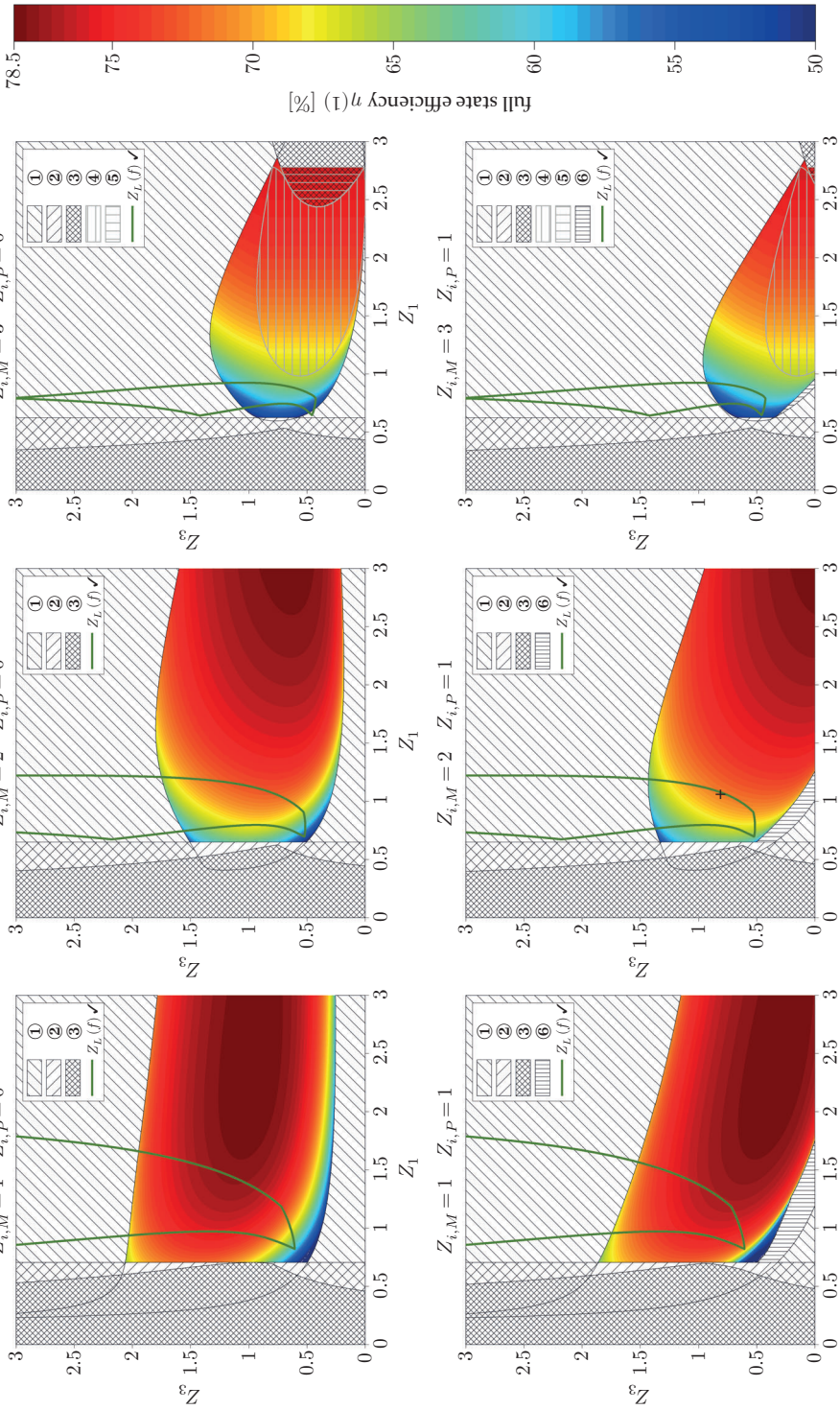

Figure 2.41: Full state efficiency for various backoff reactance parameters $Z_{i,M}$ and $Z_{i,P}$ ($R_M = 2$, $\frac{f}{f_0} = 0.75$)

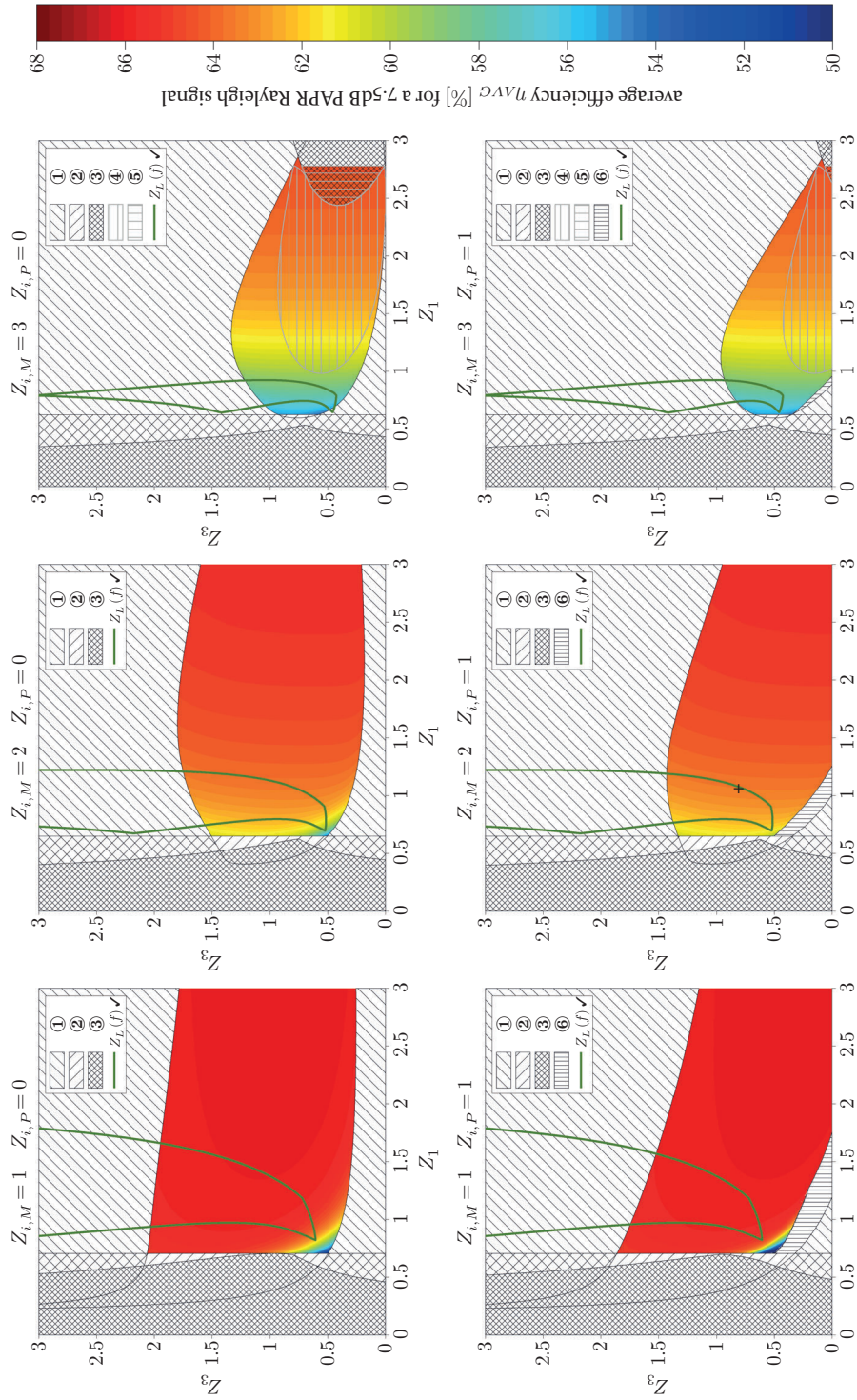

Figure 2.42: Average efficiency for various backoff reactance parameters $Z_{i,M}$ and $Z_{i,P}$ ($R_M = 2$, $\frac{f}{f_0} = 0.75$)

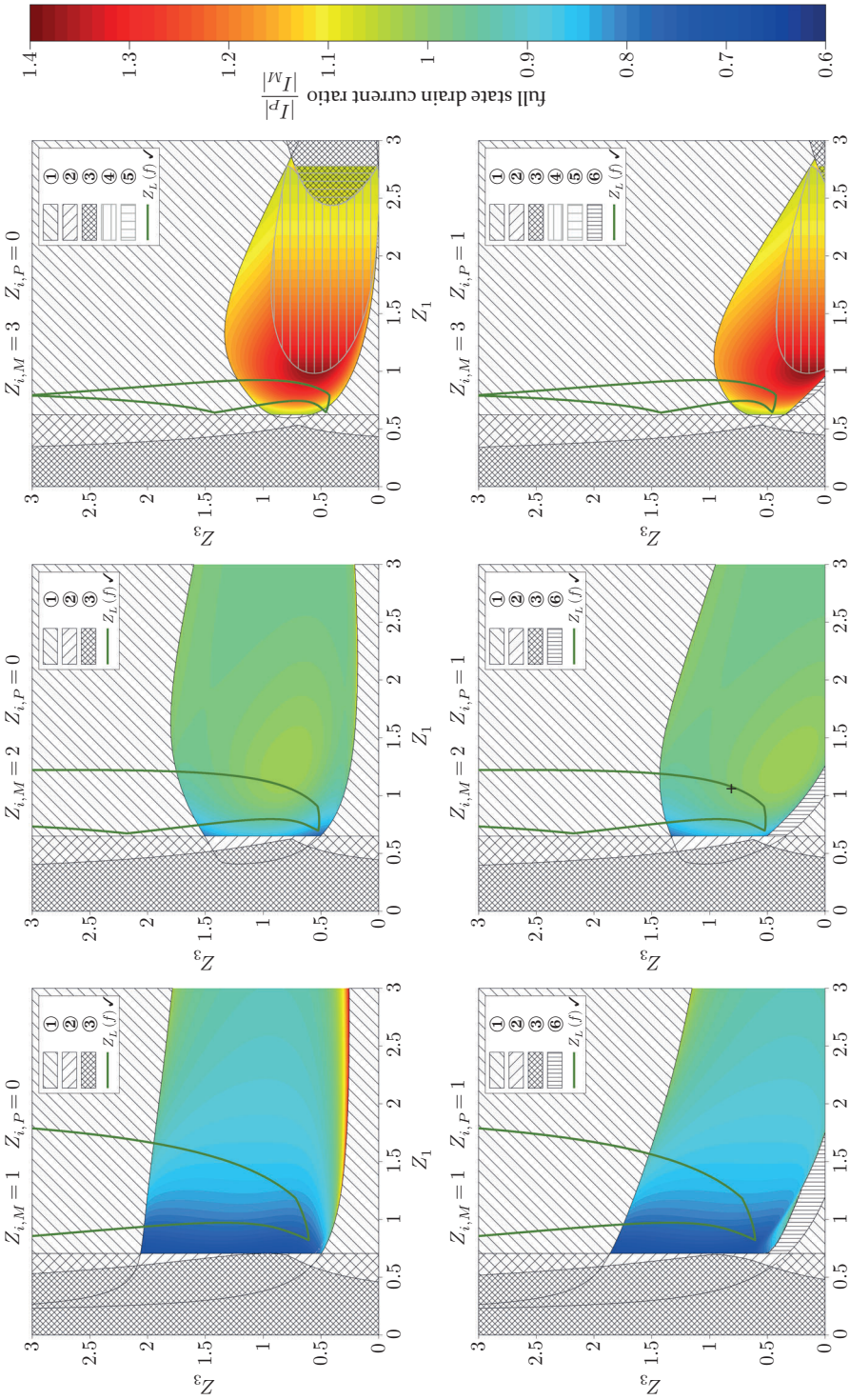

Figure 2.43: Full state current ratio for various backoff reactance parameters $Z_{i,M}$ and $Z_{i,P}$ ($R_M = 2$, $\frac{f}{f_0} = 0.75$)

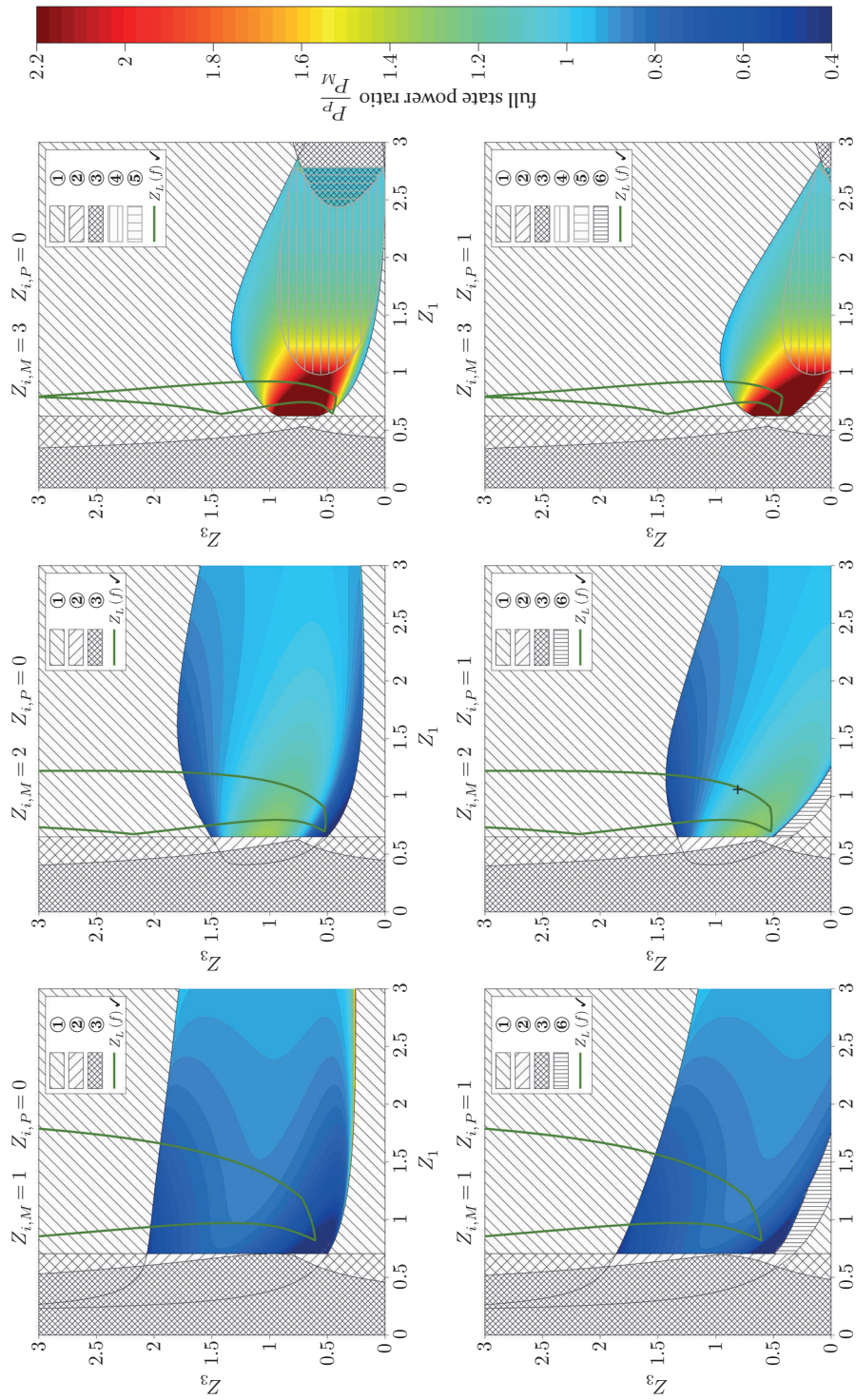

Figure 2.44: Full state power ratio for various backoff reactance parameters $Z_{i,M}$ and $Z_{i,P}$ ($R_M = 2$, $\frac{f}{f_0} = 0.75$)

2.6.3 Conclusion

Providing Class-J termination conditions to the main amplifier core at backoff extends the linear Doherty range of the detuned DPA under load modulation. Increasing $Z_{i,M}$ from 0 (Class-B) to 2 reduces the distance $|\Gamma(int) - \Gamma(1)|$ from $\sim$0.36 to $\sim$0.15 in the feasible Z_L region. The maximum output power of the linear Doherty mode, $P(int)$, is increased from $\sim$0.6 to $\sim$0.8 and full state balance is also improved significantly. Increasing $Z_{i,M}$ even further opens up a region in which $P(int)$ becomes larger than the targeted full state power (boundary condition 4), which means that the second linearity criterion would be fulfilled. However, implementing such a solution with a feasible wideband load match $Z_L(f)$ at the common node of the combiner would result in significant full state imbalance and insufficient efficiency under load modulation. Vice versa, a Class-J solution that is inherently linear and exhibits good efficiency performance under load, like the example shown in Fig. 2.37, would require an infeasible wideband load match $Z_L(f)$. It can be observed that increasing $Z_{i,M}$ generally has a deteriorating effect on efficiency in the load modulation region. In the Class-B case, average efficiency at the band edges was even higher than at center frequency, due to the presence of the non-linear 'quasi-outphasing' mode at high powers. Since the Class-J termination extends the linear Doherty range, some of that efficiency boost is lost in the Class-J case. In addition, full state efficiency in the Class-J case is slightly reduced since the ideal Class-J termination conditions cannot be fully maintained under load modulation.

It can be concluded that, by extending the linear Doherty range, the Class-J solution helps to improve drive function linearity and full state balance as compared to the Class-B solution, for the price of slightly reduced efficiency at high powers. After all, it would be misleading to judge the Class-J solution primarily for its effects on load modulation performance. The original intention behind its introduction to wideband DPA design was to optimize wideband performance at the backoff state by providing feasible multi-harmonic termination conditions at the backoff state. The work presented so far has shown that this is indeed possible and, furthermore, that it is compatible with active load modulation. When comparing the Class-J results to the Class-B results shown previously, it should always be kept in mind that the Class-B results are based on the invalid assumption of a wideband short circuit of the higher harmonics. For the sake of providing reasonable multi-harmonic termination conditions, a reactive second harmonic termination has also been presented to the peak amplifier core, although the results of the design space analysis

indicate that this has a negative effect on load modulation performance[23]. In accordance with the Class-B case, an exemplary choice of optimum Class-J combiner parameters, $Z_1 = 1.07$, $Z_3 = 0.87$ and $Z_2 = Z_1\,Z_3$, summarized in Table 2.2, is provided in order to simplify comparison. Fig. 2.45 shows the corresponding drive functions in amplitude domain. The corresponding load modulation space representation has been shown in Fig. 2.36.

	Z_1	Z_2	Z_3	$\eta(1)$	η_{avg}	$\lvert\Gamma(int)-\Gamma(1)\rvert$	$P(int)$	$\frac{\lvert I_P\rvert}{\lvert I_M\rvert}$	$\frac{P_P}{P_M}$
Class-J, $Z_{i,M} = 2$, $Z_{i,P} = 1$, $Z_2 = Z_1\,Z_3$ center frequency	1.07	0.87	0.81	78.54	65.23	0	1	1	1
Class-J, $Z_{i,M} = 2$, $Z_{i,P} = 1$, $Z_2 = Z_1\,Z_3$ band edge	1.07	0.87	0.81	71.29	63.52	0.20	0.76	0.99	1.06

Table 2.2: Summary of exemplary results for the Class-J case with $Z_2 = Z_1\,Z_3$

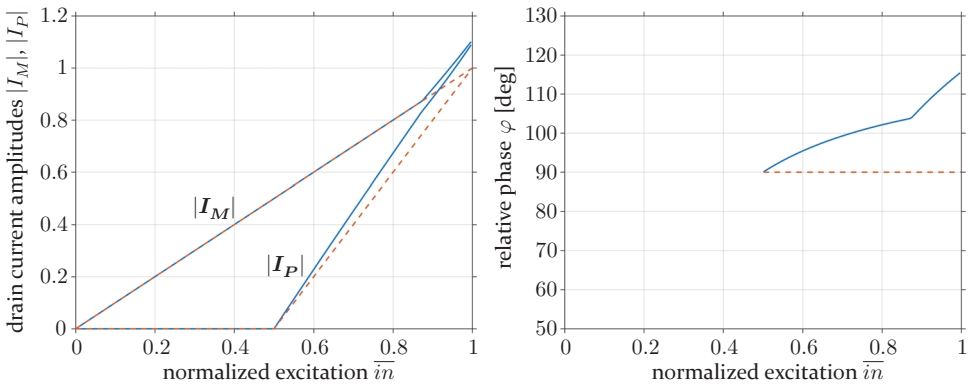

Figure 2.45: Band edge (blue) and center frequency (red dotted) drive functions vs. normalized excitation $\overline{in}$

The design space analysis revealed that a Class-J termination of the main amplifier core at backoff, as a side effect, improves linearity in the load modulation region. However, although theoretically possible, using Class-J termination conditions at backoff as a means to completely fulfill the second linearity criterion does not make much sense, since it impairs the other performance

[23] In this context, the concept of using a push-pull peak amplifier core in the wideband DPA, as reported in [43], should be seriously considered, since the push-pull configuration allows to keep the second harmonic reactance lower than in a single-ended configuration.

criteria in the load modulation region when used to that extent. Up to this point, the assumption $Z_2 = Z_1\,Z_3$, derived in 2.1.6 as a consequence of ideal Doherty operation at center frequency, was held up, since the author felt that it serves the main objective of this chapter, which is to improve the understanding of load modulation spaces and to investigate the effects of Class-J termination conditions under active load modulation. In the following section, it will be shown that dropping this assumption provides a generic way to fulfill the second linearity criterion, for the price of reduced center frequency performance.

2.7 Adaption of the center frequency transformation ratio

With regard to the characteristic impedances of the $\lambda/4$ transmission lines in the combiner, the condition $Z_2 = Z_1\,Z_3$ has been specified in subsection 2.1.6 and was used throughout the previous analysis of load modulation spaces and combiner design spaces. This relation resulted from the postulation of ideal Doherty behaviour at center frequency, which implies that the voltages at both amplifier cores are saturated at full state (Eq. 2.23). If that requirement is given up and the peak amplifier core voltage at center frequency allowed to remain unsaturated at full state, we are free to choose a different value of Z_2. Based on the knowledge about the structure of the load modulation space, we can deliberately choose $Z_2 > Z_1\,Z_3$ so that, for a certain detuning $\Theta = \frac{\pi}{2}\frac{f}{f_0}$ of the combiner, the maximum output power of the linear Doherty mode (i.e. the power at the intersection of the $dflin$ and equi-clip circles), $P(int)$, equals the targeted full state power and thus enforce the second linearity criterion. In this characteristic case, all of the six circles defined in section 2.3 (i.e. the $dflin$ and equi-clip circles, the iso-c circles for $c_M = 1$ and $c_P = 1$, as well as the c_M and c_P limited iso-P circles for $P = 1$ [24]) will intersect in a single point, the full state load modulation factor $\Gamma(1)$. Thus, based on the adaption of Z_2, the transition from the linear Doherty mode to a more non-linear 'quasi-outphasing' mode can be avoided completely, but this comes at the price of reduced center frequency efficiency. For further illustration, an example of Class-B load modulation spaces with adapted Z_2 at center frequency and band edge is given in Figures 2.46 and 2.47.

[24] iso-c and iso-P values refer to a symmetric DPA.

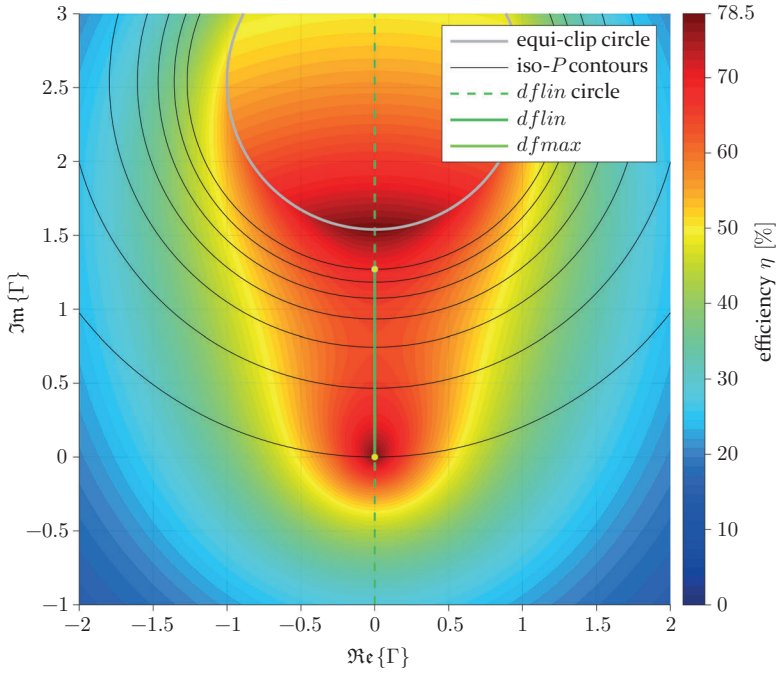

Figure 2.46: Load modulation space for $Z_1 = 1.65$, $Z_2 = 1.55$ and $Z_3 = 0.74$ at $\frac{f}{f_0} = 1$ [25]

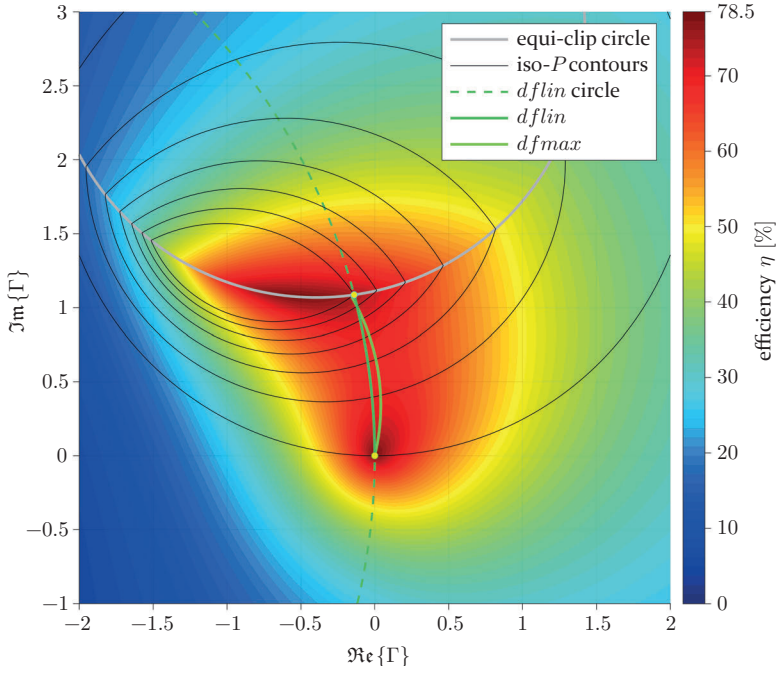

Figure 2.47: Load modulation space for $Z_1 = 1.65$, $Z_2 = 1.55$ and $Z_3 = 0.74$ at $\frac{f}{f_0} = 1.25$ [25]

In the following, some of the consequences that the outlined adaption of Z_2 has on the Class-B load modulation space analysis will be discussed. Subsequently, the impact on amplifier performance will be examined in detail by means of combiner design space analysis. Finally, the adaption of Z_2 will be applied to the Class-J DPA in section 2.9.

2.7.1 Class-B load modulation space analysis with adapted Z_2

As a consequence of the requirement that the full state load modulation factor shall lie on the $dflin$-circle, the main amplifiers full state voltage phasor $U_M(1)$ can be deduced directly from the voltage and current relationships at the ports of the transmission line Z_1 (s. Fig. 2.1). The backoff voltage at the output of that transmission line (i.e. the common node) $U_{CN}(BO)$ follows from the definitions made in 2.1.5, $U_M(BO) = 1$ and $I_M(BO) = BO$, as

$$U_{CN}(BO) = cos(\phi) + j\,Z_1\,BO\,sin(\phi) \tag{2.115}$$

With $I_M(1) = 1$ and the fact that the voltage amplitude at the common node is proportional to the DPA's output amplitude and thus linear by definition, we get

$$|U_{CN}(1)| = |U_{CN}(BO)|\,\frac{1}{BO} = |U_M(1)\,cos(\phi) + j\,Z_1\,sin(\phi)| \tag{2.116}$$

With $|U_M(1)| = 1$, Eq. 2.115 can be solved for the imaginary part of $U_M(1)$, which equals the main amplifiers termation reactance $X_M(1)$

$$\mathfrak{Im}\{U_M(1)\} = \mathfrak{Im}\{Z_M(1)\} = X_M(1) = \frac{1 - \frac{1}{BO^2}}{2\,Z_1\,tan(\phi)} \tag{2.117}$$

The real part follows from $|U_M(1)| = 1$

$$\mathfrak{Re}\{U_M(1)\} = \mathfrak{Re}\{Z_M(1)\} = R_M(1) = \sqrt{1 - \mathfrak{Im}\{U_M(1)\}^2} \tag{2.118}$$

[25] All parameters that are not specified explicitly are equal to those used in the load modulation space examples shown in the introduction of section 2.3 (Figs. 2.19 - 2.21).

This is an important finding, since it demonstrates that, in case of a linear main amplitude drive function, the main amplifiers termination resistance (and thus its full state output voltage and power, as can be observed in Figs. 2.43 and 2.43 inside the area that meets boundary condition 4) is a sole function of Z_1 and BO. From $Z_M(1)$ the full state load modulation factor (Eq. 2.11) can also be deduced

$$\Gamma(1) = Z_M(1)\, A_{21} - A_{11} = (Z_M(1) - R_M(BO))\, A_{21} \tag{2.119}$$

Since the argument of A_{21} is a sole function of Z_1 and BO as well,

$$\angle A_{21} = \arctan(BO\, Z_1 \tan(\Theta)) \tag{2.120}$$

the same applies to the argument of $\Gamma(1)$

$$\angle\Gamma(1) = \arctan\left(\frac{\mathfrak{Im}\{Z_M(1)\}}{\mathfrak{Re}\{Z_M(1)\} - \frac{1}{BO}}\right) + \arctan(BO\, Z_1 \tan(\Theta)) \tag{2.121}$$

$\angle\Gamma(1)$ is an important measure, since the non-linear relative phase of the drive function is a source of drive function non-linearity that is present even in case the second linearity criterion is fulfilled (i.e. the main amplifier amplitude drive function is strictly linear). Finally, $\Gamma(1)$ provides a convenient way to express the center and radius of the $dflin$ circle[26]

$$M_{dflin} = \frac{|\Gamma(1)|}{2\cos(\angle\Gamma(1))} \qquad r_{dflin} = |M_{dflin}| \tag{2.122}$$

The relations derived above simplify the analysis and may provide some additional insights but they do not solve the actual problem of calculating the adapted Z_2 value directly as a function of Z_1 and Z_3, as required for the combiner design space analysis. A similar approach as in Eq. 2.115 could be used in order to find a closed form solution for Z_2, but unfortunately this results in a very clumsy 4^{th} order equation. Thus, in the following, we will again resort to a numerical solution in order to find the first $Z_2 > Z_1\, Z_3$ for which the output power $P(int)$ at the first intersection of the $dflin$ and equi-clip

[26] If $\Gamma(1)$ lies on the $dflin$ circle, it forms an isosceles triangle with M_{dflin}.

circles equals the targeted full state power[27]. With the adapted value of Z_2 being found, a design space analysis analogue to section 3.4 can be performed. In addition to the performance criteria introduced there, however, center frequency performance has to be taken into account now as well, since the assumption of ideal Doherty operation at center frequency has been dropped. Load modulation space analysis at center frequency is straightforward, as the corresponding full state load modulation factor can be specified easily. At center frequency, the c_M-limited iso-P circles derived in 2.3.2 simplify to the expressions given for the iso-c_M circles in Eqs. 2.82 and 2.83. With these, the center frequency load modulation factor follows as

$$\Gamma_{f0}(P) = -A_{11} - j\frac{|A_{21}|\sqrt{\frac{A_{11}}{A_{21}}}}{\sqrt{2P}} \tag{2.123}$$

Inserting the center frequency chain parameters of the combiner (Eqs. 2.28 and 2.32) gives

$$\Gamma_{f0}(P) = j\frac{Z_2}{Z_1 Z_3}\left(R_M(BO) - \sqrt{\frac{R_M(BO)}{2P}}\right) \tag{2.124}$$

For the symmetric case, we have $R_M(BO) = 2$ and $P(1) = 1$ and Eq. 2.124 reduces to

$$\Gamma_{f0}(1) = j\frac{Z_2}{Z_1 Z_3} \tag{2.125}$$

2.7.2 Class-B design space analysis with adapted Z_2

In order to assess the potential performance of a wideband Class-B DPA solution linearized by adapting Z_2 for $P(int) = P(1)$ at the band edges, we will resort to the combiner design space analysis that has already been used in previous sections. Apart from the adapted value of Z_2, the statements and definitions made in section 2.4 with regard to the Class-B combiner design

[27] The assumption that this is the only relevant solution has been backed up by an exhaustive numerical search over all possible solutions. This assumption is especially important for the Class-J case presented later, where otherwise the computing time required for an exhaustive search would become excessive.

space analysis in general will also apply to this section. However, there are some changes in the boundary conditions and performance criteria due to the adaption of Z_2, which shall be discussed briefly, before the actual results of the analysis are presented.

Boundary conditions

① For the combiner design space with adapted Z_2, the first boundary condition expresses whether or not **the adapted $\boldsymbol{Z_2 > Z_1 Z_3}$ exists, such that $\boldsymbol{P(int)}$ equals the targeted full state power** (i.e. $P(int) = 1$ for the symmetric case discussed in this section). It is set during the numeric Z_2 search if $P(int)$ remains $< P(1)$ throughout the relevant Z_2 range[28].

② The second boundary condition marks an area in which **the equiclip and $\boldsymbol{dflin}$ circles will not intersect for any $\boldsymbol{Z_2 > Z_1 Z_3}$**. This is also detected during the numeric Z_2 search.

The $c_M(BO) > c_P(BO)$ condition that was used in previous sections merges into boundary ① in case of the adapted Z_2, since the definition of boundary ① implies that $c_M(BO) < c_P(BO)$[29].

Performance and feasibilty criteria

Since the second linearity criterion (2.3.5) is enforced at the band edges by adapting the value of Z_2, the measures introduced in 2.4 in order to evaluate drive function non-linearity, $P(int)$ and $|\Gamma(int) - \Gamma(1)|$, must not be considered anymore[30]. Instead, center frequency performance has to be taken into account now, since the ideal Doherty operation at center frequency is no longer assumed.

[28] The relevant parameter range for Z_2 used during the exact search is dynamically adapted in order to reduce computation time, based on a coarse initial search. It is ensured that no relevant solution is missed.

[29] Due to the numeric nature of the calculation of Z_2, an independent definition of a boundary condition corresponding to the $c_M(BO) > c_P(BO)$ condition in previous sections seemed inappropriate, although a similar condition still exists, as can be observed from the results of the design space analysis.

[30] A drive function non-linearity criterion with regard to the the non-linear relative phase of the drive function could still be defined (see Eq. 2.121), but this was omitted because it would be strongly correlated to the power balance criterion already defined and would thus not add much further information.

Figure 2.48 shows the actual value of the adapted Z_2. The performance criteria, average efficiency for a 6.45 dB Rayleigh signal, full state efficiency, current and power balance, are illustrated in Figures 2.49 - 2.55 at band edges and center frequency, respectively. These criteria as well as the feasibility of the wideband load match $Z_L(f)$ are defined analogue to section 2.4. As pointed out in Eq. 2.118, the power balance at band edges is independent of Z_3, which is confirmed in Fig. 2.55. At center frequency, the power balance maintains a constant value of 1 by definition (2.1.5) and is therefore not shown explicitly.

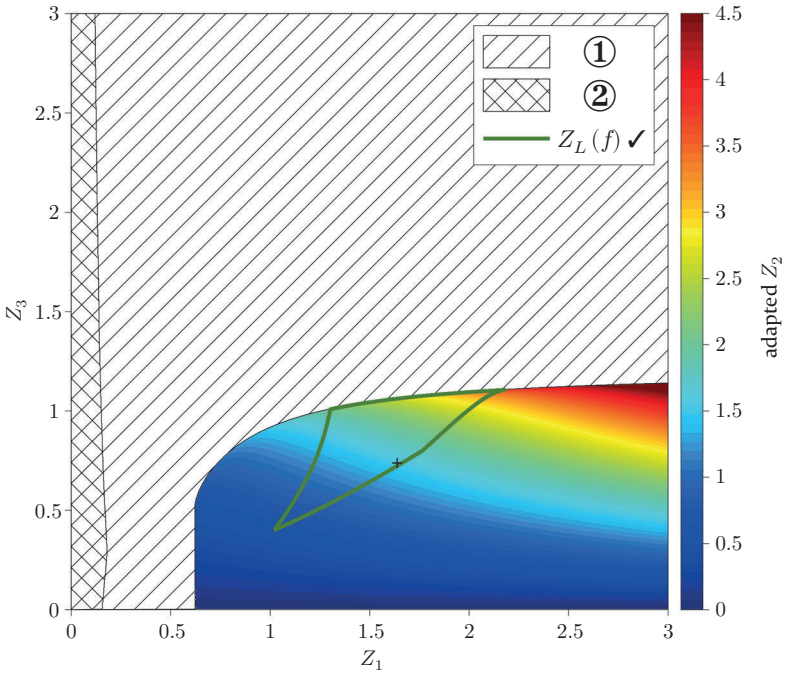

Figure 2.48: Value of the adapted Z_2 in $[Z_1, Z_3]$-space

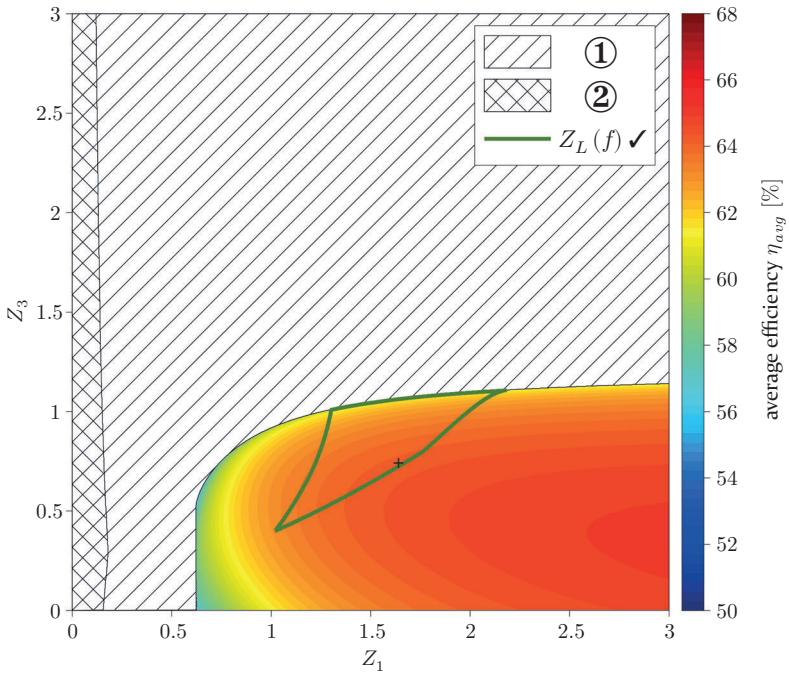

Figure 2.49: Average efficiency at band edges in $[Z_1, Z_3]$-space

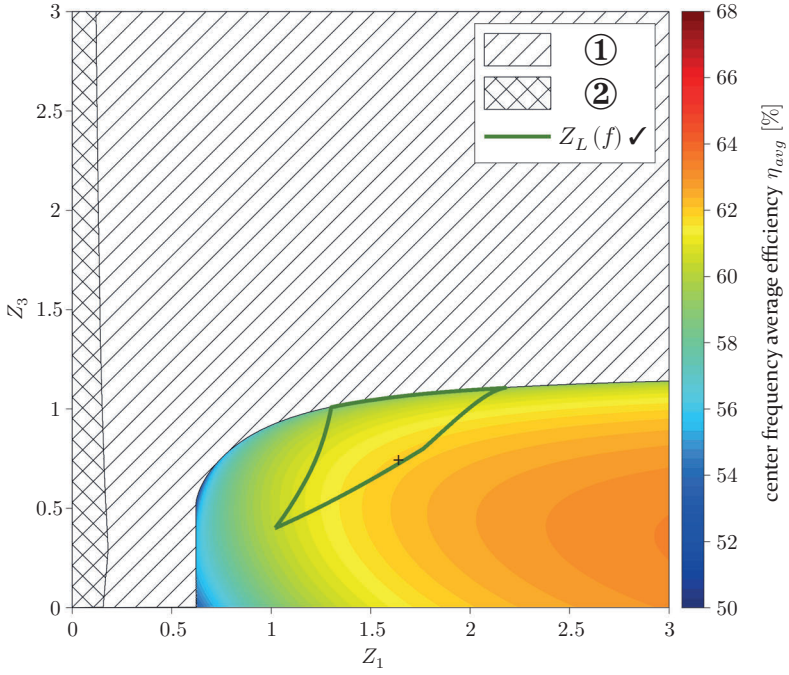

Figure 2.50: Average efficiency at center frequency in $[Z_1, Z_3]$-space

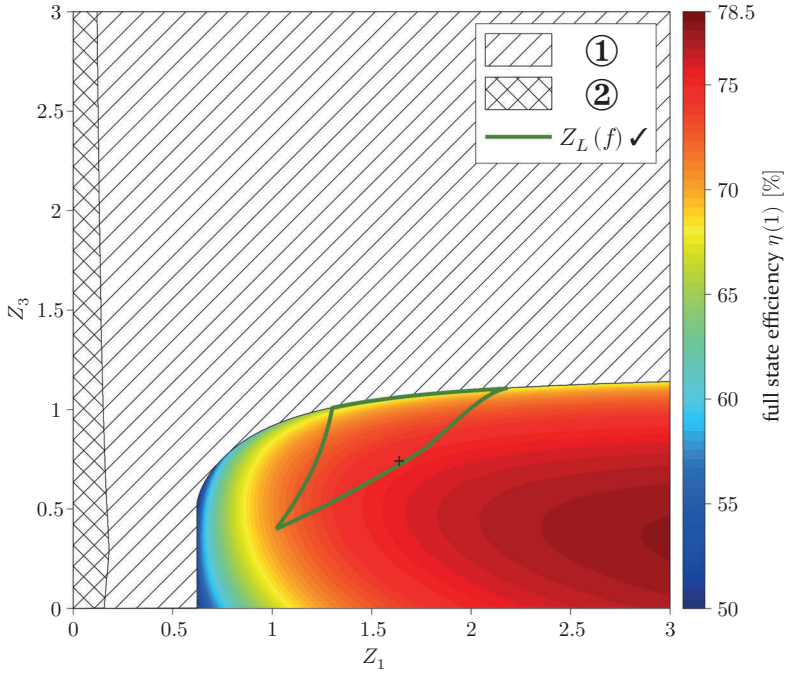

Figure 2.51: Full state efficiency at band edges in $[Z_1, Z_3]$-space

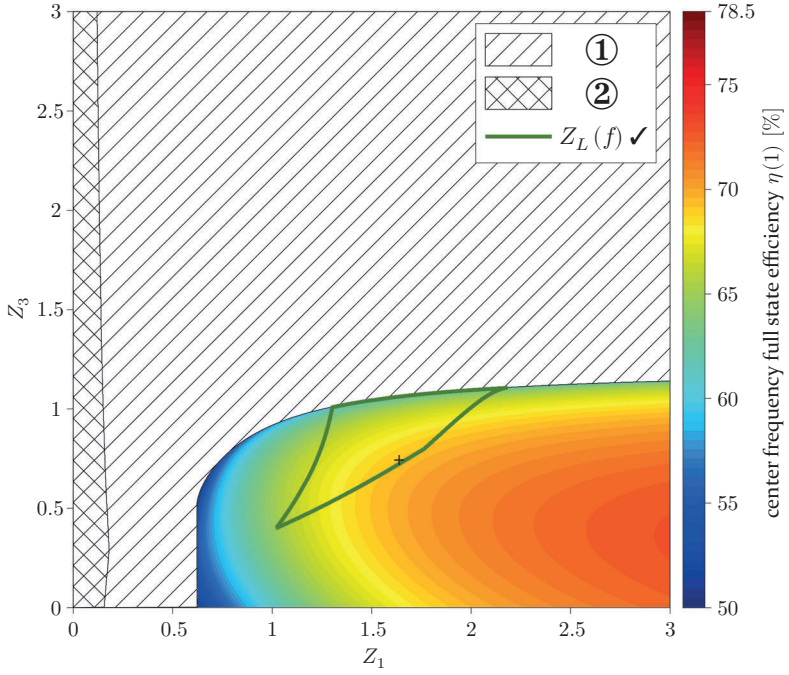

Figure 2.52: Full state efficiency at center frequency in $[Z_1, Z_3]$-space

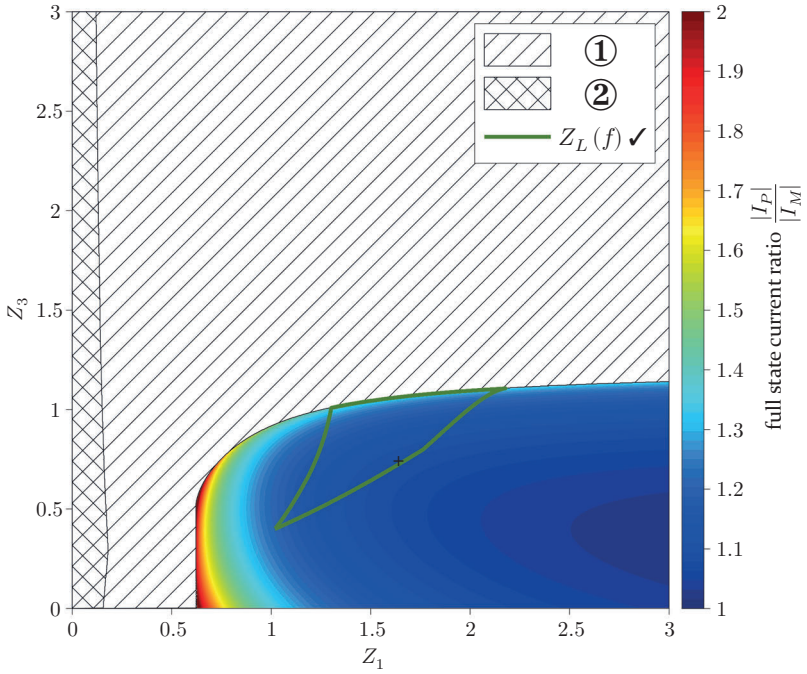

Figure 2.53: Full state current ratio at band edges in $[Z_1, Z_3]$-space

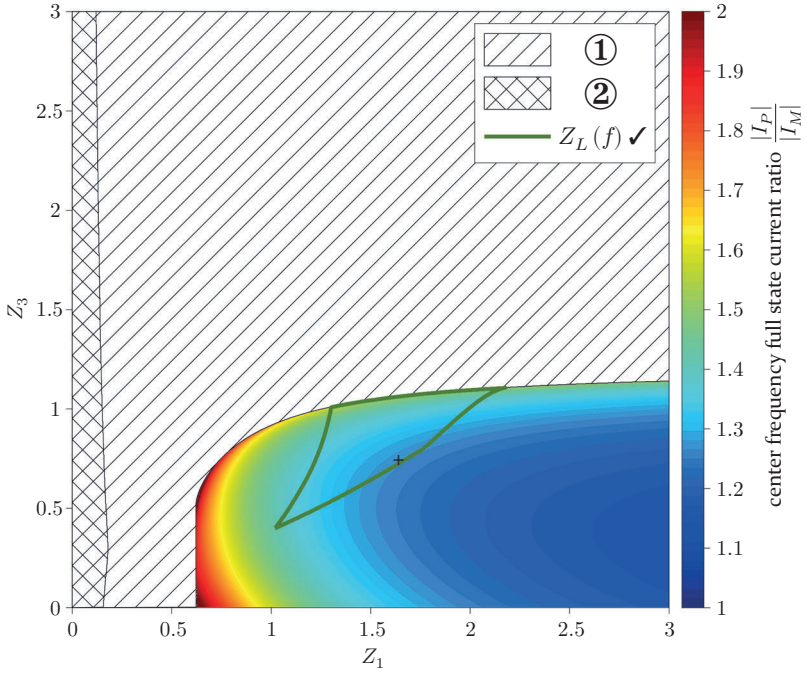

Figure 2.54: Full state current ratio at center frequency in $[Z_1, Z_3]$-space

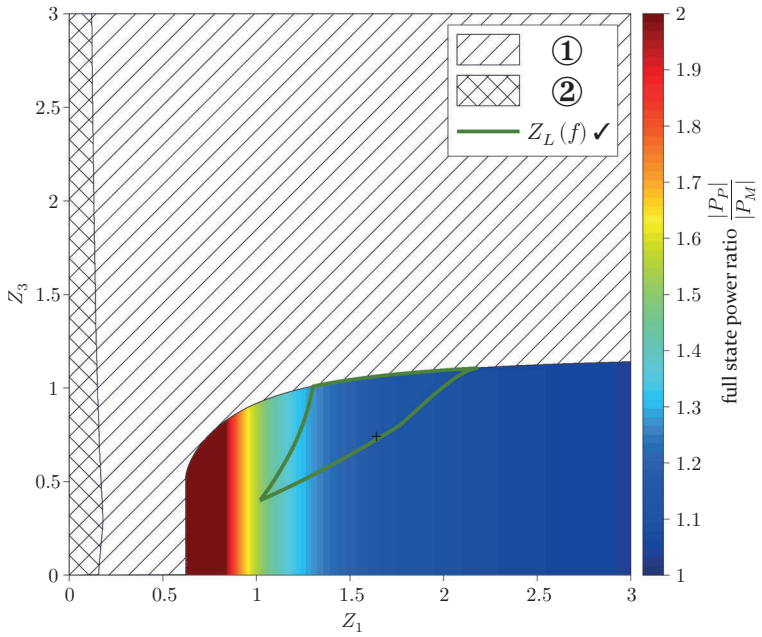

Figure 2.55: Full state power ratio at band edges in $[Z_1, Z_3]$-space

Conclusion

The results of the design space analysis confirm that the Class-B solution with adapted Z_2 does what it is supposed to do: It enforces the second linearity criterion for the price of reduced center frequency performance due to the peak amplifier core not being fully saturated at full state output power. As in previous sections, an exemplary choice of optimum combiner parameters, summarized in Table 2.3, is made in order to simplify comparison with the other wideband DPA variants discussed in this chapter. The corresponding load modulation space representations were given in Figures 2.46 and 2.47. Figure 2.56 shows the drive functions in linear amplitude domain. We see that, in terms of efficiency, the adapted Z_2 solution is the least satisfying of the solutions discussed so far. As already observed in the Class-J case, the usage of a linear drive function itself leads to lower average efficiency compared to the Class-B case with $Z_2 = Z_1\,Z_3$, since the efficiency boost due to the non-linear 'quasi-outphasing' mode at high powers is lost. At the band edges, the adapted Z_2 solution delivers a slightly higher average efficiency than the Class-J solution with $Z_2 = Z_1\,Z_3$ while at the same time providing better drive function linearity. On the other hand, the loss of about 9.3 % in full state

efficiency at center frequency is indeed painful[31]. With regard to the current balance, the adapted Z_2 solution also performs worse than the $Z_2 = Z_1\,Z_3$ solutions, since, at center frequency, the unsaturated voltage amplitude at the peak amplifier core is compensated by a higher current amplitude in order to achieve equal full state output power. Nevertheless, it has become clear that the adaption of Z_2 provides a generic way to enforce linearity of the main amplitude drive function. In the next and final step, this principle will be applied to the Class-J case.

	Z_1	Z_2	Z_3	$\eta(1)$	η_{avg}	$\lvert\Gamma(int)-\Gamma(1)\rvert$	$P(int)$	$\frac{\lvert I_P\rvert}{\lvert I_M\rvert}$	$\frac{P_P}{P_M}$
Class-B $Z_2 = Z_{2opt}$ center frequency	1.65	1.55	0.74	69.2	61.9	(-0.27)	(1.61)	1.27	1
Class-B $Z_2 = Z_{2opt}$ band edge	1.65	1.55	0.74	75.0	64.2	0	1	1.09	1.16

Table 2.3: Summary of exemplary results for the Class-B case with $Z_2 = Z_{2opt}$

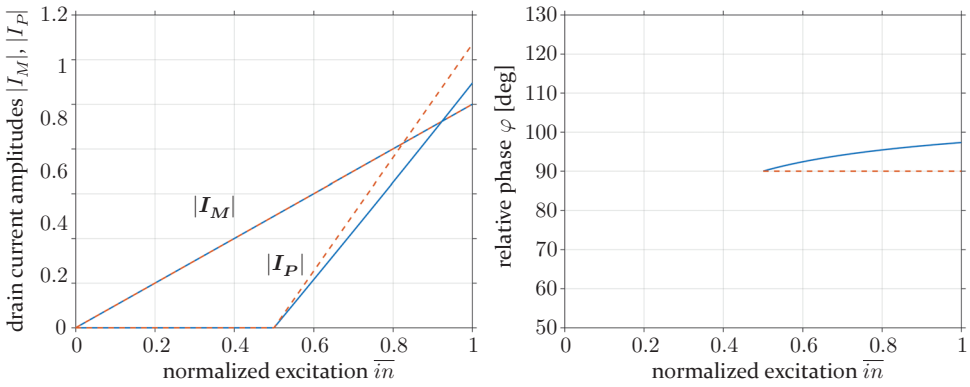

Figure 2.56: Band edge (blue) and center frequency (red dotted) drive functions vs. normalized excitation $\overline{in}$

[31] Although the full state efficiency is not the most critical performance parameter in base station PAs, because the actual PAPR is usually much higher than 6.45 dB when fluctuating network load conditions are taken into consideration.

2.7.3 Class-J design space analysis with adapted Z_2

Unfortunately, the relations derived previously for the Class-B load modulation space with adapted Z_2 (Eqs. 2.115 - 2.118) do not apply to the Class-J case[32]. For the Class-J case, $U_M(BO)$ is complex, thus Eq. 2.116 becomes

$$\left|\left(\frac{1}{BO}+jZ_{i,M}\cot(\Theta)\right)\cos(\Theta)+jZ_1\sin(\Theta)\right| = |U_M(1)\cos(\Theta)+jZ_1\sin(\Theta)| \tag{2.126}$$

Solving this equation is not as straightforward as for the Class-B case, since the assumption $|U_M(1)|=1$ doesn't hold anymore. As a consequence of linearity, the full state clipping factor $c_M(1)$ is still known and constant throughout frequency, but due to the multi-harmonic nature of the voltage waveform, it cannot be easily mapped back to the fundamental voltage amplitude. The results of the design space analysis indicate that $U_M(1)$ in Class-J is still independent of Z_2 and Z_3, but is now also a function of $Z_{i,M}$. For the following Class-J design space analysis, the identification of the adapted Z_2 value as well as load modulation space analysis in general are done numerically. Class-J load modulation space analysis is based on the same principles and algorithms that were used in section 2.6.

Boundary conditions

Boundary conditions for the Class-J case with adapted Z_2 are defined analog to the Class-B case.

① The first boundary condition expresses whether or not **the adapted $\boldsymbol{Z_2 > Z_1}$ $\boldsymbol{Z_3}$ exists, such that $\boldsymbol{P(int)}$ equals the targeted full state power**. It is set during the numeric Z_2 search if $P(int)$ remains $< P(1)$ throughout the relevant Z_2 range. For the Class-J case, one exception from this definition occurs, which will be treated separately as boundary condition ④.

② The second boundary condition designates an area in which **the equi-clip and $\boldsymbol{dflin}$ circles will not intersect for any $\boldsymbol{Z_2 > Z_1}$ $\boldsymbol{Z_3}$**. This is also detected during the numeric Z_2 search.

[32] The relations regarding the center frequency load modulation factor (Eqs. 2.123 - 2.125) do apply to the Class-J case as well.

③ The third boundary condition designates an area in which the adapted Z_2 solution exists, but **full state power balance at the band edges is negative**. Namely, the main amplifier core sinks power in this region, which is obviously not useful for the design of a practical DPA.

④ In Class-J cases with large values of $Z_{i,M}$ an area in the combiner design space is observed in which $P(int)$ becomes larger than the targeted full state power $P(1)$ for $Z_2 = Z_1\,Z_3$. This case has already been identified in section 2.6 and led to the definition of boundary conditions ④ and ⑤ in 2.6.1. For the adapted Z_2 solution discussed here, it necessitates that **a $\boldsymbol{Z_2 < Z_1\,Z_3}$ must be chosen in order to fulfill the $\boldsymbol{P(int) = P(1)}$ requirement** in that area.

Performance and feasibility criteria

Figure 2.57 shows the actual value of the adapted Z_2 in $[Z_1, Z_3]$-space for a discrete set of backoff reactance parameters $Z_{i,M} \in \{1, 2, 3\}$ and $Z_{i,P} \in \{0, 1\}$, using the same method of illustrating Class-J combiner design space results as introduced in section 2.6. We see that, with increasing $Z_{i,P}$, the combiner parameter range in which a solution for the adapted Z_2 exists becomes quite narrow. At the same time, due to the increased transformation ratio in the peak path, the feasibility of the wideband load match $Z_L\,(\Theta)$ is significantly impaired. With increasing $Z_{i,M}$, the feasible $Z_L\,(\Theta)$ region barely extends into the region of good performance, especially at $Z_{i,P} = 1$. Contrary to the Class-J case with $Z_2 = Z_1\,Z_3$, the peak amplifier termination reactance parameter $Z_{i,P}$ now also affects the wideband load match $Z_L\,(\Theta)$ via its influence on the value of the adapted Z_2.

Figures 2.58 - 2.62 represent the performance parameters, including center frequency performance parameters, as introduced in previous sections. In section 2.7.1 it was shown that, for the Class-B case, the main amplifier core's full state power is a function of Z_1 and BO, but is independent of Z_2 and Z_3. Figure 2.62 reveals that this statement applies to the Class-J case as well. In Figure 2.62 we also notice a pole in the full state power balance function, which gave rise to the definition of boundary condition ③. On the left side of this pole, the main amplifier cores full state power becomes negative.

Conclusion

When comparing the efficiency plots in Figures 2.58 and 2.59, we see that the degradation of center frequency efficiency, which is characteristic for the adapted Z_2 solution, reduces as $Z_{i,M}$ is increased. Around $Z_{i,M} = 2$ center frequency and band edge efficiencies become well balanced for $Z_1 > 1.5$. So far, this is a result that was expected and hoped for. But unfortunately, the results also show that, for the Class-J case, the adapted Z_2 solution produces a quite infeasible wideband load match $Z_L(\Theta)$, especially if a $Z_{i,P} > 0$ is introduced. Within the range of feasible wideband load match approximations, the theoretical potential of applying the adapted Z_2 solution to the Class-J wideband DPA cannot be realized.

An exemplary optimum set of combiner parameters for the Class-J DPA with adapted Z_2 is chosen analog to the cases discussed previously. The results for this solution are summarized in Table 2.4. In order to even enable a solution, $Z_{i,P}$ had to be kept at zero. This is a major restriction, since it contradicts the most important goal of the Class-J solution, which is to allow for a practical wideband termination of the second harmonic frequency component. But even if this shortcoming was deemed acceptable, we see that the efficiency results are not optimal and, more importantly, the full state power ratio at the band edges is prohibitively high.

	Z_1	Z_2	Z_3	$\eta(1)$	η_{avg}	$\lvert\Gamma(int)-\Gamma(1)\rvert$	$P(int)$	$\frac{\lvert I_P\rvert}{\lvert I_M\rvert}$	$\frac{P_P}{P_M}$
Class-J, $Z_{i,M}=2$, $Z_{i,P}=0$, $Z_2=Z_{2opt}$ center frequency	1.07	0.81	0.72	74.31	63.79	(-0.12)	(1.24)	1.11	1
Class-J, $Z_{i,M}=2$, $Z_{i,P}=0$, $Z_2=Z_{2opt}$ band edges	1.07	0.81	0.72	69.50	61.78	0	1	1.26	1.63

Table 2.4: Summary of exemplary results for the Class-J case with $Z_2 = Z_{2opt}$

Eventually, it has to be acknowledged that linearizing the wideband Class-J DPA by adapting Z_2 does not work out as well as initially anticipated. Although the analysis shows that for $Z_{i,P} = 0$ and $Z_1 > 1.5$ this combination of wideband techniques would meet the expectations associated with it, its potential cannot be realized due to the infeasibility of an appropriate wideband load match approximation. A badly approximated load match, however, would not only impair load modulation performance, but also result in poor backoff performance and is therefore unacceptable.

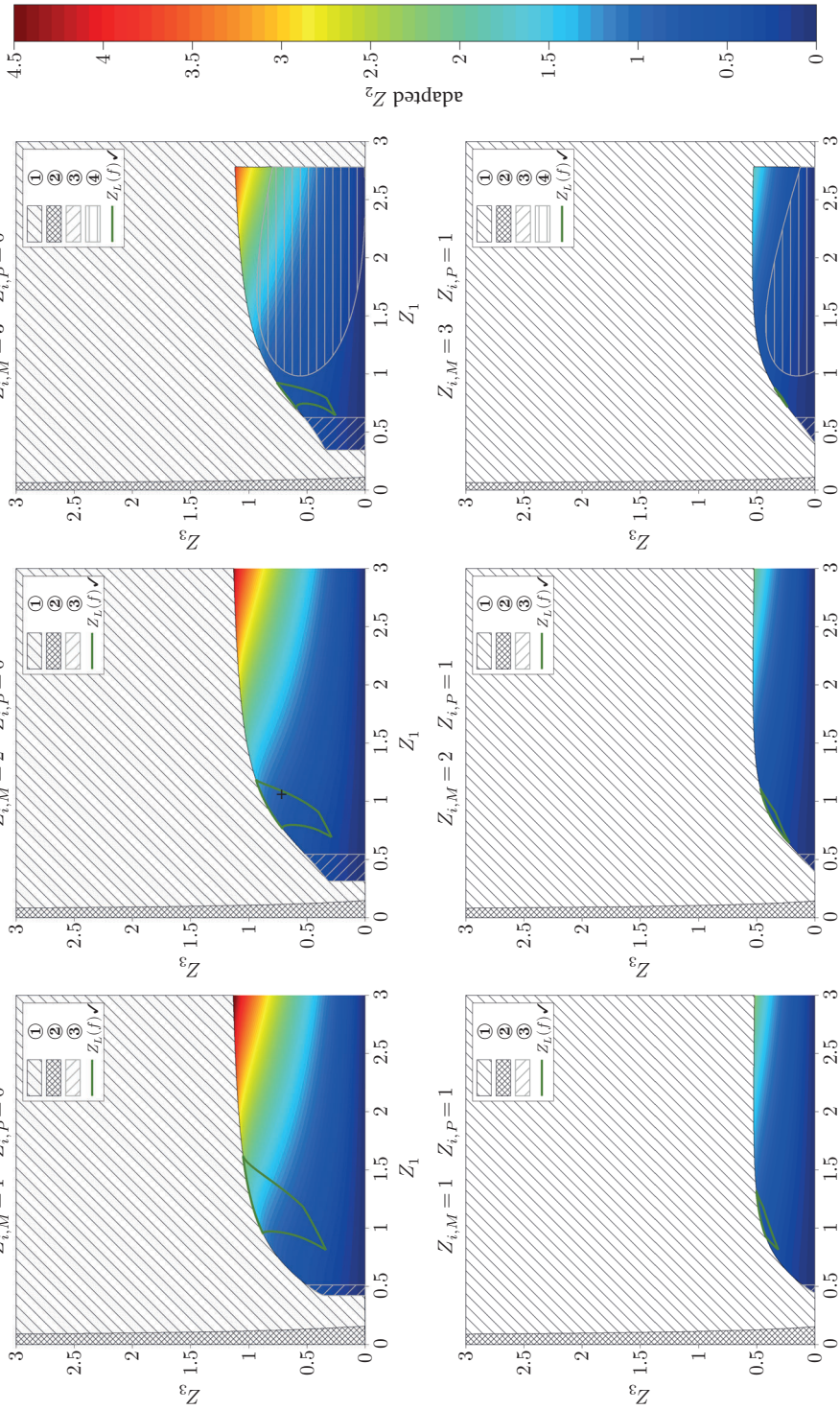

Figure 2.57: Value of the adapted Z_2 for various backoff reactance parameters $Z_{i,M}$ and $Z_{i,P}$

Figure 2.58: Average efficiency at band edges for various backoff reactance parameters $Z_{i,M}$ and $Z_{i,P}$

Figure 2.59: Average efficiency at center frequency for various backoff reactance parameters $Z_{i,M}$ and $Z_{i,P}$

Figure 2.60: Current balance at band edges for various backoff reactance parameters $Z_{i,M}$ and $Z_{i,P}$

Figure 2.61: Current balance at center frequency for various backoff reactance parameters $Z_{i,M}$ and $Z_{i,P}$

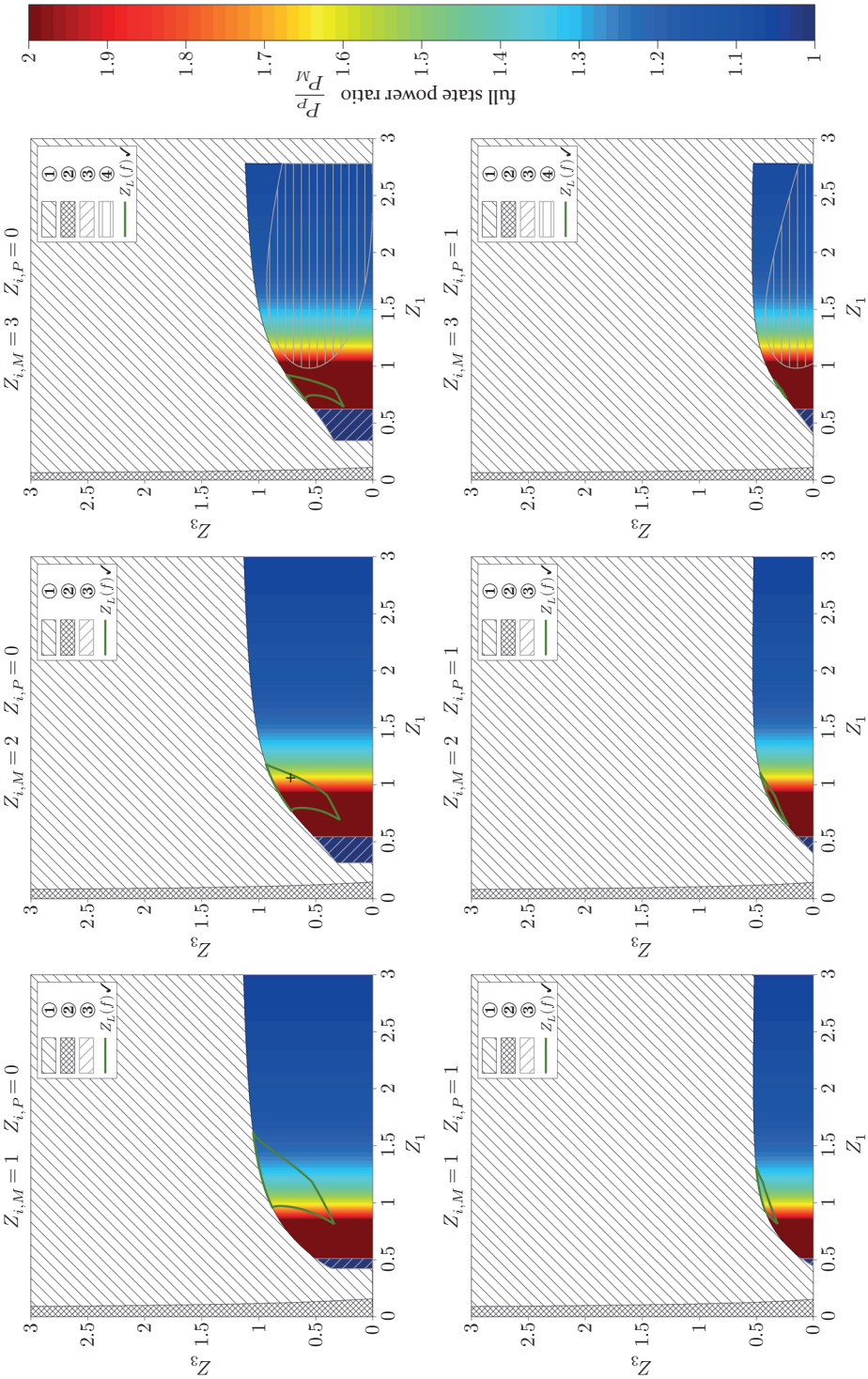

Figure 2.62: Power balance at band edges for various backoff reactance parameters $Z_{i,M}$ and $Z_{i,P}$

2.8 Summary and Conclusion

On the previous pages a method for the analysis of the wideband active load modulation problem has been established which is genuinely able to provide the level of insight that has been missing in this field. To conclude the chapter, we will briefly retrace the ideas upon which the load modulation space analysis is built, point out the novelty of various elements in the analysis and recapitulate the advantages that come along with them. Finally, the results gained from the design space analysis of the wideband DPA approaches discussed in sections 2.4 - 2.7 will be compared and practical recommendations for the design of an actual wideband DPA will be derived.

2.8.1 Novelty and advantage of the proposed analysis

The **load modulation space analysis** proposed in this chapter is based on the finding that, for a given combiner topology, the virtual impedances at the individual amplifier cores of a Doherty PA solely depend on the ratio between the current vectors sourced by the amplifier cores, which has been referred to as the complex load modulation factor. A normalized, linear excitation has then been assumed and a clipping operator has been applied to the resulting voltage and current waveforms in order to create the voltage saturation conditions which are inherent to active load modulation PA concepts like the Doherty or Chireix architectures. Based on these rather simple operations, it was possible to reduce the active load modulation concept from a four dimensional problem (two complex input currents) to a two dimensional one (one complex load modulation factor). The introduction of a clipping operator enabled us to map the complex load modulation factor directly to the PA's output power and efficiency. To the best of the author's knowledge, the resulting representation of the PA's output parameters in complex load modulation space is completely new to the field and proves to be a key element on the way towards an intuitive understanding of wideband active load modulation. In the course of further analysis of the load modulation space representation, characteristic objects such as the equi-clip circle, iso-P contours and the $dflin$ circle were identified. Under the assumption of Class-B operating conditions, which is common to almost all previous works on Doherty PAs, these objects have been deduced analytically and a complete mathematical description has been provided in section 2.3. The insights gained from the analysis of the Class-B load modulation space have then been transferred to the Class-J case, based on a numeric evaluation of the multi-harmonic clipping factors. This is a crucial

step towards practical wideband DPAs, since Class-B operating conditions are inherently narrowband and their usage in the analysis of wideband DPAs, as commonly found in literature, is therefore inconsistent and questionable.

The clipping operator does not only allow for the expression of the PA's output parameters as functions of the complex load modulation factor, it also allows to map the load modulation factor back to the source current vectors, as stated in equation 2.90. The source current vectors, in turn, correspond to the input drive functions of the amplifier. Thus, the load modulation space analysis established in this work provides the missing link between a DPA's input drive functions and its output parameters. The key advantage of the load modulation space representation is that it creates an intuitive understanding of the crucial role of the drive functions in a wideband active load modulation RFPA. In the context of **drive function linearity**, it has been found that the assumption of a main amplitude function that proceeds linearly from the low power region into the load modulation region, termed 1st linearity criterion in this work, maps to the $dflin$-circle in complex load modulation space. It becomes obvious at this point that the classic drive function present in an analogue DPA[33] is from the beginning unfit to fulfill this condition. Thus, a DPA limited to the classic drive function generally cannot achieve optimum load modulation conditions throughout an extended bandwidth.

Even more important, it has been found that the maximum available power in linear Doherty mode, which occurs when the linear drive function hits the equi-clip condition and which is usually lower than the targeted full state power, is not equivalent to the maximum power available in the load modulation space. If the drive function is not restricted to the linear drive function circle but allowed to move further on the equi-clip circle after intersecting it, which corresponds to a 'quasi-outphasing' mode to the effect that voltage saturation is maintained at both amplifier cores simultaneously, it is indeed possible to maintain constant full state power throughout a largely extended bandwidth. To the best of the authors knowledge, this is the first work that clearly demonstrated the existence of a **transition between the linear Doherty mode and a less linear 'quasi-outphasing' mode** in the detuned DPA in amplitude domain. A continuity between such modes has been described before in a patent by Richard Hellberg [36] and subsequent works at Chalmers University [39], [41], but these works referred to frequency dependent mode transitions as a result of the frequency-dependence of the combiner parameters. They did not further elaborate on the characteristics of

[33] i.e. a linear amplitude function with a constant relative phase, mapping to a line in complex load modulation space...

a mixed-mode operation of the detuned DPA and the consequences this has on the drive functions.

Another element newly introduced to the analysis of wideband active load modulation PAs is the **optimum wideband load match**. Analytic expressions have been derived for the frequency response of the load impedance connected to the common node of the DPA such that the termination impedance at the main amplifier core at backoff maintains its optimum value throughout bandwidth. The optimum wideband load match $Z_L(\Theta)$, which has been derived for Class-B as well as for Class-J termination conditions of the main amplifier core, has the advantage that it implicitly sets the performance in the backoff region to its optimum. In terms of analysis, this means that we can focus on the assessment of performance under load modulation and must not re-evaluate backoff performance whenever the combiner parameters are modified. In terms of practical wideband DPA design, the optimum wideband load match provides a way to significantly improve wideband performance, which is critically dependent on backoff performance, under the precondition that the quasi-left handed approximation of the ideal wideband load match is feasible. It has been demonstrated that the approximation based on a multi-section transmission line transformer is indeed feasible in many cases. Thus, the limitation to wideband resistive loads, which is commonly found in literature and which, by the way, require the same kind of multi-section transmission line transforms that could also be used to well approximate the optimum wideband load match, is an unnecessary waste of potential wideband performance[34]. However, it should be pointed out that the methods of analysis introduced in this chapter are not restricted to combiner topologies with optimum wideband load match. They can be applied to any other combiner topology, but then performance at backoff must be assessed as well. Likewise, the findings regarding drive function linearity and the transition between the linear Doherty mode and a non-linear 'quasi-outphasing' mode are not limited to combiner circuits that apply the optimum wideband load match.

A major goal of the presented load modulation space analysis is that it allows us to define evaluation criteria which are specific to a given combiner circuit, represented by its chain parameters, and do not depend on the choice of an actual drive function. As such, the load modulation space analysis provides an ideal basis for a **combiner design space analysis**. The design

[34] Although the wideband resistive load may come close to the ideal wideband load match at a certain point in the combiner design space, it does not seem reasonable to limit the analysis to this point.

space analysis enables us to fully assess the potential performance of a certain combiner topology, optimize the design parameters for a given application or compare different combiner topologies with each other. Using a combiner topology based on three $\lambda/4$ transmission lines and a wideband optimum load match, the combiner design space analysis was first introduced for the Class-B design space and was then transferred to the Class-J case. To the best of the author's knowledge, this work is also the first one to introduce Class-J termination conditions to wideband Doherty PA design and systematically analyse the potential and feasibility of such a solution. To give a thorough analysis of Class-J operation in wideband DPAs was the primary objective of this work and the fact that this seemingly obvious step has not been made by others before clearly indicates the novelty and value of the proposed methods of analysis.

2.8.2 Comparison of the discussed wideband DPA solutions

In sections 2.4, 2.6 and 2.7 the potential performance of various wideband DPA approaches has been assessed by means of a combiner design space analysis. The results are summarized in Table 2.5. Classic Doherty operation and thus ideal Doherty performance occurs at center frequency for $Z_2 = Z_1 Z_3$. It has been shown that, as the combiner is detuned to 50 % rel. BW, the maximum available output power of the linear Doherty mode reduces to about 60 - 70 % of the targeted full state power, under the assumption of a sinusoidal drain voltage waveform (Class-B). If the drive function was able to follow the subsequent transition to a 'quasi-outphasing' mode instantly, the targeted full state power could be maintained throughout the entire frequency range and the non-linear 'quasi-outphasing mode' in the detuned case would provide even higher instantaneous efficiencies than the linear Doherty mode at center frequency. The downside of this approach is that it contains two assumptions which are both incorrect. Due to its bandwidth limitations, a technically feasible drive function will not be able to follow the transition from the linear Doherty mode to the quasi-outphasing mode instantly. Instead, a softer transition between these modes must be chosen in order to reach the targeted full state power within given boundaries on the bandspread of the PA's input signals. To find a drive function that fulfills these requirements while at the same time maintaining linearity at the PA's output and preserving as much efficiency as possible is a task for advanced digital predistortion of dual-input DPAs. Novel approaches that address this problem (e.g. dynamic drive functions) are the subject of ongoing research.

The second invalid assumption was that of a wideband Class-B operation (i.e. sinusoidal drain voltage waveforms throughout the entire bandwidth), which would require a wideband short circuit of the higher harmonic components at the active devices' intrinsic current generator planes and is thus physically impossible. In an attempt to address the problem of providing valid multi-harmonic termination conditions over an extended bandwidth, the author introduced continuous complex termination conditions, known as Class-J, to the analysis of the wideband DPA. By providing the appropriate wideband load match $Z_L(\Theta)$ at the common node of the combiner, optimum Class-J conditions were enforced in the low power region, prior to the onset of active load modulation. This is in itself an important step towards better wideband DPA performance, since the low-power region is crucial to overall performance, but it also lays the foundation for the analysis of Class-J-type operation modes under active load modulation. Further analysis revealed that, although it

	Z_1	Z_2	Z_3	$\eta(1)$	η_{avg}	$\lvert\Gamma(int)-\Gamma(1)\rvert$	$P(int)$	$\frac{\lvert I_P\rvert}{\lvert I_M\rvert}$	$\frac{P_P}{P_M}$
Class-B $Z_2 = Z_1 Z_3$ center frequency	1.90	2.76	1.45	78.54	65.23	0	1	1	1
Class-B $Z_2 = Z_1 Z_3$ band edge	1.90	2.76	1.45	78.17	67.05	0.36	0.64	0.84	0.84
Class-J, $Z_{i,M} = 2$, $Z_{i,P} = 1$, $Z_2 = Z_1 Z_3$ center frequency	1.07	0.87	0.81	78.54	65.23	0	1	1	1
Class-J, $Z_{i,M} = 2$, $Z_{i,P} = 1$, $Z_2 = Z_1 Z_3$ band edge	1.07	0.87	0.81	71.29	63.52	0.20	0.76	0.99	1.06
Class-B $Z_2 = Z_{2opt}$ center frequency	1.65	1.55	0.74	69.2	61.9	0 (-0.27)	1 (1.61)	1.27	1
Class-B $Z_2 = Z_{2opt}$ band edge	1.65	1.55	0.74	75.0	64.2	0	1	1.09	1.16
Class-J, $Z_{i,M} = 2$, $Z_{i,P} = 0$, $Z_2 = Z_{2opt}$ center frequency	1.07	0.81	0.72	74.31	63.79	0 (-0.12)	1 (1.24)	1.11	1
Class-J, $Z_{i,M} = 2$, $Z_{i,P} = 0$, $Z_2 = Z_{2opt}$ band edge	1.07	0.81	0.72	69.50	61.78	0	1	1.26	1.63

Table 2.5: Comparison of exemplary results for the wideband DPA approaches discussed in this chapter

is not possible to maintain optimum Class-J termination conditions at both amplifier cores simultaneously under load modulation, a sufficiently high level of efficiency can be maintained throughout the load modulation region. Most interestingly, the linear Doherty range is extended due to the Class-J termination, which means that the drive function non-linearity problem becomes less prominent. Full state current and power balance is also improved. Thus, the Class-J approach brings us much closer to a practical wideband DPA solution.

Finally, the question if the problem of drive function non-linearity could be solved solely by means of combiner design has been further addressed. It has been shown that by dropping the $Z_2 = Z_1 Z_3$ requirement and allowing for larger values of Z_2, the combiner transformation ratio can be adapted in such a way that the maximum output power of the linear Doherty mode at the band edges equals the targeted full state power. Since the $Z_2 = Z_1 Z_3$ requirement is a direct result of the equi-clip condition at center frequency, increasing Z_2, on the other hand, leads to current imbalance and significantly reduced full state efficiency at center frequency. For the Class-B case, the resulting drop in overall performance might just be acceptable. However, contrary to initial expectations, we had to learn that this approach is not practical at all for the Class-J case.

In conclusion, the most promising approach for a practical implementation of a wideband DPA demonstrator seems to be the Class-J solution with $Z_2 = Z_1 Z_3$. Since the feasibility of a potential Class-J DPA has always been a focus of this work and the analysis revealed that such a solution is indeed promising, it strongly suggests itself to verify the theoretical results in practice. Although asymmetric DPA solutions were not treated explicitly in this chapter, it has been found that the Class-J solution with $Z_2 = Z_1 Z_3$ is, in theory, compatible with moderate and even high degrees of asymmetry [35]. This is an important feature in practical cellular base station applications, where the 6 dB backoff ratio of a symmetric DPA is usually deemed too small. Furthermore, the remaining drive function non-linearity due to the Doherty-Outphasing transition may even be regarded a desirable feature for a demonstrator circuit. It opens up yet another opportunity to experimentally verify the results of the proposed analysis and provides a testbed for further research on the signal processing side, which then eventually answers the important question of whether or not the kind of non-linearity encountered in a wideband DPA is compatible with instantaneous wideband PA operation.

[35] Theoretically up to $R_M(BO) \leq 3$, corresponding to a backoff ratio of about 10 dB.

3 Design of a wideband active load modulation RFPA demonstrator

3.1 Choice of active devices

For the sake of convenience, most of the theoretical analysis presented in the previous chapter referred to symmetric DPA configurations ($I_P(1) = I_M(1) = 1$). In practical applications of the DPA, however, it is usually favourable to use asymmetric configurations. Based on the normalization introduced in 2.1.6, which applies to symmetric as well as asymmetric configurations, the fundamental drain voltages and currents in the load modulation region for the tuned combiner can be expressed as functions of output power

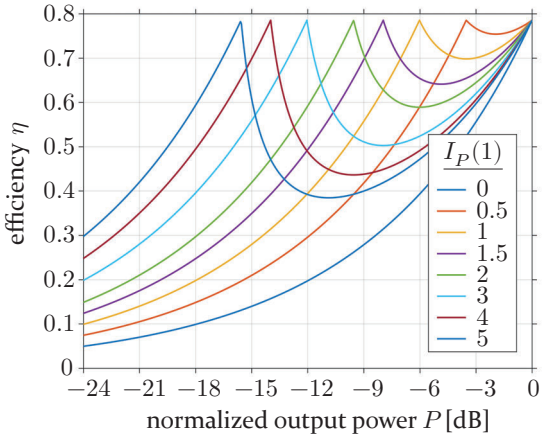

Figure 3.1: Instantaneous efficiency vs. output power backoff in an ideal, tuned, DPA for various full state current ratios

$$U_M(P) = 1 \qquad I_M(P) = \sqrt{2\,PBO} \tag{3.1}$$

$$U_P(P) = \sqrt{2\,PBO} \qquad I_P(P) = \sqrt{\frac{2\,P}{BO}} - 1 \tag{3.2}$$

with the parameter BO (indirectly) representing the degree of asymmetry. As established in 2.1.6, BO denotes the onset point of load modulation in amplitude domain and is linked to the full state current ratio

$$\frac{I_P(1)}{I_M(1)} = I_P(1) = \frac{1}{BO} - 1 \tag{3.3}$$

The instantaneous efficiency in the load modulation region as a function of output power follows from Eqs. 3.1 and 3.2 as

$$\eta_{LM}(P) = \frac{P}{P_{DC}(P)} = \frac{P}{\frac{2}{\pi}\left(I_M(P) + I_P(P)\right)} = \frac{P}{\frac{2}{\pi}\left(\sqrt{2P}\left(\sqrt{BO} + \sqrt{\frac{1}{BO}}\right) - 1\right)} \tag{3.4}$$

For the low power region, prior to the onset of load modulation, a Class-B efficiency slope $\eta_{BO}(P) = \frac{\pi}{4}\sqrt{\frac{P}{P(BO)}}$ can be assumed. Figure 3.1. illustrates the instantaneous efficiency characteristics of the ideal, tuned DPA for various full state current ratios $I_P(1)$. Based on the instantaneous efficiency characteristic and the signals probability density function $PDF(P)$, the average efficiency can be calculated for any given signal

$$\eta_{avg} = \frac{\int_0^{\frac{1}{2BO}} PDF(P)\, P \mathrm{d}P}{\int_0^{\frac{1}{2}BO} PDF(P)\, \frac{P}{\eta_{BO}(P)}\, \mathrm{d}P + \int_{\frac{1}{2}BO}^{\frac{1}{2BO}} PDF(P)\, \frac{P}{\eta_{LM}(P)}\, \mathrm{d}P} \tag{3.5}$$

Figure 3.2 shows the average efficiency as a function of the full state current ratio for Rayleigh-distributed signals with various PAPRs and thus allows to identify the optimum degree of asymmetry for a given PAPR. Cellular BTS make use of advanced crest factor reduction techniques, which limit the PAPR of the TX signal itself to 7.5 - 8.5 dB. This would result in an optimum full state current ratio of around 1 : 1.5. In actual application scenarios, however, the BTS doesn't operate at full capacity most of the time, which further increases the demand for higher backoff efficiency. Although other techniques to accommodate fluctuating network loads are available supplementary to active load modulation (e.g. drain bias adaption), it seems desirable to further increase the full state current ratio of the DPA up to 1 : 2. On the other hand, it has to be kept in mind that higher degrees of asymmetry necessitate higher

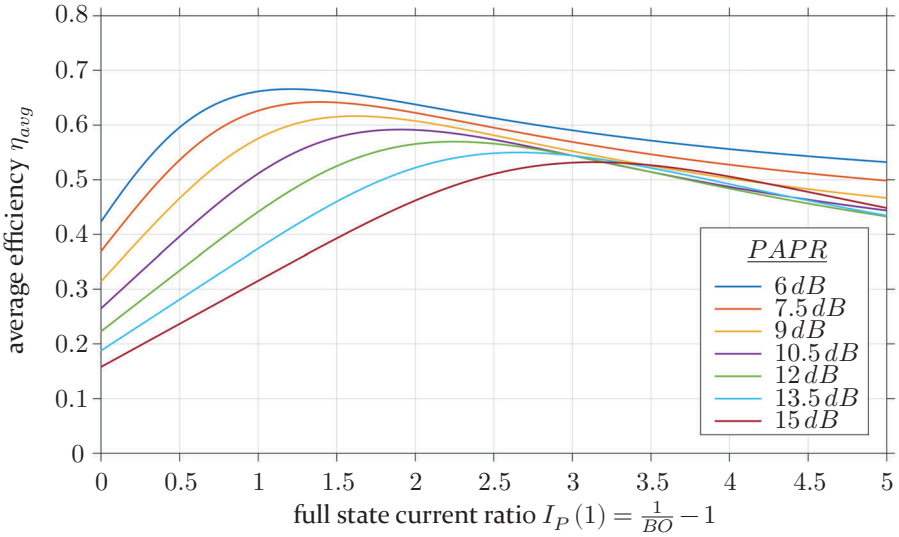

Figure 3.2: Average efficiency of the ideal DPA vs. asymmetry for Rayleigh-distributed signals with various PAPRs

transformation ratios in the combiner[1] and thus compromise bandwidth. To sum up this short discussion on asymmetry, the wideband DPA demonstrator described in this chapter should feature a full state current ratio of at least 1 : 1.5, corresponding to an onset of load modulation at $20\log\left(\frac{1}{1.5+1}\right) = -7.96\,dB$ output power backoff.

The frequency range of the wideband DPA demonstrator described in this chapter was defined to cover the lower cellular bands, esp. E-UTRA bands 8, 20 and 28. In accordance to another wideband DPA demonstrator[2], built at an earlier stage of the authors research, the center frequency was set to 850 MHz, which is approximately in the middle of the previously mentioned E-UTRA bands. The new demonstrator design was aimed at a relative bandwidth of 40 %, corresponding to a 680 - 1020 MHz frequency range, and a full state output power of 300 W.

[1] Even in cases of asymmetric drain bias [39], [40] the transformation ratio of the impedance inverter is not reduced, but the transformation is shifted from backoff to full state.

[2] The older wideband DPA demonstrator [48], built in 2013, is mentioned here only for reference and will not be further discussed in this work. It featured a relative bandwidth of 35 % at a full state output power of 100 W. Although this was a very successful design, it used a different combiner topology and is therefore less suited to validate the theoretical findings of chapter two, which are the primary achievement of this work.

At the moment, the GaN HEMT is the optimum transistor technology for the design of wideband RFPA's [49]–[51]. Due to their high power density, these devices feature very low output capacitances and their 50 V drain bias capability results in higher loadline resistances, and thus lower transformation ratios, at high output power levels. In numerous successful PA design projects conducted during his research, the author has become familiar with the 400 nm and, more recently, the 250 nm GaN HEMT technology offered by Cree Inc., the market leader in this segment. Among commercially available, unmatched GaN HEMT devices, they offer the best performance and the manufacturer provides exceptionally accurate large signal models. The latter is absolutely crucial, since the wideband DPA design problem, as it is handled in this work, is a highly multidimensional problem. Tackling the effects of varying, multi-harmonic termination conditions over a wide frequency and power range based on traditional design principles (i.e. empirical, discrete, loadpull data) is just impossible. Simulation based design is thus mandatory. These aspects narrowed the choice of active devices down to two transistors:

Device	Technology	P_{out} rating	Prematching	Duty factor
CGHV40100F (main)	250 nm / 50 V	100 W	unmatched in-/output	fully specified for CW operation
CGHV14250F (peak)	250 nm / 50 V	250 W	prematched input/ unmatched output	maximum continuous power dissipation $\approx$170 W

Table 3.1: Choice of active devices for the 300 W wideband dual-input DPA demonstrator

A full state current ratio of 1 : 2.5, as indicated by the output power ratings, would be unfavourably high for the design of a wideband DPA. However, the manufacturers output power ratings are misleading in this case, because the 250 W device is specified for pulsed operation in a Class-AB operating mode. The device is not 'oversized' for CW operation at Class-C bias and an output power level of about 200 W, which means that its output capacitance is not unnecessarily high. On the other hand, the 100 W device can well be operated at 120 W output power if adequate termination conditions are provided. Thus, this 100 W / 250 W transistor pair is well suited for the design of the wideband DPA demonstrator. The actual full state fundamental current ratio in the wideband DPA demonstrator design is in the range of 1 : 1.4 to 1 : 1.5.

3.2 Linear deembedding

The basic idea behind the combiner design strategy used in this work is to start with an ideal combiner representation as derived in chapter two and then successively move towards a realistic combiner circuit design. The first step on this way is to absorb the active devices' output parasitics (i.e. linear drain-source capacitance and package parasitics) in the combiner network. In order to do so, we need a linear two port representation of each device's output parasitics. The large signal models offered by the device manufacturer are encapsulated black box models and do not allow direct access to the output parasitics. However, these models feature a dynamic loadline option, which enables the designer to assess the intrinsic drain voltage and current. In the following, it will be briefly described how this feature can be used to extract linear output parasitic models from the large signal models.

Assuming a linear two-port model $[S]$ for the output parasitics, the intrinsic load reflection coefficient can be expressed as

$$\Gamma_{int} = S_{11} + \frac{S_{12}\,S_{21}\,\Gamma_{ext}}{1 - S_{22}\,\Gamma_{ext}} \tag{3.6}$$

This constitutes a Möbius transformation

$$w = \frac{a\,z + b}{c\,z + d} \tag{3.7}$$

In order to calculate the complex transformation coefficients $\{a, b, c, d\}$, it is sufficient to know three transformation pairs $\{\{z_1, w_1\}, \{z_2, w_2\}, \{z_3, w_3\}\}$. Based on these transformation pairs, the coefficients can be calculated using the cross-ratio preservation property of the Möbius transformation [52]. A simple method to acquire three transformation pairs would be using $\Gamma_L \in \{-1, 0, 1\}$, as is done in the well known TOSL calibration, but this is obviously impractical for the task at hand, because the transistor must be presented with reasonable load termination conditions. Therefore, a reasonable large signal operating point, including proper termination conditions, is obtained via harmonic balance based loadpull simulations. By introducing small perturbations to the load and monitoring the effect on the intrinsic termination condition, assessed via the dynamic loadline option, we can then acquire the transformation pairs needed in order to calculate the transformation parameters of the parasitic output network. A determinant formula can be used to calculate the coefficients directly from the transformation pairs

$$a = \begin{vmatrix} z_1 w_1 & w_1 & 1 \\ z_2 w_2 & w_2 & 1 \\ z_3 w_3 & w_3 & 1 \end{vmatrix} \quad b = \begin{vmatrix} z_1 w_1 & z_1 & w_1 \\ z_2 w_2 & z_2 & w_2 \\ z_3 w_3 & z_3 & w_3 \end{vmatrix} \quad c = \begin{vmatrix} z_1 & w_1 & 1 \\ z_2 & w_2 & 1 \\ z_3 & w_3 & 1 \end{vmatrix} \quad d = \begin{vmatrix} z_1 w_1 & z_1 & 1 \\ z_2 w_2 & z_2 & 1 \\ z_3 w_3 & z_3 & 1 \end{vmatrix} \tag{3.8}$$

The S-Parameters of the parasitic network follow as

$$S_{11} = \frac{b}{d} \qquad S_{22} = -\frac{c}{d} \qquad S_{12} = S_{21} = \sqrt{\frac{a}{d} - \frac{bc}{d^2}} \tag{3.9}$$

The drawback of this method is that it assumes that the output parasitics reproduced by the large signal model are linear, which in reality they are not[3]. The first workaround for this problem is to choose a reasonably linear large signal operating point and avoid strong compression. A second workaround is to 'linearize' the method by obtaining more than just three transformation pairs[4] and average the transformation coefficients. Finally, a physical representation of the parasitic model, as shown in Figure 3.3, is fitted to the S-Parameter data extracted from the large signal models. This ensures that the de-embedding network is passive, reciprocal and has a valid frequency response. The parameters obtained for the active devices used in the demonstrator design are summarized in Table 3.2.

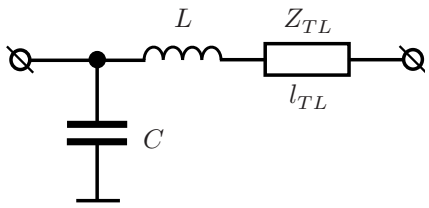

Figure 3.3: Linear parasitic model

Active device	C [pF]	L [pH]	Z_{TL} [Ω]	l_{TL} @ 0.85 GHz
CGHV40100F	7.07	18.8	11.9	5.47°
CGHV14250F	13.03	297.6	4.05	3.32°

Table 3.2: Linear parasitic model parameters

[3] Interestingly, the output parasitics of the older 400 nm device models behaved far more linear than those of the newer 250 nm device models. It is not clear whether this is just a consequence of the higher amount of non-linearity exhibited by the smaller gate length devices, or if the internal details of the large signal modelling have been changed.

[4] e.g. by placing the perturbation triplets in a triangle around the large signal termination and introducing a swept offset angle.

3.3 Combiner design

With a linear de-embedding network at hand, the multi-harmonic current sources used in chapter two are now replaced with large signal models of the actual active devices and the behaviour of the wideband DPA is further analysed by means of harmonic balance simulations. Figure 3.4 illustrates this approach.

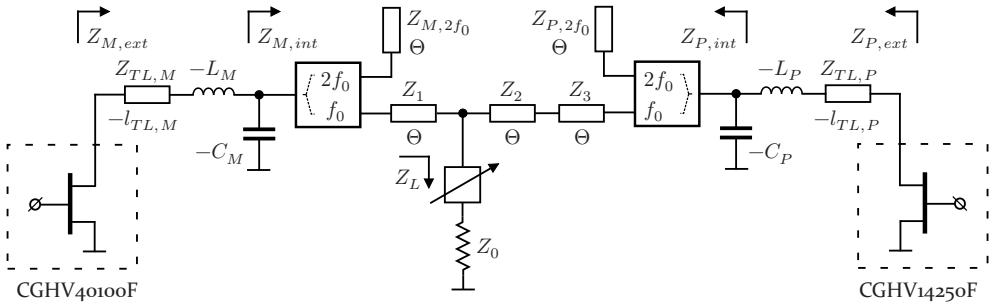

Figure 3.4: Class-J Doherty model with linear deembedding[5]

Due to the actual bias conditions of the GaN HEMTs in the DPA demonstrator (Class-AB / Class-C), compression that occurs when the drain voltage waveform approaches the knee voltage and other non-linear effects [50], [53], the true harmonic content of the intrinsic waveforms differs significantly from the ideal Class-B / Class-J waveforms that were assumed in chapter two. The advantage of using an idealized combiner model like the one shown in Figure 3.4 as an intermediate step in the combiner design process is that it allows us to take into account the non-linearity of the actual active devices without moving too far away from the load modulation principles outlined in chapter two. It allows us, at least to some extend, to separate the deviations that result from the non-linear behaviour of the actual transistors from the physical and technical limitations of network synthesis that we have to face when designing an actual combiner circuit. The active devices' termination conditions obtained in this intermediate step are also used for an initial design of the input networks. Although this can severely complicate the design process, it is important to incorporate realistic frequency responses of the input networks into the design at an early design stage, since the source terminations at the

[5] Bias T's, baseband and higher harmonic terminations not drawn.

fundamental and 2nd harmonic frequency can have a significant effect on the harmonic content of the waveforms[6].

After readjusting the, now unnormalized, combiner model parameters to the large signal transistor models in a harmonic balance simulation environment, small signal two-port parameters of the optimized combiner model, including the de-embedding networks, are extracted. The two-port model of the optimum combiner circuit is then used as a target for the synthesis of the actual combiner circuit. This temporary separation between the large signal DPA simulation and the combiner network synthesis is advantageous from a practical point of view, since the network synthesis based on simple S-Parameter simulations is much more convenient and faster than harmonic balance simulations. But also from a theoretical point of view, the synthesis of the combiner network poses a challenge on its own, due to the multizone nature of the optimum termination conditions defined before.

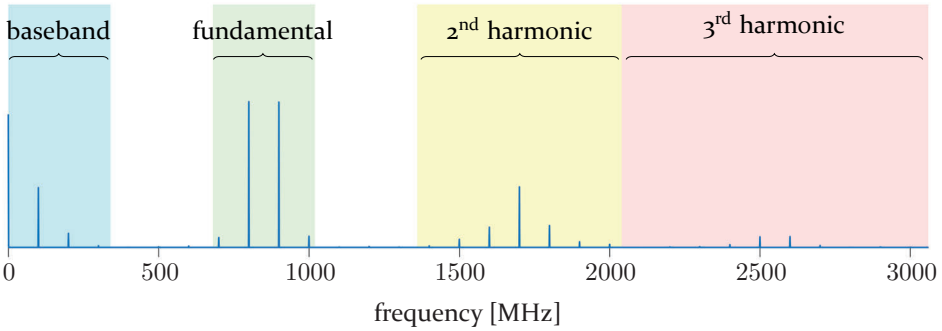

Figure 3.5: Termination zones in frequency domain

The combiner circuit has to adopt a bandpass characteristic, closely approximating the scattering characteristics of the optimum wideband Doherty combiner at the fundamental frequency band while at the same time suppressing out-of-band transmission between the amplifier cores and providing proper reflection coefficients to the amplifier cores at the second harmonic band and at baseband. Figure 3.5 illustrates the individual termination zones for the frequency scenario of the wideband DPA demonstrator. The spectral lines drawn in Figure 3.5 reflect the linear amplitudes of an exemplary [E2] two-tone drain current spectrum, as it occurs in a Class-AB amplifier core. This has been included in order to emphasize the importance of the

[6] In active devices that do not use internal pre-matching on the input, these interrelations become much more prominent than in pre-matched devices.

out-of-band termination conditions not only from the perspective of efficient waveform shaping, but also with regard to linearity [53]. If the wideband DPA shall be used in concurrent wideband or multi-band operation scenarios, the baseband termination becomes as important as the 2nd harmonic termination.

In order to absorb the, predominantly capacitive, output parasitics of the active devices in the combiner, the homogeneous $\lambda/4$ transmission lines used in the ideal combiner model are replaced by semi-lumped microstrip structures [54], [55]. The inherent low-pass characteristic of the semi-lumped network also provides the degree of freedom necessary in order to create a transmission zero at the second harmonic frequency band. On the other side of the frequency range, at DC, a transmission zero is created by the drain bias feeds, which are implemented as shorted stubs. The closed-form microstrip component models used in the initial combiner synthesis were then successively replaced by parametrized, EM simulation based models[7]. Accurate EM modelling is a crucial step in the design of the combiner since the aspect ratios of the microstrip components used in the semi-lumped design often fall outside the valid range of available closed-form models [54] and especially the frequency range of the higher harmonics[8] is dominated by higher order modes. As last step in the combiner design, the parametrized, EM simulation based, combiner model was integrated in the large signal simulation environment together with the non-linear transistor models and S-Parameter models of the actual input networks for a final optimization.

Figure 3.6 shows the resulting combiner design, implemented on a 20 mil thick Rogers TMM4 substrate, as it is used in the wideband DPA demonstrator. This rather simple network topology has been chosen because it approximates the previously defined, optimum wideband DPA combiner close enough in order to experimentally validate the theoretical findings outlined in chapter two, while at the same time not completely abandoning the standard DPA combiner designs used in industry. It has been found that, by use of higher order filter structures, especially in the output transformer, a better approximation of the optimum wideband DPA combiner is indeed possible, but at the price of further increased complexity, size, transmission losses and implementation risks. Especially the, then necessary, inclusion of additional shorted stubs or parallel inductors seems problematic from a practical point of view. Thus, the combiner design presented here does not represent the best theoretically possible solution, but shall be seen as an application oriented,

[7] EM-simulation based microstrip component models were generated using Keysight's ADS momentum advanced model composer.

[8] All passive structures in the demonstrator design have been model from DC to 8.5 GHz.

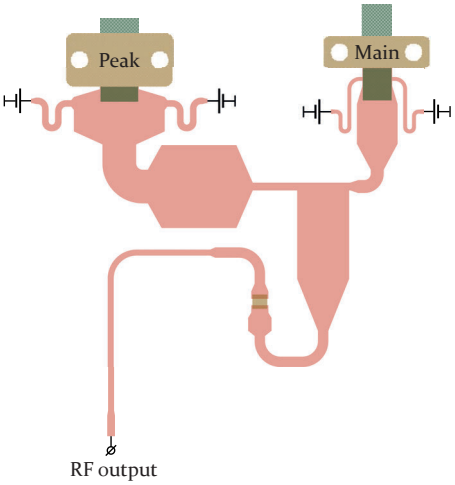

Figure 3.6: Actual combiner circuit layout used in the wideband DPA demonstrator

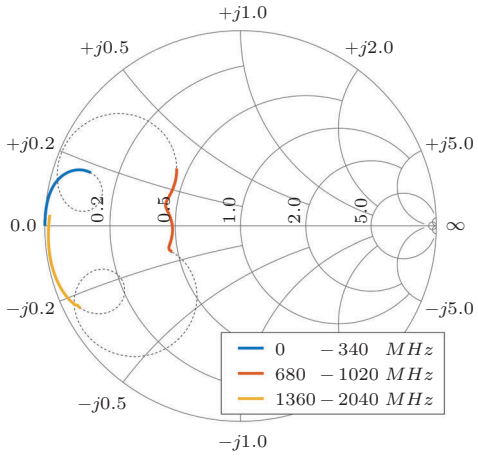

Figure 3.7: Intrinsic small signal termination of the main amplifier core at baseband (blue), fundamental (red) and 2nd harmonic (yellow)

implementation friendly compromise. The small signal input impedance as seen from the intrinsic current generator plane of the main amplifier core at deep backoff into the combiner is plotted in Figure 3.7. It shows a typical band-pass characteristic and we also see that the fundamental and 2nd harmonic terminations lie inside a Class-J impedance continuum fairly well, although they are not placed symmetrically around the Class-B point. With respect to the practical limitations of network synthesis, it is inevitable to trade off the termination conditions at the fundamental frequency band against those at baseband and the 2nd harmonic frequency band. There is a tendency in favour of the fundamental termination conditions in this trade-off, since these are most critical with regard to the output power design goals, which must be met by all means. Thus, out-of-band rejection is not perfect over the entire frequency range and deviations from the optimum termination conditions must be accepted at the upper edge of the baseband frequency range as well as at the lower edge of the 2nd harmonic frequency range. The implications that these imperfections have on the large signal performance of the wideband DPA will be revealed in the following section.

3.4 Simulation results

Throughout this work, it has been made very clear that the performance of the wideband DPA is critically dependent upon the choice of drive functions. A simulation based assessment of the entire load modulation space would require at least[9] a three-dimensional sweep over the input powers and the relative phase between the inputs to be performed for every frequency point. The issue is further complicated by the fact that a simple tool that would enable us to map the three-dimensional load modulation space data obtained from simulations or measurements to a meaningful, definite, two-dimensional representation is not easily available, since the clipping mechanisms in actual transistors are far more complicated and ambiguous than the ideal clipping operator used in chapter two. The development of practical equivalents to the ideal clipping operator, summarized under the term 'compression control', is subject of ongoing research, which will be briefly discussed at the end of this work. Since the scope of this dissertation did not allow for the cumbersome, simulative identification and preparation of the entire load modulation space of the new wideband DPA demonstrator, another path has been chosen. Appropriate drive functions have been constructed directly, based on the following rules, in agreement with the theoretical findings of chapter two:

1. In the **low power region**, defined by the absence of load modulation ($I_{DS,P} = 0$), the input power to the main amplifier core is increased until a clipping criterion based on gain compression and a minimum intrinsic knee voltage is reached. The same criterion has been used to define the backoff point BO during the combiner design process. Thus, the power at this point equals the design target for the backoff power, 50 W.

2. The low power region is followed by the **linear Doherty region**. The drive function in this region is defined according to the findings of chapter two, namely the 1st linearity criterion expressed as

$$\frac{I_{DS,M}(\Gamma)}{\sqrt{P_{out}(\Gamma)}} = \frac{I_{DS,M}(BO)}{\sqrt{P_{out}(BO)}} \tag{3.10}$$

   $I_{DS,M}$ refers to the intrinsic fundamental drain current component of the main amplifier core, assessed via the dynamic load line option of the

[9] Performing HB simulations directly for arbitrary input triplets is not always feasible. HB convergence may require additional source stepping, which adds another dimension to the input parameter sweep.

active device's large signal model. A gradient search algorithm has been applied in order to find the input triplet that fulfills equation 3.10 for a given output power target[10]. The drive function for the linear Doherty region is constructed by successively increasing the output power target and searching for the corresponding input triplet. The point at which the algorithm first fails to find an input triplet for the given output power target is defined as the maximum output power of the linear Doherty range, analogue to the definition in 2.3.5.

3. If the maximum output power of the linear Doherty range is lower than the targeted full state output power, a **non-linear load modulation range** is defined, in which the linearity requirement of equation 3.10 is omitted. A gradient search is used again in order to find the input triplets for a given output power target, with the side condition of maximizing the PAE.

The obtained input drive functions are stored in .mdif files, which can be accessed directly from the harmonic balance simulation environment. In this way, a linear output power sweep based on the appropriate input drive functions is performed easily. The dynamic load line option of the active devices' large signal models allows the definition of an intrinsic load modulation factor

$$\Gamma = \frac{I_{DS,P}}{I_{DS,M}} \tag{3.11}$$

in analogy to equation 2.11, which, in turn, enables a comparison between the actual, simulated load modulation trajectories and the theoretical findings of chapter two, without having to consider the impact that the active devices' non-linearities have on the input drive functions, which would otherwise blur the picture.

The 'intrinsic' drive functions, represented by the intrinsic load modulation factor trajectories, are plotted in Figure 3.8. Around the center of the passband, at frequencies 850 MHz and 935 MHz, the targeted full state power is reached within the linear Doherty range. This means that the maximum output power of the linear Doherty range at center frequency is slightly higher than the targeted full state power, in line with the findings of section 2.7.

[10] Due to the complicated, bilateral, non-linear behaviour of the active devices, this definition is not necessarily non-ambiguous with regard to the input parameters. A lowly-weighted PAE criterion has been added to the goal function in order to enforce unambiguity.

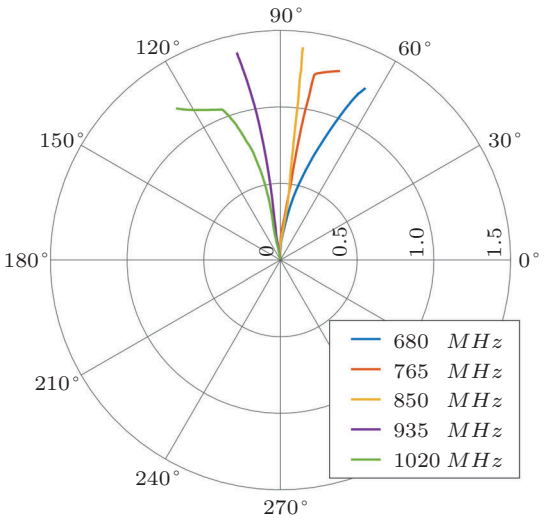

Figure 3.8: Simulated load modulation factor trajectories $\Gamma = \frac{I_{DS,P}}{I_{DS,M}}$

At the band edges, 765 MHz and 1020 MHz, the targeted full state power cannot be reached within the linear Doherty range, but in the subsequent non-linear load modulation range. The respective load modulation factor trajectories exhibit a transition from the linear Doherty mode to a non-linear, 'quasi-outphasing' mode, exactly as predicted by the theory developed in chapter two. Within the linear Doherty range, the simulation results also validate the circular characteristic of the linear drive function derived in subsection 2.3.3. At the lowest frequency point, at 680 MHz, the load modulation factor trajectory deviates from the theoretical expectations, because the targeted full state power is reached within the linear Doherty range again. This can be traced back to the fact that, at this frequency, the actual termination conditions differ significantly from the ideal Class-J load modulation scheme assumed in chapter two. Plotting the intrinsic termination conditions[11] (s. Figure 3.9) over the entire load modulation range reveals significant 2nd harmonic load modulation effects at the lower band edge. As discussed in the previous section, this is a consequence of the limitations of network synthesis. When the DPA design objectives are stretched towards octave bandwidth, the distance between the upper edge of the fundamental band and the lower edge of the second harmonic band diminishes. Since it is physically impossible to design a combiner that features a scattering characteristic suitable to active load modulation at the fundamental frequency band while changing abruptly to a completely reflective termination zone at the 2nd harmonic frequency band, it seems inevitable to accept some degree of 2nd harmonic load modulation at the lower band edge in an actual wideband DPA design[12]. Plotting the minimum value of the intrinsic drain voltage waveforms as a function of output power (s. Figure 3.10) further

[11] Obtained via linear de-embedding.
[12] At least unless push-pull amplifier cores are used [11].

demonstrates the soundness of the theoretical findings. It shows that, at the band edges, the peak amplifier core's intrinsic drain voltage saturates before full state power is reached, followed by an area of mutual voltage saturation, which corresponds to a quasi-outphasing operation.

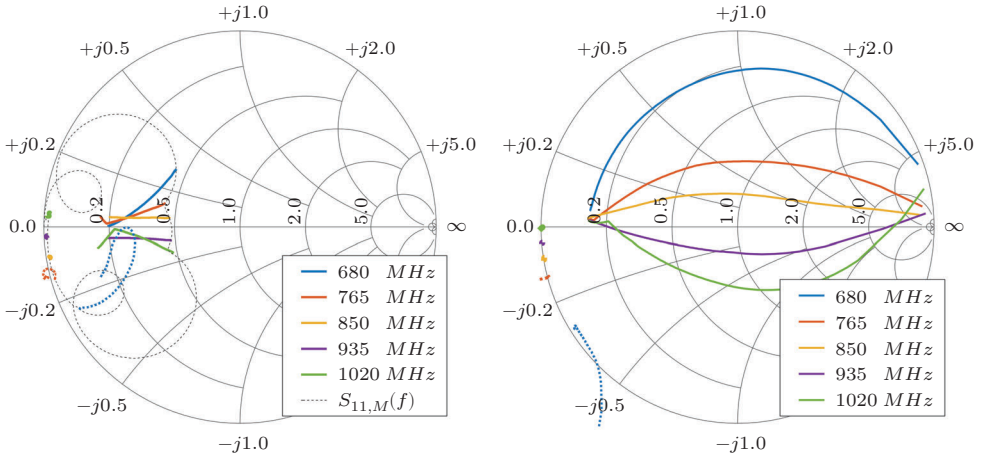

a) Main amplifier core **b)** Peak amplifier core

Figure 3.9: Fundamental (solid) and second harmonic (dotted) intrinsic load trajectories

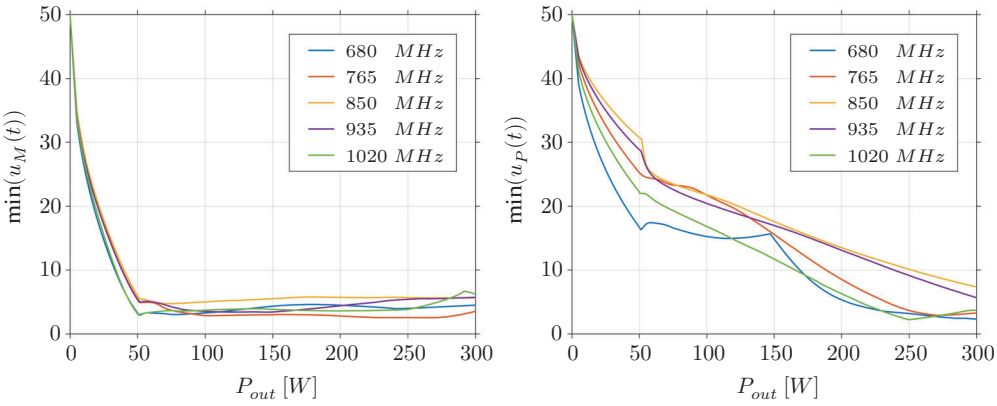

a) Main amplifier core **b)** Peak amplifier core[12]

Figure 3.10: Global minimum of the intrinsic drain voltage waveforms

[12] Note that the discontinuity in the 680 MHz curve around 150 W is a consequence of the min()-operator and marks the crossing from one local minimum in the waveform to another, a phenomenon that we already encountered in the theoretical analysis of the Class-J load modulation space (s. section 2.5.3). It has no impact on the drive functions.

On the other hand, in the center of the passband, at frequencies 765 MHz and 850 MHz, the peak amplifier core is not fully saturated at full state, in accordance to the findings of section 2.7.

Finally, Figure 3.11 shows the efficiency characteristics of the wideband DPA demonstrator. When interpreting these results, it should be kept in mind that very moderate compression level targets were used in the design of the amplifier and in the generation of the drive functions. Stronger compression, which would allow for higher efficiencies at the price of higher static as well as dynamic non-linearity, has been deliberately avoided with respect to the intended use of the wideband DPA demonstrator in other research projects, in which it shall serve as a testbed for the development of advanced predistortion techniques for concurrent multi-band and continuous wideband operation. Furthermore, non-linear waveform shaping techniques like Class-FJ, which are able to boost efficiency in a limited sub-area of the overall bandwidth, were not considered in this design, due to a lack of time[13]. Before moving to the measurement results in section 3.6., the next section will take a closer look at the demonstrator's implementation details.

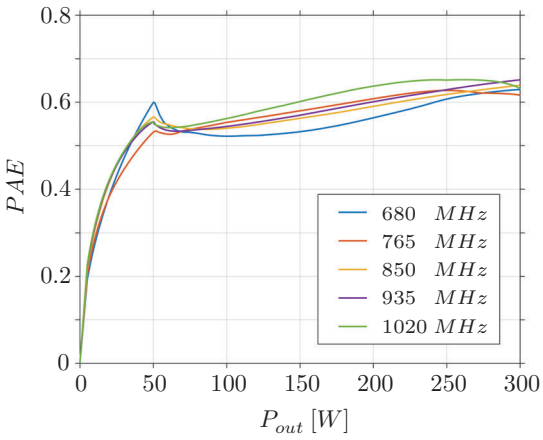

Figure 3.11: Simulated instantaneous power added efficiency vs. output power

3.5 Implementation

Discrete RF circuit design in general and RF power amplifier design in particular requires careful mechanical implementation. For the wideband DPA demonstrator presented in this chapter, a closed aluminium[14] housing has been designed in order to provide sufficient shielding to eliminate pick up

[13] A Class-FJ termination of the main amplifier core has been successfully applied in an older wideband DPA demonstrator designed by the author [48], which is not covered in this work. Those results are available upon request and might be published in the future.

[14] EN AW-6082

of pervasive parasitic signals at cellular frequencies, which could otherwise disturb measurements. In order to facilitate a fast acquisition of the DC supply current data while at the same time keeping the impedance of the DC bias feeds as low and the physical size of the demonstrator as small as possible, a sandwich architecture is used. Feed-through capacitors, screwed into the 6 mm thick, metallic backplate, connect the RF circuit board directly to a separate DC supply board, which is mounted on the opposite side of the backplate. The disadvantage of this architecture is that it is not well suited for conduction cooling, which is normally used in cellular base stations, due to the rather high thermal resistance that would be present between the active devices and a heat sink mounted to the outside of the housing. This problem was avoided by application of water cooling. Cooling channels, which run directly underneath the active devices, have been milled into the backplate. The coolant enters and exits the cooling channels through drill holes that lead to self-closing quick couplings[15] mounted to the side of the housing. A metal cover plate and a rubber[16] gasket seal the water cooling compartment, as shown in Figure 3.12.

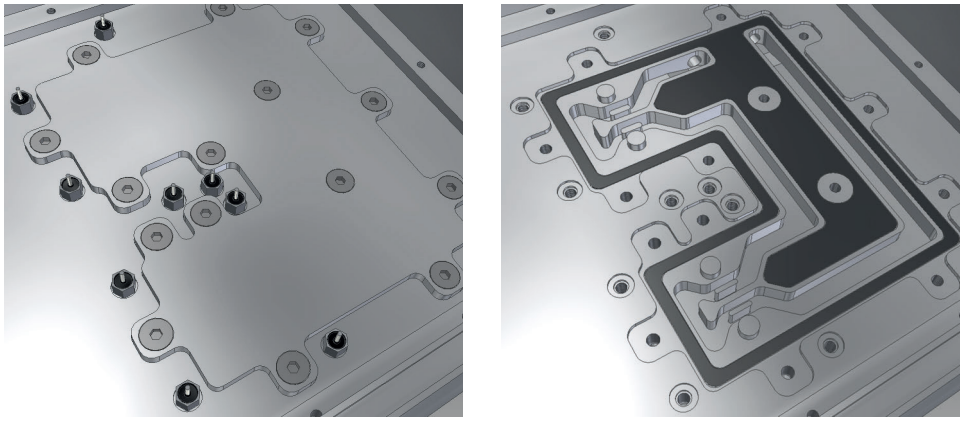

a) DC side of the housing without PCB; Feed-through capacitors and water cooling compartment lid visible

b) Internal details of the water cooling compartment with rubber gasket

Figure 3.12: Implementation of water cooling

[15] Parker Rectus Series 21
[16] EPDM 50° Shore, thickness 1.5 mm

The DC supply board does not only provide the low-impedance DC sources for the bias voltages, but also contains extensive monitoring and control circuitry. In particular, it features:

- **An E-Fuse:** If a drain current fault ($I_D > 15$ A) is detected, a high side switch very quickly (< 200 ns) disconnects the RF devices from the capacitor bank, preventing further damage to the expensive GaN HEMTs.
- **A wideband drain current sense:** A precise drain current sense with about 1 MHz measurement bandwidth is included in order to facilitate a fast acquisition of the PAs instantaneous efficiency data. The current sense circuit drives a separate 50 Ohm SMA output for the connection to an oscilloscope or other external data acquisition platform. The difficulty of providing a fast current measurement facility without increasing the drain bias feed impedance too much was met by placing a 10 mOhm shunt resistor between the feed-through capacitors that connect the RF circuit board and the large capacitor bank that buffers the drain supply voltage. The reason for the substantial effort made at this point is that the fast acquisition of the PA's instantaneous efficiency has been deemed a vital feature for the intended future usage of the wideband DPA demonstrator in research projects on advanced predistortion and system identification for dual-input, wideband DPAs.
- **Thermal monitoring and bias compensation:** The temperature on the RF circuit board is measured via an NTC sensor, mounted between the active devices. The temperature signal is used for temperature compensation of the active devices' gate bias voltage, as well as for a safety shutdown in case of over-temperature ($T_{case} \geq 85°$C). The signal is also fed to the demonstrators I/O port, in order to allow external access to the temperature data.
- **Bias sequencer and safety shutdown mechanisms:** A state machine, built from discrete logic gates, ensures that the drain voltage is turned on only if correct gate bias is present and that it is safely switched off in case of a gate voltage or over-temperature fault, or if the auxiliary supply voltage is suddenly disconnected.
- **Auxiliary power supplies:** A dual channel, low noise, wide input voltage range (4.5 V ≤ U_{AUX} ≤ 26 V) DC/DC converter, based on ZETA and Ćuk topologies, generates the bipolar supply voltages (+7.5 V and -10 V) for the auxiliary circuitry on the DC supply board. Furthermore, the

DC supply board contains a +5 V linear voltage regulator for the supply of the monitoring and logic circuitry, as well as two precision voltage references for the gate bias regulators and for the drain current sense circuit, respectively.

- **I/O and supply port:** The demonstrator's combined I/O and supply port contains two high current pins for the +50 V drain voltage supply of the amplifier and additional low current pins for the auxiliary supply voltage input, an external switching input to the drain voltage high side switch, an error flag output and an analogue temperature output. The I/O and supply port is, by design, foolproof, which means that all pins can withstand severe over-voltage and reverse polarity conditions without damage to the circuitry.

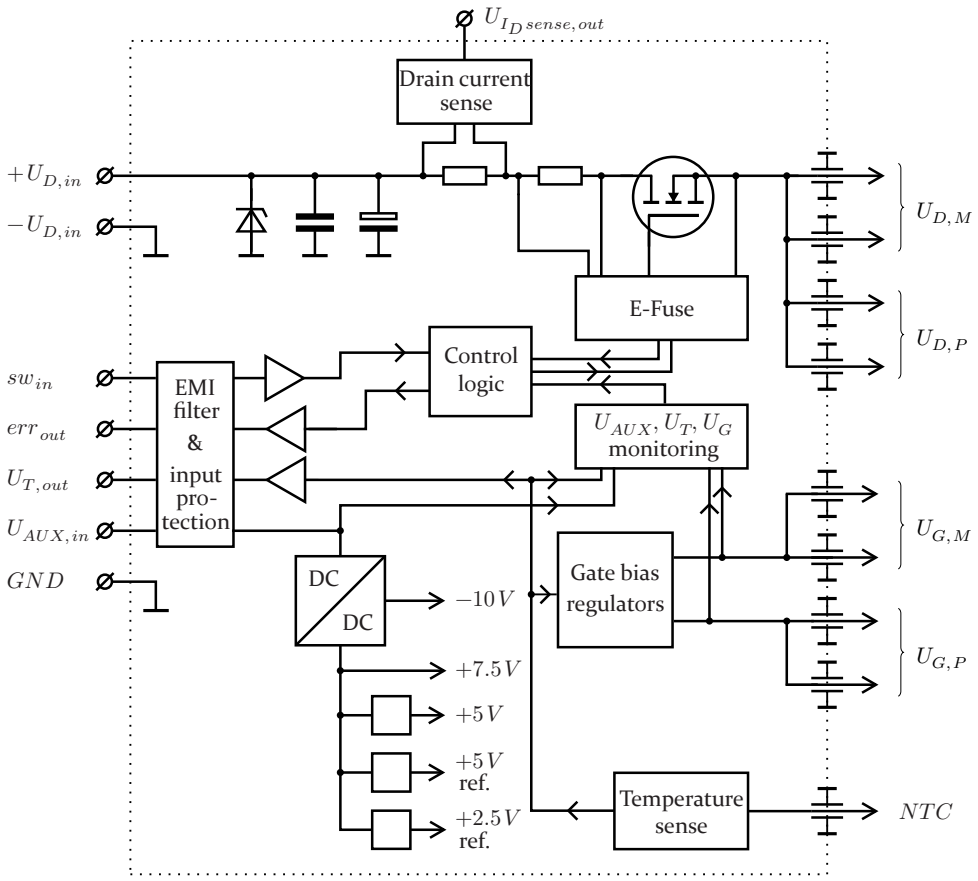

Figure 3.13: Block diagram of the DC Supply Board

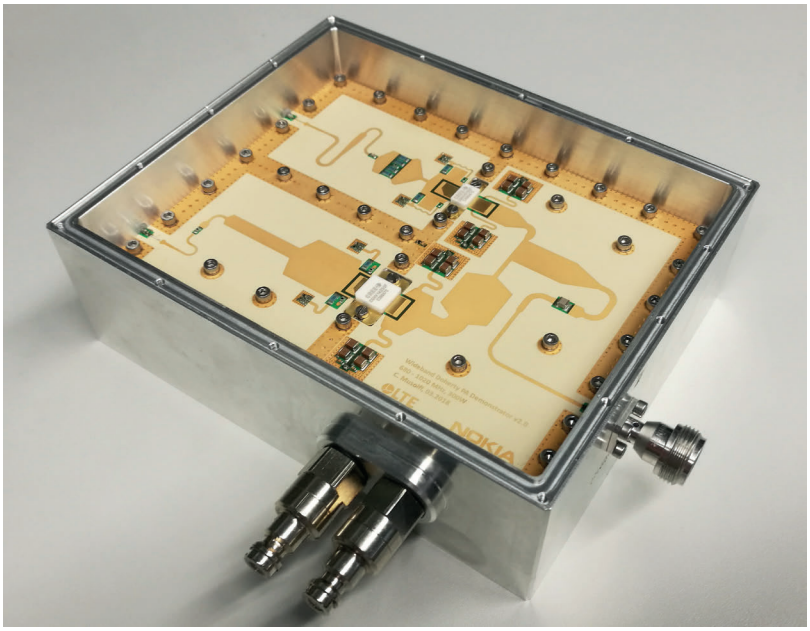

Figure 3.14: RF side of the 300 W, 680 - 1020 MHz wideband DPA demonstrator

Figure 3.15: DC side of the 300 W, 680 - 1020 MHz wideband DPA demonstrator

3.6 Measurement results

The setup that has been used for the measurements of the wideband dual-input DPA demonstrator is based on a proprietary signal generation and acquisition platform which has been provided by our project partner. The platform is connected to a PC via an USB interface and controlled from a Matlab environment. It comprises an FPGA board and a proprietary RF frontend that allows for the synchronized generation and acquisition of modulated and unmodulated RF signals on multiple TX and RX channels with an instantaneous bandwidth > 400 MHz. The TX output signals of the RF frontend are low-pass filtered and pre-amplified to the power levels necessary in order to drive the wideband dual-input DPA demonstrator. Directional couplers in front of the pre-amplifiers as well as after the pre-amplifiers allow for the acquisition of feedback signals that are used for the absolute power calibration of the setup and for a continuous assessment of the drive signals at the DUT's inputs. This allows to compensate for drift phenomena in the driver amplifiers and to cancel out the influence of their non-linearity on the generated drive functions[17]. The output of the DUT is terminated by means of a high power attenuator, after which a feedback signal is coupled out and fed to another feedback receiver. Since the traditional methods of port mismatch correction

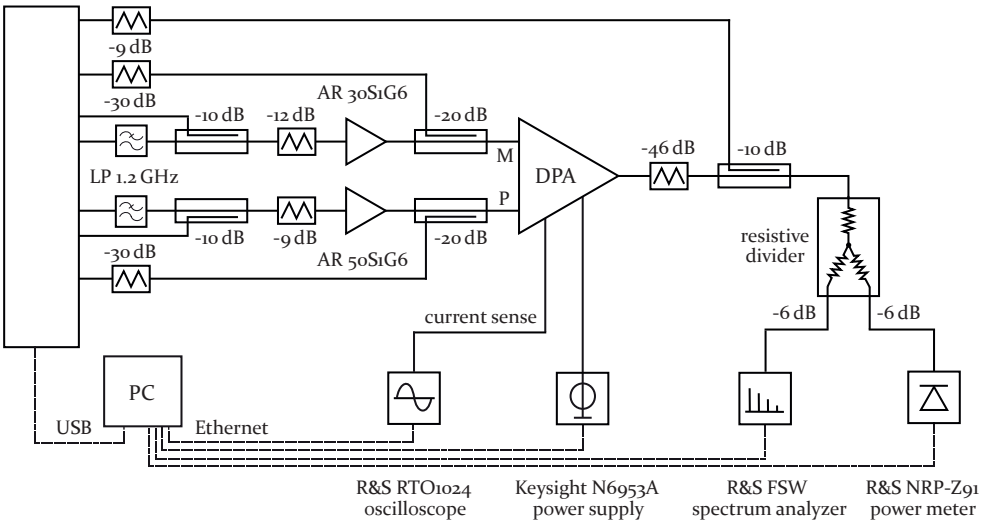

Figure 3.16: Measurement setup

[17] The latter aspect is not significant in this case, since highly linear driver amplifiers are used.

used in linear network analysis are inadequate for the measurement of non-linear DUTs like a power amplifier, great care has been exercised to provide a well matched 50 Ohm environment at the test ports, in order to achieve sufficient accuracy and repeatability of the RFPA measurements. The acquired feedback signals are digitally filtered to a bandwidth of 5 MHz and averaged 10 times, in order to eliminate noise. The power calibration of the setup is performed in two steps. Initially, a source power calibration for both TX paths is obtained by means of a power meter connected to the input test ports. Based on the source power calibration, the receiver powers and phase relations are then calibrated using a through standard between each input test port and the output test port. For verification purposes during measurements, a part of the DUT's output signal is fed to a power meter as well as a spectrum analyzer, which allows to quickly check for harmonic and spurious components[18].

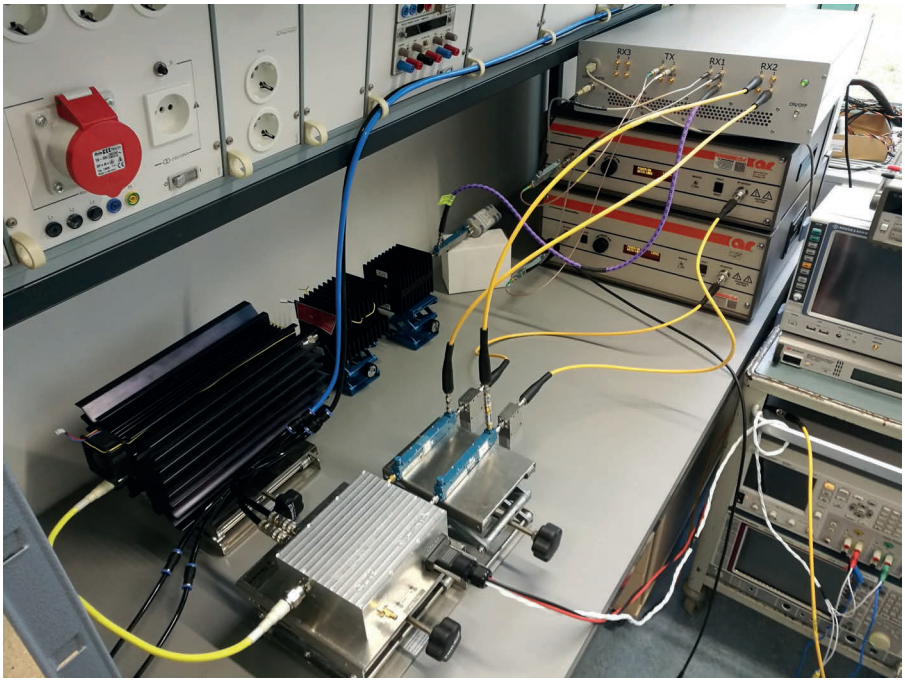

Figure 3.17: Wideband DPA demonstrator on the test bench

[18] Suppression of the 2nd harmonic at full state is around -20 dBc at 680 MHz, and better than -25 dBc at all other frequencies. Suppression of the 3rd harmonic is better than -20 dBc at full state. Spurious components other than the harmonics are not present.

It has already been pointed out before that the performance of the dual-input DPA in the load modulation region is critically dependent on the choice of explicit drive functions and that this severely complicates the characterization of an actual dual-input DPA implementation. While the static transfer function of the traditional single-input DPA is injective and can be identified completely by performing a simple power sweep, this does not work for the dual-input DPA anymore, because its transfer function is not injective and multidimensional. A three-dimensional sweep over the input variables - two input amplitudes and the relative phase between the inputs - would be the only way to completely characterize the load modulation space of an actual dual-input DPA in a straightforward fashion, but this approach is prohibitively tedious even when it is only done in simulation. Based on measurements, it is practically impossible, because the amplifier would very likely be destroyed in the attempt, due to unduly high VSWR conditions that would arise from presenting the amplifier with arbitrary input drive combinations. Thus, a more intelligent method must be found in order to characterize the dual-input DPA in the load modulation region.

In the case of the simulation based drive function identification discussed in section 3.4, the knowledge of the intrinsic current and voltage conditions, gained through the dynamic loadline option of the active device models, allowed to identify input drive functions based on intrinsic saturation criteria. However, a measurement of the intrinsic voltage and current conditions is usually not feasible (except from some very sophisticated techniques that probe the EM field at the package plane or even directly at the die of the transistor [56], [57]). The simulation based drive functions can only be used as rough orientation for the measurement based drive function generation, since a certain degree of deviation between simulation and measurement in the phase offset as well as in the gain of the individual amplifier cores is inevitable. In this regard, especially the thermal behaviour of the active devices played an important role, due to the very high output power levels and suboptimal cooling conditions present during the measurements shown here[19]. Furthermore, the drive function identification algorithm that was used in the measurements is oriented towards input drive function linearity (as opposed to 'intrinsic' drive function linearity, which could be assessed in simulation

[19] In simulations, a constant baseplate temperature of 30°C was assumed. This could not be reproduced in the measurements, due to limitations in the water cooling infrastructure available in the institutes provisional laboratory in conjunction with the very high ambient temperature experienced in June 2018. Coolant inlet temperatures of up to 35°C had to be accepted.

by means of the dynamic load line option) and PAE and therefore tends to produce higher compressions levels than those used in the simulations.

Figures 3.18 to 3.23 show the measurement results obtained for the 300 W wideband dual-input DPA demonstrator under CW conditions. Contrary to the usual logarithmic representation, the results are presented in linear power domain, because this allows for a better view on the load modulation range, and especially on details like the Doherty-Outphasing transition, which are otherwise easily missed. A good overall agreement between simulation and measurement is observed. In the lower half of the frequency range the measured efficiency is even slightly higher than the simulated efficiency, which is at least partly due to the fact that the very conservative compression criteria that were used in the simulations could not be accurately reproduced during measurements, as outlined in the last paragraph.

Most importantly, the transition from the linear Doherty mode to a 'quasi-outphasing' mode, which is one of the most important findings of this work and which has been identified clearly in simulations due to the availability of the intrinsic current and voltage data, is also verified by the measurements.

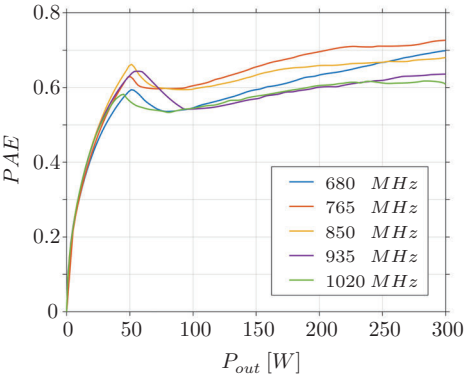

Figure 3.18: Measured instantaneous power added efficiency vs. output power

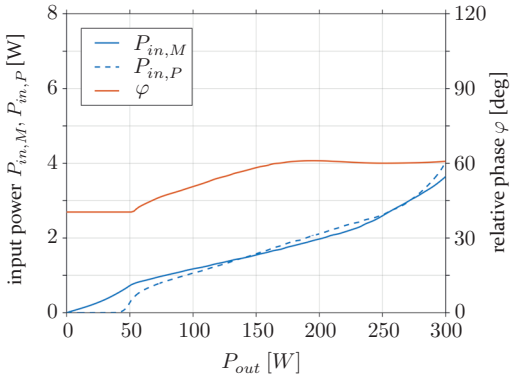

Figure 3.19: Drive functions at 680 MHz

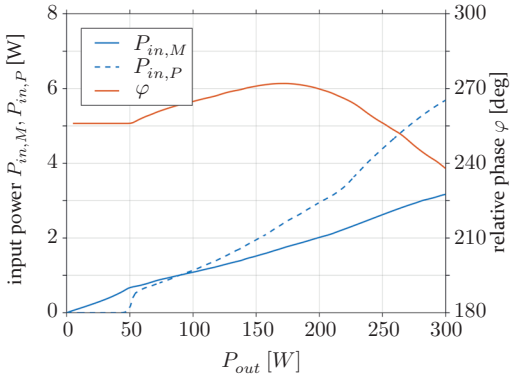

Figure 3.20: Drive functions at 765 MHz

At the frequency points 765 MHz and 1020 MHz, at which the simulation results clearly indicated the presence of a 'quasi-outphasing' mode at high powers, we see a typical outphasing profile in the measurement based drive functions as well. While operating the DPA in the Doherty mode, the output power is increased mostly by increasing the input powers, with a relatively weak dependency on the relative phase, but when, at a certain point, both amplifier cores are driven into significant compression, the dependency between output power and relative phase becomes much stronger. From this point onwards, steering the amplifier into the 'quasi-outphasing' mode is the only way to further increase the output power, which is very much in line with the theoretical findings. This behaviour has not only been observed on the DPA demonstrator presented in this work, but also on other wideband, dual-input DPAs designed by the author before.

Another observation that can be made from the drive functions is that the main amplifiers input power functions show a compressive characteristic in the medium power range, which corresponds to a gain expansion in the main amplifier path. This increase in transconductance in the main path is a side-effect of load modulation and also

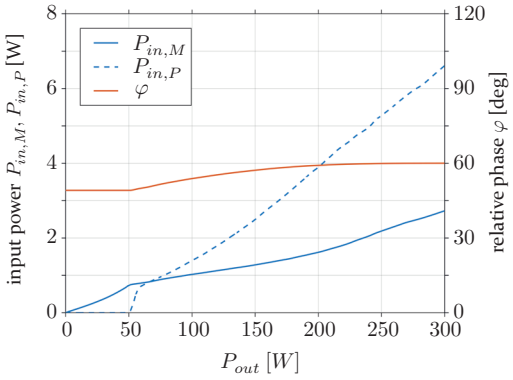

Figure 3.21: Drive functions at 850 MHz

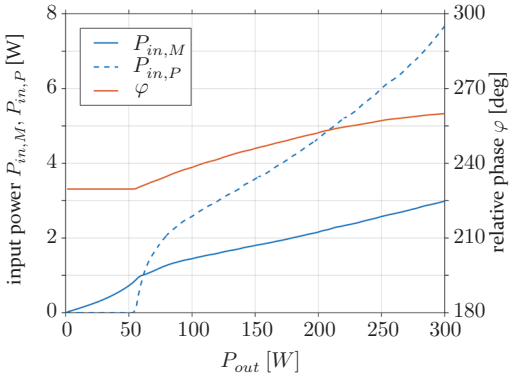

Figure 3.22: Drive functions at 935 MHz

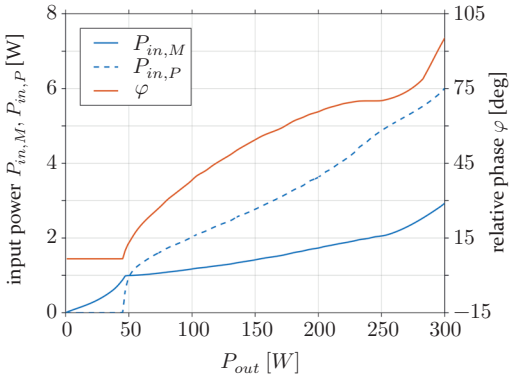

Figure 3.23: Drive functions at 1020 MHz

plays an important role in the overall linearity of conventional, single input, Doherty PAs [E2]. Furthermore, a certain amount of AM-PM distortion can be observed in the medium power region. While the AM-PM characteristic in the 'intrinsic' drive functions (s. Fig. 3.8), which is due to the detuned operation, as derived in chapter two, exhibits a rather symmetric behaviour, extending in either direction at the respective band edges, this symmetry usually does not make its way into the input drive functions, because it is superposed by the AM-PM distortion produced by the active devices, which always extends in the same direction, due to the capacitive nature of its origin [58]. In case of the input drive function at 765 MHz, this explains the local maximum in the function of the relative phase which precedes the transition to the 'quasi-outphasing' mode.

Unfortunately, measurement results for modulated signals could not be included at this point, due to a lack of time in the final phase of this work. The problem of drive function identification, compression control and digital predistortion in wideband dual-input DPAs is subject of ongoing research by my esteemed colleague Thomas Ackermann. More details on these topics, including measurement results of the wideband DPA demonstrator for modulated signals, will be published in due course.

4 Discussion and Outlook

4.1 Discussion of results

As a result of the author's acquaintance with the techniques of waveform engineering, made in lengthy multi-harmonic loadpull measurement sessions at the beginning of his time as a graduate student, one of the initial objectives of this work became trying to implement continuous wideband, linear termination conditions in a Doherty PA. It has been pointed out in section 2.2 that, by proper choice of the complex load match, a Class-J termination of the main amplifier core at backoff is indeed possible in the DPA. This already is an important improvement on its own, because the performance at deep backoff is highly important to the overall performance of the cellular base station's TX signal chain, which does not only face the high PAPR of the signal, but is also operated at significant average power backoff most of the time. Extending the analysis to the load modulation region soon revealed, that, in theory, the main amplifier core could be tuned to virtually any termination condition by a particular choice of the drive function. However, analysis also showed that enforcing arbitrary (e.g. ideal Class-J) termination conditions on the main amplifier core in the load modulation region is not advisable, because it delivers suboptimal results. Thus, a method had to be developed that allows to evaluate the potential performance of a certain Doherty output network without relying on the explicit choice of a drive function and, on the other hand, to understand the implications that the output network has on the drive function. In that effort, the method of load modulation space analysis presented in chapter two has been developed. A summary and discussion on the load modulation space analysis and the combiner design space analysis based on it has been given at the end of chapter two, in section 2.8, and shall therefore not be reiterated at this point. Nevertheless, it seems important to point out again that the insights gained in chapter two have a very fundamental meaning to the topic of wideband active load modulation. Aside from any potential usage value, these results hold a significant educational value, which the author wishes to emphasize. In times of artificial intelligence and evolu-

tionary algorithms, wideband circuit design very often has more to do with mastering simulation techniques and optimization algorithms than with the thorough understanding of an underlying problem. While this development seems reasonable, or even essential, in some fields (e.g. distributed network synthesis), it probably cannot replace the kind of insight developed in chapter two.

With the objective of verifying the theoretical results, a wideband, dual-input DPA demonstrator with a full state output power of 300 W in a relative bandwidth of 40 % has been designed, as presented in chapter three. To the best of the author's knowledge, this demonstrator shows the highest and most steady efficiency performance over the given relative bandwidth in its output power class demonstrated in the literature so far. Table 4.1 gives a quick comparison of state-of-the-art wideband DPA designs published in the literature. It lies in the nature of such a comparison that it does not always provide the complete picture, because not every detail of the respective

Reference	Frequency range [GHz]	rel. BW [%]	$P(1)$ [dBm]	BO [-dB]	PAE_{FS} [%]	PAE_{BO} [%]	Implementation details
[44]	1.7 - 2.6	42	42.1 - 45.3	6	50 - 55	41 - 55	single input
[59]	1.6 - 2.25	43	53	6	58 - 70	40 - 58	single input
[43]	0.47 - 0.78	50	58.4	6	49 - 56	41 - 45	LDMOS, single input
[11]	0.52 - 0.76	37	58.4	6	55 - 62	48 - 57	LDMOS, single input, push-pull DPA
[60]	1.7 - 2.4	36.3	39 - 41	6	53 - 72	43 - 59	bare die, single input
[39]	1.5 - 2.5	50	42	5 - 10	32 - 50	30 - 42	bare die, dual input, reconfig. drain bias
[41]	1 - 3	100	43.1 - 44.9	6	42 - 62	45 - 65	bare die, dual input, mixed mode
[40]	0.7 - 1	35.3	49	6	65 - 70	51 - 64	single input, asym. drain bias
[61]	2 - 2.7	29.8	40 - 42	7 - 10	58 - 69	50 - 75	single input
[62]	1.8 - 2.7	40	54	7	63 - 69	49 - 54	single input
2013 DPA demonstrator by the author [48]	0.7 - 1	35.5	50	7.5 - 8.2	65 - 81	60 - 79	dual input, Class-FJ
this work	**0.68 - 1.02**	**40**	**54.8**	**7.8**	**61 - 73**	**56 - 66**	**dual input**

Table 4.1: Comparison of state-of-the-art CW results for GaN[1] wideband DPAs published in the literature

[1] Unless noted otherwise.

implementations can be considered. While some of the designs found in the literature, especially those using bare die transistors, are more or less experimental setups, the wideband DPA demonstrator presented in this work comes quite close to an industrial product design.

Due to the limited time available for the completion of this work, not all aspects of the design procedure have been described in full detail. Although not unimportant, subjects like input network design have been left out, because they do not add much to the topic of this work and can also be found elsewhere. The main accomplishment of the demonstrator design is that it provides evidence for the soundness of two of the most important aspects of the theoretical findings: The feasibility and advantage of continuous multi-harmonic termination conditions at backoff and the existence of a transition from the linear Doherty mode to a non-linear 'quasi-outphasing' mode at high powers. The Class-J type backoff termination at the current generator plane of the main amplifier core clearly shows up in the simulation results and is verified by the measurement results, which show a steady high efficiency operation at the intended backoff power level of 50 W over the entire operational bandwidth of the DPA demonstrator. At high power levels, the measurement based drive functions also validate the presence of a Doherty-Outphasing transition in amplitude domain, as predicted by theory and simulations. However, this effect is by far not as obvious in the measurement results as it is in theory, because these two perspectives are separated by two levels of abstraction: The mapping of the intrinsic drain current vectors to a two-dimensional load modulation space and the transfer of the input drive functions to the intrinsic drain currents of the active devices. The step from the input drive functions of the active devices to their intrinsic drain current functions is particularly troublesome, because all of the non-linear effects inherent to real world transistors are superimposed on the mechanisms in load modulation space, blurring their impact (e.g. due to the AM-PM distortion generated by the active devices) or even partially suspending them. The non-linear and bilateral behaviour of the transistors significantly restricts the space of intrinsic drive functions that can be accessed via the input drive functions, especially in saturation and when facing reactive loads. It is exactly this issue which also hampers practical implementations of the Chireix architecture at microwave frequencies.

The significant blurring of its impact is probably also one of the reasons why the presence of the Doherty-Outphasing transition in amplitude domain has not been recognized by the literature. In many cases, it just disappears in

overall compression. This leads over to the important question of compression control in dual-input DPAs, which will be discussed in the next section.

4.2 Outlook

The concept of a digitally assisted dual-input DPA is often countered with the argument that such a device must be regarded as a transmitter system and not just as an amplifier, like the classic DPA. This is obviously true, but the same applies to every other high efficiency, wideband transmitter architecture as well. Even the classic DPA is seldom used without digital predistortion in commercial applications, because the use of a DPD allows significantly better performance in terms of backoff efficiency and bandwidth, as compared to DPA implementations with sufficiently high native linearity [E2]–[E4]. The implementation costs of digital signal preprocessing may still be prohibitive for certain low-volume applications, but in mass applications like cellular mobile radio, this is not an issue. Moore's law will eventually take care of the problem.

The dual-input Doherty concept is not only interesting from the perspective of bandwidth enhancement, but it also provides the tools necessary for a better control of the active devices compression levels. **Compression control** techniques can be used in order to optimize the backoff efficiency performance, reduce compression-induced memory effects and increase the reliability of the amplifier circuit even in narrowband DPA implementations. A control of the intrinsic compression levels by means of dual-input drive functions, however, necessitates that these compression levels are known, which is usually not the case in a DPA, as discussed in section 3.6. Thus, one of the most pressing questions for further research in this field is how to assess the intrinsic saturation conditions of the active devices in the dual-input DPA without actually looking into the devices. An in-situ characterization of the individual branches of the dual-input DPA is possible in principle, for example by means of noise injection techniques, but further research is necessary in order to derive correct information on the intrinsic saturation conditions from such noise signatures. With respect to the methods developed in this work, a functional compression control technique would serve as a practical equivalent to the clipping operator used in chapter two and would thus constitute a valuable tool in the assessment of the load modulation space and the generation of proper wideband drive functions.

Another approach towards increasing the average efficiency of the wideband dual-input DPA that has been conceptualized in the course of this work is

the concept of **dynamic drive functions**, which has evolved in reaction to the presence of the Doherty-Outphasing transition in load modulation space. While the input drive functions in CW operation can assume any shape, this is no longer true when modulated signals are considered. Under dynamic input signal conditions, the optimum drive functions are only approximated, according to the bandwidth available to the predistortion. Assuming that the available bandwidth is limited, it is very disadvantageous to always do this approximation for the entire output power range, because that leads to a situation in which the discontinuity in the derivative of the drive function due to the Doherty-Outphasing transition impairs the quality of the approximation at lower power levels, even though the signal amplitude rarely reaches the outphasing region. Figure 4.1 illustrates this thought. The approach does not only apply to the Doherty-Outphasing transition in a detuned DPA, but also to the onset point of load modulation, which generates another characteristic discontinuity in the derivative of the drive function, even in a tuned DPA. The idea behind the dynamic drive function concept is to dynamically adjust the drive function approximation to the maximum power level present in a certain interval of the signal, such that, on average, the approximation of the ideal drive function and thus the efficiency is improved. It is indeed possible to switch between different drive functions without generating additional bandspread, under the condition that the switching is done below a certain amplitude threshold, because at low amplitude levels, prior to the onset of load modulation, the drive function approximations converge, as can be seen in Fig. 4.1.

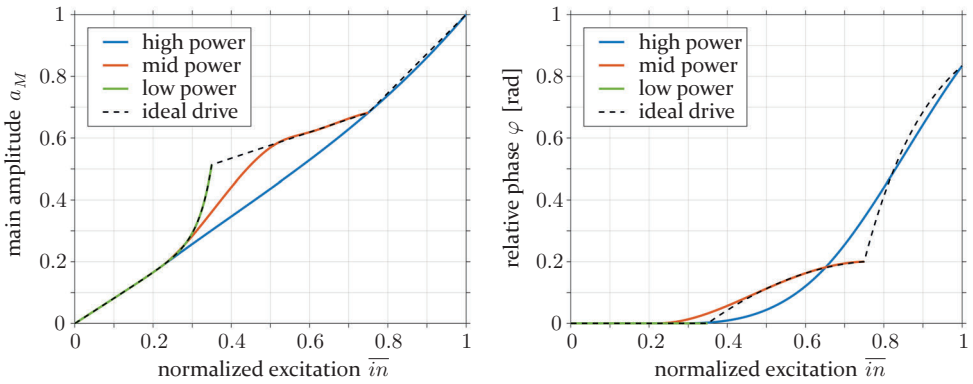

Figure 4.1: Illustration of the concept of dynamic drive functions. If the drive function bandwidth is limited, the approximation accuracy depends on the maximum amplitude up to which the ideal drive function is approximated.

In order to enable a practical implementation of the dynamic drive function technique, advanced predistortion models must be developed, addressing the lack of a genuine support of the wideband dual-input DPA architecture in current predistortion models. Due to the similarity between the proposed dynamic drive technique and the general problem of wideband/multi-band predistortion, it is expected that an appropriate wideband/multi-band predistortion model for the dual-input DPA will be able to incorporate the dynamic drive function concept without significantly increasing its complexity. To promote further research in the field of digital predistortion and system identification for wideband dual-input DPAs, the concepts of compression control and dynamic drive functions have been merged into the framework of the DFG research grant 'DynaDrive' [63], which has been approved in 2017. The wideband dual-input DPA demonstrator developed in this work serves as a testbed for the ongoing research in the signal processing field.

Bibliography

[1] S. Cherry. "Edholm's law of bandwidth". In: *IEEE Spectrum* 41.7 (July 2004), pp. 58–60. ISSN: 0018-9235. DOI: 10.1109/MSPEC.2004.1309810.

[2] Cisco Systems Inc. *Cisco Visual Networking Index: Global Mobile Data Traffic Forecast Update, 2016 - 2021 White Paper*. Feb. 2017.

[3] S.C. Cripps. *RF Power Amplifiers for Wireless Communications*. Artech House Microwave Library. Artech House, 2006. ISBN: 9781596930186.

[4] S.C. Cripps. *Advanced Techniques in RF Power Amplifier Design*. Artech House Microwave Library. Artech House, 2002. ISBN: 9781580535649.

[5] J. Qureshi. "High Efficiency RF Power Amplifier Architectures". PhD thesis. TU Delft, 2012. ISBN: 9789462030718.

[6] F. H. Raab, P. Asbeck, S. Cripps, et al. "Power amplifiers and transmitters for RF and microwave". In: *IEEE Transactions on Microwave Theory and Techniques* 50.3 (Mar. 2002), pp. 814–826. ISSN: 0018-9480. DOI: 10.1109/22.989965.

[7] R. Caverly, F. Raab, and J. Staudinger. "High-Efficiency Power Amplifiers". In: *IEEE Microwave Magazine* 13.7 (Nov. 2012), S22–S32. ISSN: 1527-3342. DOI: 10.1109/MMM.2012.2216716.

[8] M. Eron, B. Kim, F. Raab, et al. "The Head of the Class". In: *IEEE Microwave Magazine* 12.7 (Dec. 2011), S16–S33. ISSN: 1527-3342. DOI: 10.1109/MMM.2011.942725.

[9] M. Siddiqui. "Some problems connected with Rayleigh distributions". In: *Research of the NBS, Section D, Radio Propagation* 66D (1962), pp. 167–174.

[10] R. M. H. Smith and S. C. Cripps. "Broadband push-pull power amplifier design at microwave frequencies". In: *2016 46th European Microwave Conference (EuMC)*. Oct. 2016, pp. 1353–1356. DOI: 10.1109/EuMC.2016.7824603.

[11] J. He, J. H. Qureshi, W. Sneijers, et al. "A wideband 700W push-pull Doherty amplifier". In: *2015 IEEE MTT-S International Microwave Symposium*. May 2015, pp. 1–4. DOI: 10.1109/MWSYM.2015.7166772.

[12] F. H. Raab. "Maximum efficiency and output of class-F power amplifiers". In: *IEEE Transactions on Microwave Theory and Techniques* 49.6 (June 2001), pp. 1162–1166. ISSN: 0018-9480. DOI: 10.1109/22.925511.

[13] V. Carrubba, A. L. Clarke, M. Akmal, et al. "On the Extension of the Continuous Class-F Mode Power Amplifier". In: *IEEE Transactions on Microwave Theory and Techniques* 59.5 (May 2011), pp. 1294–1303. ISSN: 0018-9480. DOI: 10.1109/TMTT.2011.2117435.

[14] N. Tuffy, L. Guan, A. Zhu, et al. "A Simplified Broadband Design Methodology for Linearized High-Efficiency Continuous Class-F Power Amplifiers". In: *IEEE Transactions on Microwave Theory and Techniques* 60.6 (June 2012), pp. 1952–1963. ISSN: 0018-9480. DOI: 10.1109/TMTT.2012.2187534.

[15] N. O. Sokal and A. D. Sokal. "Class E-A new class of high-efficiency tuned single-ended switching power amplifiers". In: *IEEE Journal of Solid-State Circuits* 10.3 (June 1975), pp. 168–176. ISSN: 0018-9200. DOI: 10.1109/JSSC.1975.1050582.

[16] L. R. Kahn. "Single-Sideband Transmission by Envelope Elimination and Restoration". In: *Proceedings of the IRE* 40.7 (July 1952), pp. 803–806. ISSN: 0096-8390. DOI: 10.1109/JRPROC.1952.273844.

[17] G. Strasser, B. Lindner, L. Maurer, et al. "On the Spectral Regrowth in Polar Transmitters". In: *2006 IEEE MTT-S International Microwave Symposium Digest*. June 2006, pp. 781–784. DOI: 10.1109/MWSYM.2006.249770.

[18] K. Chen and D. Peroulis. "Design of Adaptive Highly Efficient GaN Power Amplifier for Octave-Bandwidth Application and Dynamic Load Modulation". In: *IEEE Transactions on Microwave Theory and Techniques* 60.6 (June 2012), pp. 1829–1839. ISSN: 0018-9480. DOI: 10.1109/TMTT.2012.2189232.

[19] R. Amirpour, R. Darraji, F. Ghannouchi, et al. "Enhancement of the Broadband Efficiency of a Class-J Power Amplifier With Varactor-based Dynamic Load Modulation". In: *IEEE Microwave and Wireless Components Letters* 27.2 (Feb. 2017), pp. 180–182. ISSN: 1531-1309.

[20] K. Mimis, S. Wang, and G. T. Watkins. "A load-modulated low-power amplifier with average power tracking". In: *2015 European Microwave Conference (EuMC)*. Sept. 2015, pp. 88–91.

[21] K. Mimis and G. T. Watkins. "Bandwidth reduction in dynamic load-modulated power amplifiers: control and RF signal expansion, efficiency and linearity trade-offs". In: *2015 IEEE Topical Conference on Power Amplifiers for Wireless and Radio Applications (PAWR)*. Jan. 2015, pp. 1–3.

[22] C. W. Horn. "Ten Years of Broadcasting". In: *Proceedings of the Institute of Radio Engineers* 19.3 (Mar. 1931), pp. 356–376. ISSN: 0731-5996. DOI: 10.1109/JRPROC.1931.222334.

[23] W. H. Doherty. "A New High Efficiency Power Amplifier for Modulated Waves". In: *Proceedings of the Institute of Radio Engineers* 24.9 (Sept. 1936), pp. 1163–1182. ISSN: 0731-5996. DOI: 10.1109/JRPROC.1936.228468.

[24] V. Vorapipat, C. S. Levy, and P. M. Asbeck. "Voltage Mode Doherty Power Amplifier". In: *IEEE Journal of Solid-State Circuits* 52.5 (May 2017), pp. 1295–1304. ISSN: 0018-9200. DOI: 10.1109/JSSC.2017.2647954.

[25] R. Pengelly, C. Fager, and M. Ozen. "Doherty's Legacy: A History of the Doherty Power Amplifier from 1936 to the Present Day". In: *IEEE Microwave Magazine* 17.2 (Feb. 2016), pp. 41–58. ISSN: 1527-3342. DOI: 10.1109/MMM.2015.2498081.

[26] R. E. Stengel, W.-C. A. Gu, G. D. Leizerovich, et al. "High efficiency power amplifier having reduced output matching networks for use in portable devices". Patent US6262629B1. July 2001.

[27] W. C. E. Neo, J. Qureshi, M. J. Pelk, et al. "A Mixed-Signal Approach Towards Linear and Efficient N-Way Doherty Amplifiers". In: *IEEE Transactions on Microwave Theory and Techniques* 55.5 (May 2007), pp. 866–879. ISSN: 0018-9480. DOI: 10.1109/TMTT.2007.895160.

[28] W.C.E. Neo, M. Pelk, L.C.N. De Vreede, et al. "3-WAY DOHERTY AMPLIFIER WITH MINIMUM OUTPUT NETWORK". Patent EP2235820B1. Aug. 2013.

[29] K. Motoi, A. Wentzel, M. Tanio, et al. "Digital doherty transmitter with envelope $\Delta\Sigma$ modulated class-D GaN power amplifier for 800 MHz band". In: *2014 IEEE MTT-S International Microwave Symposium (IMS2014)*. June 2014, pp. 1–4. DOI: 10.1109/MWSYM.2014.6848280.

[30] H. Chireix. "High Power Outphasing Modulation". In: *Proceedings of the Institute of Radio Engineers* 23.11 (Nov. 1935), pp. 1370–1392. ISSN: 0731-5996. DOI: 10.1109/JRPROC.1935.227299.

[31] F. Raab. "Efficiency of Outphasing RF Power-Amplifier Systems". In: *IEEE Transactions on Communications* 33.10 (Oct. 1985), pp. 1094–1099. ISSN: 0090-6778. DOI: 10.1109/TCOM.1985.1096219.

[32] Z. Abou-Chahine, T. Felgentreff, G. Fischer, et al. "An input amplitude modulated harmonic outphasing PA". In: *2013 13th Mediterranean Microwave Symposium (MMS)*. Sept. 2013, pp. 1–4. DOI: 10.1109/MMS.2013.6663082.

[33] D. J. Perreault. "A New Power Combining and Outphasing Modulation System for High-Efficiency Power Amplification". In: *IEEE Transactions on Circuits and Systems I: Regular Papers* 58.8 (Aug. 2011), pp. 1713–1726. ISSN: 1549-8328. DOI: 10.1109/TCSI.2011.2106230.

[34] D. Cox. "Linear Amplification with Nonlinear Components". In: *IEEE Transactions on Communications* 22.12 (Dec. 1974), pp. 1942–1945. ISSN: 0090-6778. DOI: 10.1109/TCOM.1974.1092141.

[35] R. Langridge, T. Thornton, P. M. Asbeck, et al. "A power re-use technique for improved efficiency of outphasing microwave power amplifiers". In: *IEEE Transactions on Microwave Theory and Techniques* 47.8 (Aug. 1999), pp. 1467–1470. ISSN: 0018-9480. DOI: 10.1109/22.780396.

[36] R. Hellberg. "Composite power amplifier". Patent EP1470635B1. June 2006.

[37] A. Grebennikov and J. Wong. "Doherty amplifier". Patent EP2634916A1. Sept. 2013.

[38] A. Grebennikov and J. Wong. "A Dual-Band Parallel Doherty Power Amplifier for Wireless Applications". In: *IEEE Transactions on Microwave Theory and Techniques* 60.10 (Oct. 2012), pp. 3214–3222. ISSN: 0018-9480. DOI: 10.1109/TMTT.2012.2210906.

[39] D. Gustafsson, C. M. Andersson, and C. Fager. "A Modified Doherty Power Amplifier With Extended Bandwidth and Reconfigurable Efficiency". In: *IEEE Transactions on Microwave Theory and Techniques* 61.1 (Jan. 2013), pp. 533–542. ISSN: 0018-9480. DOI: 10.1109/TMTT.2012.2227783.

[40] D. Y. T. Wu and S. Boumaiza. "A Modified Doherty Configuration for Broadband Amplification Using Symmetrical Devices". In: *IEEE Transactions on Microwave Theory and Techniques* 60.10 (Oct. 2012), pp. 3201–3213. ISSN: 0018-9480. DOI: 10.1109/TMTT.2012.2209446.

[41] C. M. Andersson, D. Gustafsson, J. Chani Cahuana, et al. "A 1 - 3 GHz Digitally Controlled Dual-RF Input Power-Amplifier Design Based on a Doherty-Outphasing Continuum Analysis". In: *IEEE Transactions on Microwave Theory and Techniques* 61.10 (Oct. 2013), pp. 3743–3752. ISSN: 0018-9480. DOI: 10.1109/TMTT.2013.2280562.

[42] R. Giofrè, L. Piazzon, P. Colantonio, et al. "A Closed-Form Design Technique for Ultra-Wideband Doherty Power Amplifiers". In: *IEEE Transactions on Microwave Theory and Techniques* 62.12 (Dec. 2014), pp. 3414–3424. ISSN: 0018-9480. DOI: 10.1109/TMTT.2014.2363851.

[43] J. H. Qureshi, W. Sneijers, R. Keenan, et al. "A 700-W peak ultra-wideband broadcast Doherty amplifier". In: *2014 IEEE MTT-S International Microwave Symposium (IMS2014)*. June 2014, pp. 1–4. DOI: 10.1109/MWSYM.2014.6848495.

[44] K. Bathich, A. Z. Markos, and G. Boeck. "Frequency Response Analysis and Bandwidth Extension of the Doherty Amplifier". In: *IEEE Transactions on Microwave Theory and Techniques* 59.4 (Apr. 2011), pp. 934–944. ISSN: 0018-9480. DOI: 10.1109/TMTT.2010.2098040.

[45] S. C. Cripps, P. J. Tasker, A. L. Clarke, et al. "On the Continuity of High Efficiency Modes in Linear RF Power Amplifiers". In: *IEEE Microwave and Wireless Components Letters* 19.10 (Oct. 2009), pp. 665–667. ISSN: 1531-1309. DOI: 10.1109/LMWC.2009.2029754.

[46] P. Wright, J. Lees, J. Benedikt, et al. "A Methodology for Realizing High Efficiency Class-J in a Linear and Broadband PA". In: *IEEE Transactions on Microwave Theory and Techniques* 57.12 (Dec. 2009), pp. 3196–3204. ISSN: 0018-9480. DOI: 10.1109/TMTT.2009.2033295.

[47] T. Canning, P. J. Tasker, and S. C. Cripps. "Continuous Mode Power Amplifier Design Using Harmonic Clipping Contours: Theory and Practice". In: *IEEE Transactions on Microwave Theory and Techniques* 62.1 (Jan. 2014), pp. 100–110. ISSN: 0018-9480. DOI: 10.1109/TMTT.2013.2292675.

[48] T. Felgentreff, C. Musolff, and G. Fischer. "Broadband RF power amplifier with active load modulation". Patent application EP2879291A1. Nov. 2013.

[49] A. Moore and E. Reese. *RF Applications of GaN*. John Wiley & Sons, 2015. ISBN: 9781119135531.

[50] G. Kompa. *Basic Properties of III-V Devices – Understanding Mysterious Trapping Phenomena:* Kassel University Press, 2014. ISBN: 9783862195411.

[51] R. Quay. *Gallium Nitride Electronics*. Springer Series in Materials Science. Springer Berlin Heidelberg, 2008. ISBN: 9783540718925.

[52] K. Meyberg and P. Vachenauer. *Höhere Mathematik 2: Differentialgleichungen, Funktionentheorie, Fourier-Analysis, Variationsrechnung*. Springer-Lehrbuch. Springer-Verlag Berlin Heidelberg, 2003. ISBN: 9783540418511.

[53] J. Vuolevi and T. Rahkonen. *Distortion in RF Power Amplifiers*. Artech House Microwave Library. Artech House, 2003. ISBN: 9781580536295.

[54] G. Kompa. *Practical Microstrip Design and Applications*. Artech House Microwave Library. Artech House, 2005. ISBN: 9781580539807.

[55] G. L. Matthaei, L. Young, and E. M. T. Jones. *Microwave Filters, Impedance-matching Networks, and Coupling Structures*. Artech House Microwave Library. Artech House, 1980.

[56] R. Hou, M. Spirito, J. Gajadharsing, et al. "Non-intrusive characterization of active device interactions in high-efficiency power amplifiers". In: *2013 IEEE MTT-S International Microwave Symposium Digest (MTT)*. June 2013, pp. 1–3. DOI: 10.1109/MWSYM.2013.6697599.

[57] N. Dehghan, S. Cripps, A. Porch, et al. "An improved electric field probe with applications in high efficiency PA design and diagnostics". In: *81st ARFTG Microwave Measurement Conference*. June 2013, pp. 1–4. DOI: 10.1109/ARFTG.2013.6579026.

[58] L. C. Nunes, P. M. Cabral, and J. C. Pedro. "AM/PM distortion in GaN Doherty power amplifiers". In: *2014 IEEE MTT-S International Microwave Symposium (IMS2014)*. June 2014, pp. 1–4.

[59] K. Bathich, M. T. Arnous, and G. Boeck. "Design of 200 W wideband Doherty amplifier with 34% bandwidth". In: *2013 European Microwave Conference*. Oct. 2013, pp. 279–282.

[60] L. Piazzon, R. Giofrè, P. Colantonio, et al. "A Wideband Doherty Architecture With 36% of Fractional Bandwidth". In: *IEEE Microwave and Wireless Components Letters* 23.11 (Nov. 2013), pp. 626–628. ISSN: 1531-1309. DOI: 10.1109/LMWC.2013.2281413.

[61] X. A. Nghiem, J. Guan, and R. Negra. "Broadband Sequential Power Amplifier With Doherty-Type Active Load Modulation". In: *IEEE Transactions on Microwave Theory and Techniques* 63.9 (Sept. 2015), pp. 2821–2832. ISSN: 0018-9480. DOI: 10.1109/TMTT.2015.2456901.

[62] J. Wong, N. Watanabe, and A. Grebennikov. "High-power high-efficiency broadband GaN HEMT Doherty amplifiers for base station applications". In: *2018 IEEE Topical Conference on RF/Microwave Power Amplifiers for Radio and Wireless Applications (PAWR)*. Jan. 2018, pp. 16–19. DOI: 10.1109/PAWR.2018.8310055.

[63] *Dynamic drive for radio frequency power amplifiers with wideband active load modulation, Acronym DynaDrive*. research grant application to the DFG (approved). 2017.

Author's publications

[E1] C. Musolff, A. Neuberger, and R. Kronberger. "Student competition for low-power consumption FM receiver design". In: *IEEE Microwave Magazine* 10.1 (2009), pp. 133–137. DOI: 10.1109/MMM.2008.930735.

[E2] C. Musolff, M. Kamper, Z. Abou-Chahine, et al. "Linear and efficient Doherty PA Revisited". In: *IEEE Microwave Magazine* 15.1 (2014), pp. 73–79. DOI: 10.1109/MMM.2013.2288713.

[E3] C. Musolff, M. Kamper, and G. Fischer. "Linear Doherty PA at 5 GHz". In: *IEEE Microwave Magazine* 16.1 (2015), pp. 89–93. DOI: 10.1109/MMM.2014.2367862.

[E4] C. Musolff, M. Kamper, Z. Abou-Chahine, et al. "A linear and efficient Doherty PA at 3.5 GHz". In: *IEEE Microwave Magazine* 14.1 (2013), pp. 95–101. DOI: 10.1109/MMM.2012.2226998.

[E5] W. Akstaller, C. Musolff, R. Weigel, et al. "X-Parameter Characterization of TC SAW Filters with Enhanced Dynamic Range". In: *IEEE Transactions on Microwave Theory and Techniques* 65.11 (2017), pp. 4541–4549. DOI: 10.1109/TMTT.2017.2751464.

[E6] G. Gottardo, G. Donati, C. Musolff, et al. "Hybrid recursive active filters for duplexing in RF transmitter front-ends". In: *Radio Science* 51.8 (2016), pp. 1363–1376. DOI: 10.1002/2016RS005969.

[E7] G. Gottardo, G. Donati, C. Musolff, et al. "Hybrid recursive active filters for duplexing in RF transmitter front-ends". In: *Mediterranean Microwave Symposium*. Vol. 2015-January. 2015. DOI: 10.1109/MMS.2015.7375476.

[E8] W. Akstaller, A. Tag, C. Musolff, et al. "Measurement setup for X-Parameter characterization of bulk acoustic wave resonators". In: *85th ARFTG Microwave Measurement Conference: Measurements and Techniques for 5G Applications, ARFTG 2015*. 2015. DOI: 10.1109/ARFTG.2015.7162919.

[E9] A. Tag, W. Akstaller, C. Musolff, et al. "Polyharmonic Distortion modeling of RF BAW components". In: *2015 IEEE MTT-S International Microwave Symposium, IMS 2015*. 2015. DOI: 10.1109/MWSYM.2015.7166954.

[E10] C. Musolff, A. Neuberger, and R. Kronberger. "Amplifier sequenced hybrid receiver". In: *IEEE Microwave Magazine* 12.1 (2011), pp. 94–98. DOI: 10.1109/MMM.2010.939317.

List of Symbols

α	Independent parameter in Class-J voltage waveform continuum
ΔR_{max}	Maximum resistance variation within the optimum wideband output match
η	Efficiency $\eta = \frac{P_{out}}{P_{DC}}$
η_A	Efficiency of the Class-A amplifier
η_B	Efficiency of the Class-B amplifier
η_{avg}	Average efficiency
η_{BO}	Efficiency in the low power region ($\Gamma = 0$)
η_{LM}	Efficiency in the load modulation region
γ	Scale parameter of the Rayleigh distribution $\gamma = 10^{-\frac{PAPR[dB]}{10}}$
Γ	Load modulation factor $\Gamma = \frac{I_P}{I_M}$
Γ_{int}	Intrinsic load reflection coefficient presented to the current generator plane of the transistor
Γ_{ext}	Extrinsic load reflection coefficient presented to the package plane of the transistor
λ	Wavelength
φ	Relative phase angle between the two input vectors of a dual input, active load modulation PA architecture
φ_{iPcm}	Intersecting angles on the c_M-limited iso-P circle
φ_{iPcp}	Intersecting angles on the c_P-limited iso-P circle

ϕ	Conduction angle
ϕ_0	Full state conduction angle
ψ	Conformal mapping used in the derivation of the equi-clip circle
Θ	Normalized detuning $\Theta = \frac{\pi}{2}\frac{f}{f_0}$
a, b, c, d, g	Auxilliary variables
a_0, a_1, a_2...	Fourier coefficients of the multi-harmonic current and voltage waveforms
$[A]$	Chain parameter matrix of the output combiner
A_{11}, A_{12}, A_{21}, A_{22}	Chain parameters of the output combiner
BO	Normalized linear input excitation at the onset of load modulation
BW	Relative bandwidth $\frac{f_u - f_l}{f_0}$
c	Global clipping factor $c = \min\{c_M, c_P\}$ (also: auxiliary variable)
c_M, c_P	Clipping factors for the voltage waveforms at the current generator planes of the main and peak amplifier cores, respectively
C, C_M, C_P	Capacitance used in the linear parasitic model
f	Frequency
f_0	Center frequency (also: fundamental frequency band in Fig. 3.4)
$\overrightarrow{i_{DS}}$	Harmonic vector of the drain to source current
i_M, i_P	Instantaneous (time domain) current at the current generator plane of the main and peak amplifier core, respectively
$\overline{in}$	Normalized linear input excitation
int	Normalized linear input excitation at the Doherty-Outphasing transition
I_{DC}	Direct current amplitude

I_{DS}, $I_{DS,M}$, $I_{DS,P}$	Fundamental frequency drain to source current vectors (at the main and peak transistor, respectively)
$\overrightarrow{I_{DS}}$	Drain to source current phasor
I_{f0}	Fundamental frequency current amplitude
I_M, I_P	Fundamental frequency current vector at the current generator plane of the main and peak amplifier core, respectively
I_{Main}, I_{Peak}	Fundamental frequency current amplitude at the current generator plane of the main and peak amplifier core, respectively
j	Imaginary unit
k	Order of the Fourier coefficient
l_{TL}	Electrical length of a transmission line used in the linear parasitic model
L, L_M, L_P	Inductance used in the linear parasitic model
M_{eq}	Center of the equi-clip circle
M_{iPcm}	Center of the c_M-limited iso-P circle
M_{iPcp}	Center of the c_P-limited iso-P circle
M_{dflin}	Center of the linear drive function circle
M_{icm}	Center of the iso-c_M circle
n	(harmonic) Order
P, P_{out}	RF power delivered to load
P_{DC}	DC power consumption
P_{in}	RF input power
$P_{in,M}$, $P_{in,P}$	Input power at the main and peak amplifier path in the wideband DPA demonstrator
P_M, P_{Main}, P_P, P_{Peak}	RF power delivered to load by the main and peak amplifier core, respectively
PAE	Power added efficiency $PAE = \frac{P_{out}-P_{in}}{P_{DC}}$
$PAPR$	Peak to average power ratio

PDF	Probability density function
PUF	Power utilization factor
Q_{max}	Maximum Quality factor within the optimum wideband output match
r_{eq}	Radius of the equi-clip circle
r_{iPcm}	Radius of the c_M-limited iso-P circle
r_{iPcp}	Radius of the c_P-limited iso-P circle
r_{dflin}	Radius of the linear drive function circle
r_{icm}	Radius of the iso-c_M circle
R	Resistance
R_0	Reference resistance
R_L	Center frequency load resistance connected to the common node of the output combiner
R_{Main}, R_{Peak}	Fundamental frequency virtual load resistance at the current generator plane of the main and peak amplifier core, respectively
$[S]$	Scattering matrix of the linear parasitic two-port used in section 3.2
S_{11}, S_{12}, S_{21}, S_{22}	Scattering parameters of the linear parasitic two-port used in section 3.2
$S_{11,M}(f)$	Small signal frequency response of the load reflection coefficient at the current generator plane of the main transistor in the wideband DPA demonstrator
t	Time
T_{case}	Auxilliary supply voltage of the wideband DPA demonstrator
$\overrightarrow{u_{DS}}$	Harmonic vector of the drain to source voltage
u_M, u_P	Instantaneous (time domain) voltage at the current generator plane of the main and peak amplifier core, respectively

U	Voltage amplitude
U_1, U_2	Fundamental frequency voltage vectors at the current generator planes of the Chireix PA
U_{AUX}, $U_{AUX,in}$	Auxilliary supply voltage of the wideband DPA demonstrator
U_{CN}	Fundamental frequency voltage vector at the common node of the output combiner
U_{DC}	Direct voltage amplitude
U_{DS}, $U_{DS,M}$, $U_{DS,P}$	Fundamental frequency drain to source voltage vectors (at the main and peak transistor, respectively)
$\overrightarrow{U_{DS}}$	Drain to source voltage phasor
U_{f0}	Fundamental frequency voltage amplitude
U_G, $U_{G,M}$, $U_{G,P}$	Gate bias voltages in the wideband DPA demonstrator
U_L	Fundamental frequency voltage amplitude at the load
U_M, U_P	Fundamental frequency voltage vector at the current generator plane of the main and peak amplifier core, respectively
U_{Main}, U_{Peak}	Fundamental frequency voltage amplitude at the current generator plane of the main and peak amplifier core, respectively
U_T, $U_{T,out}$	Temperature sense voltage in the wideband DPA demonstrator
w, w_1, w_2, w_3	Images of the Möbius transformation used in section 3.2
X	Reactance
z, z_1, z_2, z_3	Preimages of the Möbius transformation used in section 3.2
Z_0	Reference impedance
Z_1, Z_2, Z_3	Characteristic impedances of the $\lambda/4$ transmission lines in the output combiner

Z_{2f0}	Characteristic impedance of a $\lambda/4$ open stub terminating the 2nd harmonic frequency component at the current generator plane of an amplifier core
Z_{2opt}	Characteristic impedance of the 2nd $\lambda/4$ transmission line in the output combiner, such that the equi-clip condition at the band edges is reached at full state power (s. section 2.7)
Z_{even}	Even mode termination impedance in a push-pull amplifier
Z_{f0}, Z_{2f0}, Z_{3f0}...	Termination impedance at the current generator plane of an amplifier core at the respective harmonic
Z_i, $Z_{i,M}$, $Z_{i,P}$	Characteristic impedance parameter referring to the reactive termination component in the Class-J termination continuum (s. definition on page 40)
Z_L	Load impedance connected to the common node of the output combiner
Z_M, Z_P	Fundamental frequency termination impedance seen at the current generator plane of the main and peak amplifier cores, respectively
$Z_{M,2f_0}$, $Z_{P,2f_0}$	2nd harmonic frequency termination impedance seen at the current generator plane of the main and peak amplifier cores, respectively
$Z_{M,int}$, $Z_{P,int}$	Intrinsic termination impedance presented to the current generator plane of the main and peak transistors, respectively, after linear deembedding
$Z_{M,ext}$, $Z_{P,ext}$	Extrinsic termination impedance presented to the package plane of the main and peak transistors, respectively
Z_{odd}	Odd mode termination impedance in a push-pull amplifier
Z_{T1}, Z_{T2}, Z_{T3} ...	Characteristic impedances of the $\lambda/4$ sections of a multi-section transmission line transformer
Z_{TL}, $Z_{TL,M}$, $Z_{TL,P}$	Characteristic impedance of the transmission line used in the linear parasitic model

List of Abbreviations

AM	amplitude modulation
AM-PM	amplitude modulation to phase modulation
BJT	bipolar junction transistor
BO	backoff
BTS	base transceiver station
BW	bandwidth
CW	continuous wave
DC	direct current
DFG	Deutsche Forschungsgemeinschaft
DPA	Doherty power amplifier
DPD	digital predistortion
DUT	device under test
DVB-T	Digital Video Broadcasting - Terrestrial
E-fuse	electronic fuse
EM	electromagnetic
EMI	electromagnetic interference
EER	envelope elimination and restoration
ET	envelope tracking
E-UTRA	Evolved Universal Mobile Telecommunications System Terrestrial Radio Access
FET	field effect transistor

FPGA	field programmable gate array
FS	full state
GaN	gallium nitride
GSM	Global System for Mobile communications
HB	harmonic balance
HEMT	high electron mobility transistor
HSPA+	Evolved High Speed Packet Access
I	inphase
IEEE	Institute of Electrical and Electronics Engineers
I/O	input/output
LINC	linear amplification with non-linear components
LTE	Long Term Evolution
MTT-S	IEEE Microwave Theory and Techniques Society
NTC	negative temperature coefficient (resistor)
PA	power amplifier
PAE	power added efficiency
PAPR	peak-to-average power ratio
PCB	printed circuit board
PDF	probability density function
Q	quadrature
rel. BW	relative bandwidth
RF	radio frequency
RFPA	radio frequency power amplifier
RX	receive
SMA	Sub-Miniature version A connector
S-Parameters	scattering parameters
TOSL	through-open-short-load

TX	transmit
USB	universal serial bus
VSWR	voltage standing wave ratio

List of Figures

List of Tables

For almost a century, active load modulation techniques have been used to increase the backoff efficiency of high frequency power amplifiers. The Doherty architecture, which is based on active load modulation, has become the standard power amplifier architecture in cellular base station transmitters and makes a significant contribution to the energy-efficient operation of cellular mobile radio networks today.

In recent times, the increasing availability of ever more powerful digital signal processing also led to a paradigm shift in the field of transmitter systems. The application of complex digital predistortion algorithms opens up new ways to overcome some of the bandwidth limitations that are inherent to classic power amplifier architectures based on active load modulation and thus allows to exploit the efficiency advantages of active load modulation also for the increasingly important wideband operation.

In this work, a universal and illustrative method of analysis of multi-harmonic load modulation spaces is developed and the possibilities and characteristics of hybrid modes within the 'Doherty-Outphasing continuum' with regard to wideband operation are investigated. In the last part of the work, the theoretical findings are verified using a wideband Doherty PA demonstrator with a peak output power of 300 W in the frequency range of 680 to 1020 MHz.

ISBN 978-3-96147-205-5

9 783961 472055

FAU UNIVERSITY PRESS 2019